Optical spectroscopy of turbid media: time-domain measurements and accelerated Monte Carlo modelling

Alerstam, Erik

2011

Optical spectroscopy of turbid media: time-domain measurements and accelerated Monte Carlo modelling

Erik Alerstam

Doctoral Thesis
2011

Lund University

Optical spectroscopy of turbid media: time-domain measurements and accelerated Monte Carlo modelling

Printed in Sweden by Media-Tryck, Lund 2011

Division of Atomic Physics
Department of Physics
Faculty of Engineering, LTH
Lund University
P.O. Box 118
SE–221 00 Lund
Sweden

http://www.atomic.physics.lu.se
http://www.atomic.physics.lu.se/biophotonics

ISSN 0281-2762
Lund Reports on Atomic Physics, LRAP-447

ISBN 978-91-7473-203-0

Abstract

Optical spectroscopy is a versatile and powerful tool to probe translucent materials. In this work, the focus is on characterization of strongly scattering (turbid) materials by means of time-of-flight spectroscopy (TOFS). Instrumentation and modelling aspects of TOFS were investigated and improved, enabling significantly more accurate spectroscopic measurements.

It was shown that the commonly used diffusion theory fails to accurately describe time-domain light propagation in *e.g.* tissue. A fully scalable Monte Carlo (MC) scheme (WMC) was developed, enabling MC to replace diffusion models in TOFS data evaluation. Consequently, the accuracy and capabilities of TOFS were significantly improved. Graphics processing units (GPUs) were introduced for acceleration of MC simulations in general, resulting in three orders of magnitude speedup. It was shown that proper utilization of the capabilities of modern GPUs allow similar performance, even for more complex problems.

TOFS in combination with WMC was used in *in vivo* interstitial spectroscopy of the human prostate, demonstrating the need for better modelling in many clinical applications. To aid future interstitial *in vivo* measurements, a single-fibre TOFS system was developed and demonstrated in phantom experiments.

Turning to investigations of pharmaceutical samples, a time-of-flight spectrometer, covering the 650-1400 nm spectral range, was developed, enabling TOFS for vibrational spectroscopy of solids. In spatially resolved TOFS measurements, compaction induced anisotropic light diffusion was observed. This is of great importance for the application of model-based optical spectroscopic techniques and may, in addition, provide important information about the sample microstructure. Furthermore, TOFS was used together with laser-based gas sensing to probe porous solids. Although a need for better models was revealed, excellent correlation between optical and actual porosity was demonstrated.

Populärvetenskaplig sammanfattning

Denna avhandling handlar om optisk spektroskopi, d.v.s. att med hjälp av ljus bestämma fysiska och kemiska egenskaper hos ett prov.

När ljus interagerar med atomer och molekyler absorberas endast ljus av vissa våglängder (färger). Exakt vilka färger som absorberas är unikt för varje sorts atom eller molekyl och utgör alltså ett sorts ”fingeravtryck”. Genom att noggrant studera spektrat, d.v.s. hur absorptionen av ljus varierar med våglängden, kan man bestämma vilka ämnen som finns i ett prov. Om man dessutom vet hur långt ljuset passerade igenom provet kan man räkna ut exakt vilken koncentration av ämnent som finns i provet. Detta är en standardmetod för att mäta koncentrationer av ämnen i genomskinliga prover och används idag i oräkneliga tillämpningar världen över.

Går man över till grumliga prov, som till exempel mjölk blir situationen lite svårare. Mjölk, liksom papper, snö, moln, vit färg m.m. får sin vita färg av att ljuset hela tiden sprids, d.v.s. byter riktning, när det färdas i materialet. Mängden ljus och vilka färger som tar sig igenom ett grumligt prov beror alltså både på hur provet sprider och absorberar ljuset och man kan inte längre enkelt bestämma provets kemiska komposition.

I denna avhandling används en metod vid namn tidsupplöst spektroskopi för att optiskt undersöka grumliga material. Metoden bygger på att man skickar in extremt korta ljuspulser (miljondelars miljondels sekund långa) i materialet och studerar hur dessa pulser breddas i tiden när de breder ut sig i det spridande provet. Genom att jämföra hur pulsena breddas med matematiska modeller av ljusutbredning kan effekterna av spridning och absorption separeras. Den kemiska kompositionen kan nu bestämmas, samtidigt som spridningseffekterna ger information om den mikroskopiska strukturen hos materialet; i fallet mjölk kan t.ex. koncentrationen och storleken på mjölkens fettpartiklar bestämmas.

I mänsklig vävnad, som optiskt beter sig likt mjölk, är kemisk komposition och mikrostruktur av stort medicinskt intresse. Optiska metoder har visat sig lovande t.ex. när det kommer till att upptäcka och behandla cancer. Detta är extra intressant eftersom ljuset som används är ofarligt för kroppen, till skillnad mot t.ex. Röntgenstrålning. Ytterligare tillämpningar finns t.ex. i farmaceutisk industri där frågor som: "Hur mycket läkemedel finns det i en tablett?" och "Var i mag-tarmkanalen kommer läkemedlet att frigöras?" kan besvaras genom analys av kemisk sammansättning respektive materialstruktur. Båda dessa egenskaper kan potentiellt sett mätas med hjälp av ljus, utan att man ens behöver röra tabetten.

I avhandlingsarbetet har stort fokus lagts på att förbättra tidsupplöst spektroskopi. Detta har gjorts genom att utveckla nya mätinstrument och mätmetoder men framför allt genom att utveckla och snabba upp de matematiska modellerna som används för att utvärdera experimentell data. Detta har lett till att bättre modeller av ljusutbredningen kan användas, då det visade sig att konventionella modeller inte var tillräckligt exakta. Sammanfattningsvis ledde detta till mer noggranna resultat och ökade möjligheter för metoden.

Ytterligare har tidsupplöst spektroskopi använts för att karakterisera olika material, t.ex. mänsklig prostatavävnad och tabletter innehållande läkemedel.

List of publications

This thesis is based on the following papers, which will be referred to by their roman numerals in the text.

I **White Monte Carlo for time-resolved photon migration**
E. Alerstam, S. Andersson-Engels, and T. Svensson.
Journal of Biomedical Optics **13**, 041304 (2008).

II **Parallel computing with graphics processing units for high-speed Monte Carlo simulation of photon migration**
E. Alerstam, T. Svensson, and S. Andersson-Engels.
Journal of Biomedical Optics **13**, 060504 (2008).

III **Next-generation acceleration and code optimization for light transport in turbid media using GPUs**
E. Alerstam, W. C. Y. Lo, T. D. Han, J. Rose,
S. Andersson-Engels, and L. Lilge.
Biomedical Optics Express **1**, 658-675 (2010).

IV **Towards accurate in vivo spectroscopy of the human prostate**
T. Svensson, E. Alerstam, M. Einarsdóttír, K. Svanberg,
and S. Andersson-Engels.
Journal of Biophotonics **1**, 200-203 (2008).

V **Near-infrared photon time-of-flight spectroscopy of turbid materials up to 1400 nm**
T. Svensson, E. Alerstam, D. Khoptyar, J. Johansson,
S. Folestad and S. Andersson-Engels.
Review of Scientific Instruments **80**, 063105 (2009).

VI **Improved accuracy in time-resolved diffuse reflectance spectroscopy**
E. Alerstam, S. Andersson-Engels and T. Svensson.
Optics Express **16**, 10434-10448 (2008).

VII **Optical porosimetry and investigations of the porosity experienced by light interacting with porous media**
T. Svensson, E. Alerstam, J. Johansson, and S. Andersson-Engels.
Optics Letters **35**, 1740-1742 (2010).

VIII **Observation of anisotropic diffusion of light in compacted granular porous materials**
E. Alerstam, and T. Svensson.
(2011) *arXiv 1111.1700v1, to be submitted.*

IX **Toward single-fiber diffuse optical time-of-flight spectroscopy**
E. Alerstam, T. Svensson, S. Andersson-Engels, L. Spinelli, D. Contini, A. Dalla Mora, A. Tosi, F. Zappa and A. Pifferi.
(2011) *Manuscript in preparation.*

Other related publications by the author:

Evaluating the accuracy and precision of a two-compartment Kärger model using Monte Carlo simulations
M. Nilsson, E. Alerstam, R. Wirestam, F. Ståhlberg, S. Brockstedt, and J. Lätt.
Journal of Magnetic Resonance **206**, 59 - 67 (2010).

Abbreviations

CLT	central limit theorem
CPU	central procesing unit
DE	diffusion equation
DOS	diffuse optical spectroscopy
EBC	extrapolated boundary condition
FD	frequency domain
FDTD	finite difference time-domain
GASMAS	gas in scattering media absorption spectroscopy
GPU	graphics processing unit
IRF	instrumental response function
NIR	near infrared
NIRS	near infrared spectroscopy
PDF	probability density function
PDT	photo-dynamic therapy
PMT	photomultiplier tube
RTE	radiative transport equation
RTT	radiative transport theory
SPAD	single photon avalanche photodiode
TCSPC	time-correlated single photon counting
TOF	time-of-flight
TOFS	time-of-flight spectroscopy
WMC	white Monte Carlo

Contents

Papers

Chapter 1

Introduction

Optical spectroscopy is the subject concerned with the interaction between matter (atoms and molecules) and electromagnetic energy [1]. The interaction processes, *e.g.* absorption and scattering, are dependent on the energy, or wavelength, of the radiation and this dependence over a range of energies is called a *spectrum*. In the case of absorption, as a result of quantum mechanics, these spectra are unique for different kinds of atoms and molecules. Consequently, measuring the spectra allows detection, identification and quantification of the chemical composition of samples. Spectroscopic techniques play an important role in science and technology, and are widely used in physical and analytical chemistry [2], astronomy [3, 4], remote sensing [5], combustion physics [6] etc.

In addition to revealing the chemical composition of samples, spectroscopic techniques may be used to determine physical properties of objects by studying the spectrum of other interaction processes, such as scattering. This is used in, for example, determining the size distributions of particles in the atmospheres of distant planets [7], or assessment of pore size distributions in high density ceramics [8].

This thesis is devoted to optical spectroscopy of turbid materials, such as biological tissues and pharmaceutical preparations. In these materials, two interaction processes, absorption and scattering, are simultaneously present. The strong scattering process makes conventional absorption spectroscopy inapplicable as a simple transmission spectrum depends on the scattering and absorption processes in a complex manner. To overcome this problem, optical time-of-flight spectroscopy (TOFS) is employed.

In TOFS, the time-evolution of a short optical pulse propagating in a turbid material is measured. The temporal shape of the detected pulse is a signature of the average scattering and absorption properties of the probed sample. By carefully study-

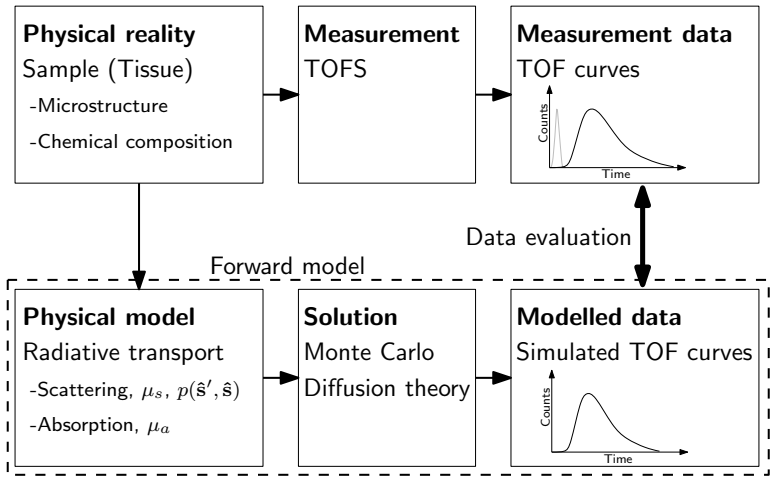

Figure 1.1. *Overview of the process of optical spectroscopy in turbid materials, using time-of-flight spectroscopy (TOFS). Modified from Nilsson [17].*

ing the temporal shape, the strengths of the two processes can be separated. Measurements over a range of wavelengths yields the absorption and scattering spectra, which in turn, may be related to the chemical composition and microstructure of the sample respectively. TOFS, and related techniques for diffuse optical spectroscopy (DOS) have found use, for example various aspects of medicine. The most well known example is the pulse oximeter [9], a basic and vital tool at every hospital, but more advanced applications are emerging, such as cancer detection [10, 11] and aid in, and monitoring, of tumour treatment [12–16].

Although not strictly spectroscopy, single wavelengths measurements using TOFS may also be used to gather valuable information, such as in material characterisation.

1.1 Overview of the scientific work

Fig. 1.1 provides an overview of the entire TOFS measurement and evaluation process, which also serves an overview of the work in this thesis.

In the context of a spectroscopic measurement, the sample, for example tissue, represents the **physical reality**. As mentioned in the previous section the spectroscopic measurements aims to accurately assess the properties, *e.g.* chemical composition and microstructure, of the sample. The sample is subject to a **measurement**, in this case using a TOFS system, resulting in **measured data**, *i.e.* a set of time-of-flight (TOF) curves. In this upper track

of Fig. 1.1 two things are important to note. First, it is of utmost importance to a have well working instrument, capable of probing and resolving the sample physical quantities of interest. Second, while the TOF curves contain information on the sample, the extraction of this information is not straightforward. One way of relating measurement data to sample properties is by calibration *i.e.* by comparing the measured data to previous measurements performed on samples with known properties. Another way is the so-called model-based approach, where the data is compared to a model of the measurement case. The first step in this approach is to construct a **physical model**, for example, using mathematics to describe how nature behaves.

In this thesis the major physical model is radiative transport. In radiative transport, the transport problem is described using a differential equation, where the sample properties are described by a set of coefficients. Several ways of solving this equation exist, such as diffusion theory and Monte Carlo simulations. In the calculation of the **solution**, the measurement geometry etc. is taken into account, resulting in a set of simulated TOF curves. If the model is accurate, and the coefficients used in the model are correct, this **modelled data** should correspond to the curves measured by the TOFS system. This problem of creating a physical model and solving it is called *forward modelling*, or the forward problem.

While not trivial, going from left to right in Fig. 1.1 is at least intuitive; a sample can be measured and the response of a sample can be mathematically modelled. However, as stated before, the problem of interest is rather to assess sample properties from a measurement, *i.e.* going from right to left. This is called the *inverse problem*. The inverse problem may be solved using the forward model. This is done by first making a guessing the properties of the sample and using this guess as the input in the forward model, resulting in a set of curves. The "guess" curves are compared to the measured curves and a new guess is made, based on how good the previous guess was. This process is iterated until the best agreement between the simulated and the measured data is found. It is evident that the forward model needs to accurately model the physics and that it needs to be fast in order to be applicable in this iterative fitting scheme.

1.2 Aim and outline of the thesis

Three general aims can be stated:

(i) To develop and improve the TOFS technique.

(ii) To improve the modelling of light propagation in turbid media, with emphasis on accurate and fast models for evaluation of TOFS data.

(iii) To explore the application of TOFS in biological and pharmaceutical samples.

Detailed descriptions of the scientific contributions, achieved in pursuit of these goals, are found in the peer-reviewed scientific articles that are enclosed at the end of the thesis. The purpose of the thesis chapters is to put these contributions into a broader context, and to provide a more thorough understanding of the models used.

The thesis chapters, and their connections to the papers are outlined below

Chapter 2 outlines the link between the physical reality and the physical model *i.e.* how light interacts with turbid media, such as biological tissue. In order to provide a forward model which may be solved with realistic effort, the physical reality is reduced to a theory of radiative transport, where the sample microstructure and chemical composition are reduced to two interaction coefficients, μ_s and μ_a, and a scattering phase function $p(\hat{\mathbf{s}}', \hat{\mathbf{s}})$.

Chapter 3 describes the Monte Carlo method, a technique for solving the radiative transport equation. Monte Carlo solutions are accurate but generally prohibitively slow. In order to use the technique in TOFS data evaluation, a powerful variance reduction technique was used in Paper **I**, resulting in a significant improvement of the accuracy of TOFS. Consequently, Monte Carlo was used in inverse modelling in Papers **VI**, and **IV**. In Papers **II**, and **III**, graphics processing units were introduced and explored in order to accelerate the forward Monte Carlo model for more general problems, resulting in a performance boost of several orders of magnitude. This enabled the simulations presented in Paper **IX**.

Chapter 4 discusses diffusion theory, a simplification of radiative transport featuring simple analytical solutions. Diffusion theory is widely used but suffers from limited validity under certain conditions. In Papers **I**, and **VI**, time-domain diffusion theory was compared to Monte Carlo, revealing large inaccuracies when using diffusion models to evaluate TOFS

data. In order to understand why diffusion theory fails, the approximations in diffusion theory are emphasized using an alternative derivation of the theory.

Chapter 5 covers various aspects of TOFS, such as instrumentation, advantages and disadvantages of the technique, possible applications of TOFS, etc. Papers **V**, and **IX** relates to the instrument aspect of TOFS. In Paper **IV** TOFS was used to perform *in vivo* spectroscopy of the human prostate, and in Papers **VII** and **VIII** TOFS was explored as a tool to assess structural properties of porous materials.

Chapter 2

Light-matter interactions and radiative transport theory

This chapter introduces radiative transport theory (RTT) and the radiative transport equation (RTE), the fundamental equation of interest in many applications of diffuse optical spectroscopy. In order to understand the underlying physics of RTT, the chapter begins with a brief reminder of how light interacts with matter and how the *scattering coefficient*, μ_s, the *absorption coefficient*, μ_a, and the *scattering phase function*, $p(\hat{\mathbf{s}}', \hat{\mathbf{s}})$, relates to the more fundamental wave theory of light.

In the end of the chapter different ways of solving the RTE and properties of the solutions are briefly discussed, setting the stage for Chapter 3 and 4.

2.1 Light-matter interaction

This section gives a very brief introduction to electrodynamics, highlighting a few important concepts that are needed for the discussion in the preceding sections.

2.1.1 Electromagnetic wave theory

The fundamental equations describing the behaviour of electromagnetic fields are the microscopic Maxwell equations [18] (in SI

units):

$$\nabla \times \mathbf{E} = -\frac{\partial \mathbf{B}}{\partial t}, \tag{2.1}$$

$$\nabla \times \mathbf{B} = \mu_0 \mathbf{J} + \mu_0 \varepsilon_0 \frac{\partial \mathbf{E}}{\partial t}, \tag{2.2}$$

$$\nabla \cdot \mathbf{E} = \frac{1}{\varepsilon_0} \rho, \tag{2.3}$$

$$\nabla \cdot \mathbf{B} = 0, \tag{2.4}$$

where $\mathbf{E}$ and $\mathbf{B}$ are the electric and magnetic fields, respectively, which may vary in space, $\mathbf{r}$, and with time, t. The vacuum permittivity, ε_0, and the vacuum permeability, μ_0 are fundamental constants. The charge- and current density are denoted ρ and $\mathbf{J}$, respectively. In the materials of interest in this thesis, *e.g.* biological tissue, the contribution of free currents and charges are negligible [19]. Therefore, ρ and $\mathbf{J}$ describe the microscopic ("bound") charges and currents *i.e.* electron clouds bound to atoms or molecules. Further, the materials may be considered non-magnetic ($\mu_r = 1$, *i.e.* the permeability of the materials is the same as that of vacuum, μ_0). In conclusion, the charge density and current density originate from the electric *dipoles* induced in the material by the $\mathbf{E}$-field,

$$\rho = -\nabla \cdot \mathbf{P}, \tag{2.5}$$

$$\mathbf{J} = \frac{\partial \mathbf{P}}{\partial t}, \tag{2.6}$$

where $\mathbf{P}$ is the polarization, describing the dipole moment density. Assuming the medium is linear and isotropic the polarization may be written

$$\mathbf{P} = \varepsilon_0 \chi \mathbf{E}, \tag{2.7}$$

where χ is the linear susceptibility which may vary in space and time. It is convenient to combine Eq. 2.3, 2.5, and 2.7 into

$$\mathbf{D} = \varepsilon_0 \mathbf{E} + \mathbf{P} = \varepsilon \mathbf{E}, \tag{2.8}$$

where $\mathbf{D}$ is called the electric displacement, and ε is the (complex) permittivity of the material

$$\varepsilon(\mathbf{r}, t) = \varepsilon_0 \varepsilon_r = \varepsilon_0 (1 + \chi(\mathbf{r}, t)). \tag{2.9}$$

In absence of free charges

$$\nabla \cdot \mathbf{D} = 0, \tag{2.10}$$

replaces Eq. 2.3 in the Maxwell equations.

In principle, the Maxwell equations and the complex permittivity $\varepsilon(\mathbf{r}, t)$ is everything needed to completely characterize the

behaviour of any system under the assumptions made above. However, in turbid materials such as tissue, ε varies spatially on all microscopically relevant length-scales, from nanometres to micrometres, and may vary in time as well. Hence, both defining turbid materials on a macroscopic scale, millimetres to centimetres, as well as solving the equations for such materials becomes an impossible task. In order to describe the transport of light on a macroscopic scale, simplifications are necessary.

Taking the curl of Eq. 2.1 leads to a wave equation for the electric field (the same may be shown for the magnetic field), showing that in a homogeneous medium electromagnetic energy propagates as a wave with electric and magnetic field vectors perpendicular to each other as well as the propagation direction of the wave. In vacuum, the wave travels with the speed $c = 1/\sqrt{\varepsilon_0\mu_0}$ *i.e.* the speed of light. In a medium (as described above) the speed of the wave, called the phase velocity, is $v_p = c/\Re(n)$, where n is the *refractive index*, $n = \sqrt{\varepsilon_r\mu_r}$. The refractive index is commonly used in optics to describe the properties of a materials and can, in the context of this thesis, be treated as an equivalent to the relative permittivity (as $\mu_r = 1$).

The Poynting vector, $\mathbf{S}$ is a quantity describing the energy per unit time, per unit area transported by the fields:

$$\mathbf{S}(t) = \frac{1}{\mu_0}(\mathbf{E} \times \mathbf{B}). \tag{2.11}$$

However, the Poynting vector may fluctuate rapidly. Instead the time averaged (over several oscillations) Poynting vector is considered

$$\langle \mathbf{S} \rangle = \frac{1}{2}\frac{1}{\mu_0\mu_r}\Re(\mathbf{E} \times \mathbf{B}^*). \tag{2.12}$$

2.2 Scattering

Scattering is the physical process that occurs when a propagating wave encounters an inhomogeneity in the medium in which it propagates. Consider, for example, a lone atom suspended in free space. The atom is composed of a positively charged nucleus (*e.g.* a proton) surrounded by a negatively charged electron cloud. If subjected to an oscillating electric field, such as an electromagnetic wave, the field will accelerate the charges forcing them into an oscillatory motion. Accelerating charges radiate electromagnetic energy in all directions; the electromagnetic wave is "scattered". This process is true also for aggregates of atoms, molecules, and even macroscopic collections of molecules *i.e.* macroscopic objects. In terms of macroscopic wave propagation scattering may be seen as a distortion of the wave front of a propagating wave by an inhomogeneity in the medium, forcing energy of the wave to

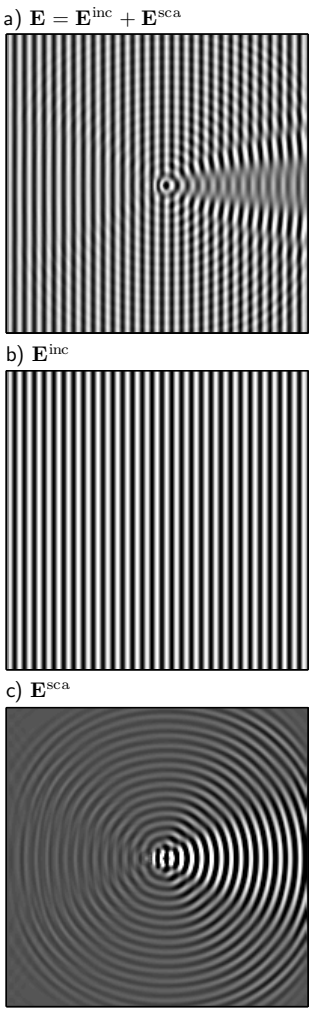

Figure 2.1. *An FDTD simulation of electromagnetic wave propagation in 2 dimensions. The real part of the electric field is shown (the intensity scale is optimized for each subfigure) for the incoming field* $\mathbf{E}^{\mathrm{inc}}$*, a plane monochromatic wave propagating from left to right and the field in presence of a small circular scatterer* $\mathbf{E}$*. The scattered field,* $\mathbf{E}^{\mathrm{sca}} = \mathbf{E} - \mathbf{E}^{\mathrm{inc}}$ *is also shown, showing a spherical wave propagating outwards from the scatterer with intensity varying with the direction. Modified from [20].*

propagate in new directions. The inhomogeneity, if localized, is called a *scatterer*. Below, scattering by a single scatterer is first discussed, followed by a discussion of light propagation in i medium with many scatterers present, so called *multiple scattering*.

Scattering by single particles is the subject of several books (see *e.g.* [21–23]). Similarly, multiple scattering is covered by *e.g.* [20, 23–26].

In this thesis only *elastic scattering* is considered, *i.e.* where the energy, and thus the wavelength, is conserved in the scattering process. Several inelastic scattering phenomena also exist, such as Raman- and Brillouin scattering, but these processes are typically much weaker than elastic scattering [1] and may be ignored in this context.

2.2.1 Scattering by a single particle

Here, a single scatterer in an unbounded homogeneous medium is considered. A plane harmonic wave is incident on the particle, and is consequently distorted by the presence of the scatterer, creating a new field. This resulting field, $\mathbf{E}$, may be expressed as the sum of the incoming field, $\mathbf{E}^{\mathrm{inc}}$ and the scattered field $\mathbf{E}^{\mathrm{sca}}$. This separation of the field is purely mathematical, $\mathbf{E}$ is the actual physical field. However, it is evident that energy is transferred from $\mathbf{E}^{\mathrm{inc}}$ to $\mathbf{E}^{\mathrm{sca}}$ and that energy may radiate from the scattering particle in all directions. This is illustrated in Fig. 2.1 showing the results of a 2D finite difference time-domain (FDTD) simulation of the scattering a plane harmonic wave by a small particle.

Due to the limited complexity of the above problem, the Maxwell equations can be used to solve the problem directly either analytically or numerically. Early and important contributions include the work by Rayleigh on scatterers much smaller than the wavelength of light, *e.g.* molecules [27, 28] (called Rayleigh scattering) and on spherical scatterers by Mie [29] (Mie scattering). The scattered field $\mathbf{E}^{\mathrm{sca}}$, originating from a plane wave scattered by a single scatterer, may be characterized by a single parameter: the *differential scattering cross section*, $\partial\sigma_{\mathrm{sca}}$. This parameter describes the angular distribution of the power of the scattered field (the Poynting vector of the far field scattered field). It should be noted that the differential scattering cross section, and all parameters derived from it, is wavelength dependent $\partial\sigma_{\mathrm{sca}} = \partial\sigma_{\mathrm{sca}}(\lambda)$. The explicit notation of this dependence have been left out for brevity. Integrating the differential scattering cross section over all solid angles yields the *scattering cross section*,

$$\sigma_{sca} = \int_{4\pi} \partial\sigma_{\mathrm{sca}} d\omega', \tag{2.13}$$

which, avoiding geometrical interpretations, describe the strength (or probability) of interaction between the incident and scattered fields. Normalizing the differential scattering cross section with the scattering cross section yields the *(single) scattering phase function*

$$p(\hat{\mathbf{s}}', \hat{\mathbf{s}}) = \frac{\partial \sigma_{\text{sca}}}{\sigma_{\text{sca}}}. \tag{2.14}$$

The scattering phase function is, in essence, a characterization of the far field of the scattered field. It describes the Poynting vector of the scattered field, in direction $\hat{\mathbf{s}}$, far away from the scatterer. Here, the scattered field originates from a plane wave, propagating in direction $\hat{\mathbf{s}}'$, incident on the scatterer. Also, the scattering phase function is normalized by the interaction strength, so that the integration over all solid angles is equal to one

$$\int_{4\pi} p(\hat{\mathbf{s}}', \hat{\mathbf{s}}) d\omega' = 1. \tag{2.15}$$

In conclusion, the elastic interaction between a plane harmonic wave and a scatterer may be described by the two parameters σ_{sca} and $p(\hat{\mathbf{s}}', \hat{\mathbf{s}})$.

2.2.2 Single scattering

The results for a single scatterer may be used to solve more difficult problems. Considering a dilute suspension of scatterers with the density of scatterers (number density), ρ_{sca}, the interaction between an incident wave and the suspension may be described by a *scattering coefficient*

$$\mu_s = \sigma_{\text{sca}} \rho_{\text{sca}}. \tag{2.16}$$

The scattering coefficient describes the probability of interaction with the scatterers per unit length travelled. In order to understand the meaning of this, another example is used: A plane wave is propagating in a direction $\hat{\mathbf{s}}'$ in the suspension of scatterers. Travelling an infinitesimal length, Δx in this medium, the total interaction between the plane wave and the scatterers is, on average, $\mu_s \Delta x$. The intensity "lost" in this step is

$$dI = -\mu_s \Delta x I, \tag{2.17}$$

where I is the intensity (as described by the Poynting vector) of the wave. The energy is not really lost, rather it is scattered to all other directions. Assuming that the amount of energy scattered back into the direction $\hat{\mathbf{s}}'$ is negligible, it follows directly from Eq. 2.17 that the intensity, I, of the plane wave will decay exponentially

$$I = I_0 \exp(-\mu_s L), \tag{2.18}$$

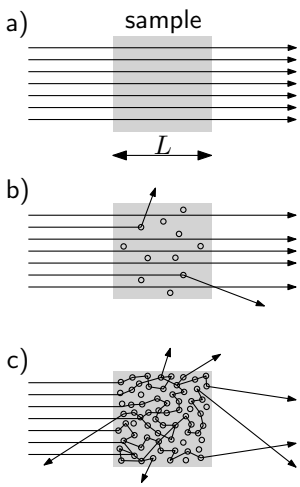

Figure 2.2. *Illustration of light propagating in three different samples (here light is illustrated by rays, as in geometrical optics). In a) there is no scattering, light passes straight through. In b) the sample is a dilute suspension of scatterers, rays are scattered only once, the single scattering regime. In c) rays are scattered multiple times. Only scattered rays are transmitted. Modified from [31].*

where I_0 is the incident intensity and L is the total distance travelled. This is illustrated in Fig. 2.2; in a) there are no scatterers and the transmitted intensity equal the incident intensity. In b) a few scatterers are present and the transmitted intensity is described by Eq. 2.18. The contribution of the intensity of the scattered waves is negligible. However, in c) the density of scatterers is large and the contribution of the scattered field can no longer be ignored. All the energy of the incident plane wave have been scattered to new directions, where the energy in turn have been scattered again by other scatterers. While the plane wave no longer contributes to the transmission, waves that have been scattered multiple times do. The analysis of this is the topic of the next section.

While the approximation to ignore the scattered fields may seem crude, several problems exist where this, so called, *single scattering*, description often is applicable, such as propagation of light in the earth's atmosphere [5] and in interstellar atmospheres [30]. An enlightening example is provided by Rayleigh, who, in 1871, managed to explain the blue appearance of the sky by finding out that the light originates from single scattering of light by small particles present in the atmosphere. Such particles, for example molecules, are much smaller than the wavelength of visible light and have a scattering cross section dependent on the wavelength according to $\sigma_{\text{sca}} \propto \lambda^{-4}$. The interaction is thus stronger for blue light which dominates the spectrum when observing scattered light, *i.e.* when not looking directly at the sun [27, 28].

2.2.3 Multiple scattering

Continuing the example of light propagating in the atmosphere, clouds represent the next complication. Clouds may also be considered a dilute suspension of scatterers, where the scatterers are small water droplets. However, the appearance of clouds is very different from that of the blue sky. The white colour of clouds is characteristic of materials exhibiting *multiple scattering* of light. Many everyday objects such as milk, snow, white paint, pharmaceutical tablets and paper owes their white appearance to multiple light scattering.

The difference between clouds and the atmosphere lies both in the characteristics of the scatterers, water droplets are bigger than molecules, and the density of scatterers. The result of this difference is that the scattering coefficient of clouds is significantly larger than that of the weakly scattering atmosphere. Considering the transmission of light through the atmosphere, compared to transmission through a cloud, the two cases can be illustrated by b) and c) in Fig. 2.2.

The treatment of multiple scattering in the framework of electromagnetic wave propagation is not trivial. Early work on the

rigorous treatment of multiple scattering was done by Foldy, who expressed the total field of scalar waves in the presence of N scatterers as the sum of the incident field and the contributions from each scatter [32]

$$\mathbf{E}(\mathbf{r}) = \mathbf{E}^{\text{inc}}(\mathbf{r}) + \sum_{i=1}^{N} \mathbf{E}_i^{\text{sca}}(\mathbf{r}). \tag{2.19}$$

Foldys treatment uses determined positions of all scatterers and follow directly from Maxwell equations in the first order Born approximation. In this approximation, the field driving the oscillations in all dipoles is assumed to be independent of the presence of all the scatterers. In the next step in Foldys treatment, the scattered fields from each of the scatterers are used as the driving field of all other scatterers. The field from each scatterer depends on the field of all other scatterers, resulting in a recursive behaviour. The solution of iterating the scattered fields *ad infinitum* is inefficient and another approach is needed to solve the multiple scattering problem.

One way to proceed with multiple scattering is to give up the determined positions of the scatterers, moving to a statistic description of the scattering medium. This was done already in the previous section when introducing the scattering coefficient, by using the density of scatterers. The scattering coefficient may be defined in the same way when considering multiple scattering. It is also meaningful to consider an equivalent parameter, the *mean free path*

$$\ell = \frac{1}{\mu_s}. \tag{2.20}$$

The mean free path may be interpreted in an intuitive way. Considering the scattered field, propagating as a wave outwards from its scattered, and a direction $\hat{\mathbf{s}}$. The mean free path is the average distance the scattered field propagates in that direction before it encounters a new scatterer. If the mean free path is much longer than the wavelength of light, the scattered wave is approximately equivalent to a plane wave when it encounters the next scatterer, and the theory of scattering by a single particle may be used again. However, if the mean free path is short, so that the scatterers interact in the near field, the theory used to define the differential cross section, and subsequently derived parameters, breaks down.

In summary, assuming the scatterers are not to densely packed, the theory from scattering by a single particle may be utilized and the average behaviour of a scattering material may be characterized using just two parameters, μ_s and $p(\hat{\mathbf{s}}', \hat{\mathbf{s}})$. In order to proceed with the multiple scattering problem, radiative transport theory will be introduced in Section 2.4, but before that a small detour

will be made in order to investigate scattering of light by tissue and to introduce the concept of absorption.

2.2.4 Scattering of light by tissue

Looking closely at biological tissue, it is clear that it is not a simple medium. Biological tissue consist of a flora of molecules, particles and structures with different properties and sizes, all compacted together to form a medium with spatial (and temporal) variations in the refractive index on length scales from nanometres and up, or, in the words of Schmitt and Kumar, "*the structure of the refractive-index inhomogeneities in a variety of mammalian tissues resembles that of frozen turbulence*" [33]. Clearly, tissue is not a dilute suspension of scatterers and at first glance it seems like the above description of multiple scattering falls apart. However, treating the problem of light scattering by tissue from the point of view of electrodynamics, it may be shown that multiple scattering theory is still applicable [31, 34, 35], and that tissue, just like the suspension of discrete scatterers, may be characterized by a few parameters. The full explanation of this treatment is extensive but a few relevant results are summarized here.

The effective refractive index

A water molecule or a water droplet in air acts as a scatterer of light, however, assembling many water molecules (or droplets) and light may propagate, virtually without being scattered, in the resulting body of water. The reason is that the strength of the scattering process, σ_{sca}, depend on the difference in refractive index between the scatterer and the background. When the scattering molecules have the same refractive index as the surrounding medium, the molecules no longer act as scatterers.

In tissue, all the scatterers and structures are compressed into a continuum, $n(\mathbf{r}, t)$. From the point of view of scattering, it is instructive to express this continuum as

$$n(\mathbf{r}, t) = n_{\text{eff}} + n_e(\mathbf{r}, t), \tag{2.21}$$

where n_{eff} is the mean of the refractive index continuum, $n_{\text{eff}} = \langle n(\mathbf{r}, t) \rangle$, called the *effective refractive index* and $n_e(\mathbf{r}, t)$ is the variations in refractive index with respect to n_{eff}.

For relevant wavelengths of light (600-1000 nm) the effective refractive index of tissue is ~ 1.4 [36]. Schmitt and Kumar came to a similar conclusion ($n_{\text{eff}} \approx 1.35$) adding that the microscopic variations in refractive index, $n_e(\mathbf{r}, t)$, of soft tissue vary between 0.04 and 0.1 [37].

The scattering coefficient

The task of defining and calculating a scattering coefficient from the spatial fluctuations in refractive index describing tissue is a daunting task. Historically, tissue have been considered equivalent to a collection of discrete Mie (spherical) scatterers interacting only in the far field [38, 39]. In a more modern treatment, the scattering coefficient, and the scattering phase function, are calculated from the correlation function of the spatial fluctuations (see *e.g.* [31, 35, 37]) taking the near field interaction of the structures contributing to the scattering into account. The resulting description of scattering, surprisingly, shares many similarities with the Mie-scatterer description, for example, the wavelength dependence of the scattering coefficient which in both cases is described a power law

$$\mu_s = a\lambda^{-b}. \tag{2.22}$$

The coefficients a and b are related to the structure of the tissue. In Mie theory, a and b are directly related to density of scatterers and scatterer size respectively. The other theory, representing a far more complex material, does not allow such a direct interpretation.

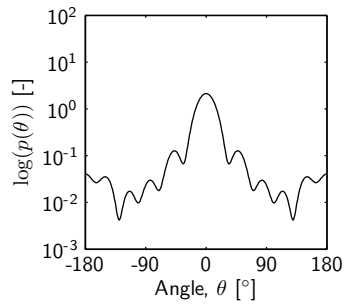

Figure 2.3. *An illustration of the scattering phase function of a dielectric sphere (Mie scatterer). Typical for larger scatterers, forward scattering is dominant. Multiple side lobes, due to interference, are visible. Compare to Fig. 2.1 c) where such lobes are vaguely visible. The average cosine of the angle scattering angle is* $\langle \cos\theta \rangle = 0.68$. *Data from the Mie calculator [40].*

The scattering phase function

For scattering by physical particles, the scattering phase function may be calculated with relative ease. For randomly oriented small particles, *i.e.* Rayleigh scatterers, the scattering is isotropic. In case of Mie scattering, the exact shape of the scattering phase function depends on the size and permittivity of the spherical particle but, in general, the scattering is dominant in the forward direction with minor side-lobes, see Fig. 2.3. In general, it is assumed that the scattering phase function is independent of the propagation direction, *i.e.* $p(\hat{\mathbf{s}}', \hat{\mathbf{s}}) = p(\hat{\mathbf{s}}' \cdot \hat{\mathbf{s}})$, which is true, on average, when the scatterers are randomly oriented. Further, it is commonly assumed that the scattering probability is symmetric for the azimuthal angle, ϕ. That is, the scattering phase function only depends on the deflection (inclination) angle, θ

$$p(\hat{\mathbf{s}}', \hat{\mathbf{s}}) = p(\cos(\theta)). \tag{2.23}$$

Working with diffuse interstellar radiation, Henyey and Greenstein invented a scattering phase function to approximate Mie-scattering, the so-called Henyey-Greenstein function [41]. It may be regarded as an approximative average of a polydisperse ensemble of Mie-scatterers where the lobes, caused by interference effects, are cancelled out. The Henyey-Greenstein scattering phase function is

$$p(\cos\theta) = \frac{1}{4\pi} \frac{1 - g^2}{(1 + g^2 - 2g\cos\theta)^{3/2}}, \tag{2.24}$$

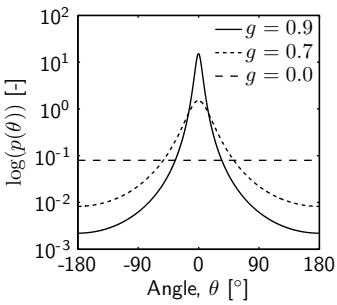

Figure 2.4. *The Henyey-Greenstein scattering phase function for $g = 0.9$, $g = 0.7$, and $g = 0.0$ (isotropic). The $g = 0.7$ curve may be compared to Fig. 2.3 as they (approximately) share the same $g = \langle \cos\theta \rangle$.*

where g, called the *anisotropy factor* or the *g-factor*, is the average of the cosine of the deflection angle,

$$g = \langle \cos\theta \rangle = \int_{4\pi} p(\hat{\mathbf{s}}', \hat{\mathbf{s}}) \cos\theta d\omega' = \int_{4\pi} p(\hat{\mathbf{s}}', \hat{\mathbf{s}})(\hat{\mathbf{s}}' \cdot \hat{\mathbf{s}}) d\omega'. \quad (2.25)$$

The Henyey-Greenstein phase function for different values of g is illustrated in Fig. 2.4.

Despite light scattering in tissue being different from that of Mie-scatterers, the Henyey-Greenstein function approximates the scattering phase function of tissue well [31] as forward scattering is dominant in both cases. The Henyey-Greenstein was introduced into tissue optics by Jacques *et al.* [42], and have been successfully used in countless studies since. The reason for the success will be explored in Chapter 4 where it is shown that the exact shape of the scattering phase function does not significantly influence macroscopic light transport.

2.3 Absorption

Going back to the description of matter as a collection of molecules (or atoms) as in the beginning of Section 2.2, another prominent phenomena must also be considered. In addition to re-radiating energy as a scattered wave, energy may also be *absorbed* by the molecule. This happens when the energy of a *photon* (the discretized energy of the electromagnetic field) exactly matches the transition energy of the molecule, causing it to be excited to a higher electronic, vibrational, or rotational state. For free molecules, as for example in a gas, the transition energies are well defined and only photons with certain energies may be absorbed. In soft matter, such as tissue or granular materials, the random interactions of the molecules cause a transformation the narrow energy levels to broad spectral features. The spectral width of absorption peaks in such materials are typically several nanometres broad. This difference in the spectral dependence of the absorption in solids and gases is used in the GASMAS-technique [43], where the weak absorption of free gases trapped in porous or hollow solids can be studied. This was used in the investigation in Paper **VII**.

The fate of the absorbed energy is interesting to consider. A common result of absorption is heating of the absorbing materials. The absorbed energy may also be re-emitted as light, so called *fluorescence*. The re-emission is typically delayed (nano- to milliseconds) and significantly Stokes shifted, making it irrelevant in the scope of this thesis. It should, however, be mentioned that fluorescence is a commonly used diagnostic tool in the field of biomedical optics [44]. The absorbed energy may also be used to drive a chemical process. For example, in *photodynamic therapy*

(PDT) the energy is transferred, via a molecule called a photosensitizer, to an oxygen molecule, creating toxic singlet oxygen molecules, used to kill cells (*e.g.* tumors) [45].

2.3.1 The absorption coefficient

Since the absorbed energy is considered lost, the knowledge of the exact positions of the absorbers may be considered redundant information. Moving from a deterministic to a stochastic description of absorption, the absorption coefficient, μ_a, may be defined as

$$\mu_a(\lambda) = \sigma_{\text{abs}}(\lambda)\rho_{\text{abs}}, \tag{2.26}$$

where ρ_{abs} is the density of absorbers, and $\sigma_{\text{abs}}(\lambda)$ is the cross section for the absorption process at wavelength λ. The absorption coefficient describe the probability of absorption per unit length travelled. Just as for the scattering coefficient, this Poisson process leads to an exponential decrease in the intensity of a propagating wave, as described by the famous Beer-Lamberts law

$$I = I_0 \exp(-\mu_a L) = I_0 \exp(-\mu_a v t), \tag{2.27}$$

where $L = vt$ is the propagation distance, t is the propagation time, and v is the local speed of light.

The wavelength dependence of the absorption coefficient in Eq. 2.26 is emphasised as $\mu_a(\lambda)$ serves as a "fingerprint" for each species of molecules. This is important as $\mu_a(\lambda)$ can reveal the exact constituents and concentrations thereof in a sample. This is the foundation of *absorption spectroscopy*.

In the presence of several absorbing molecule species, so-called *chromophores*, the total absorption coefficient is the sum of the contribution from each chromophore

$$\mu_a(\lambda) = \sum_i \sigma_{i,\text{abs}}(\lambda)\rho_{i,\text{abs}}. \tag{2.28}$$

Knowing the absorption cross section of all chromophores, $\sigma_{i,\text{abs}}(\lambda)$, the concentration of each chromophore may be derived from a measured absorption spectrum.

2.3.2 Absorption in tissue

Biological tissue contain a large number of different molecules and biomolecules. In the visible- and ultraviolet spectral range tissue is highly scattering and absorbing, limiting the applicability of diffuse optical spectroscopic technique. However, in the near infrared (NIR) spectral range, an absorption "window" exist where the penetration depth of light is in the order of milli- to centimetres. This spectral window, called tissue optical window [50], is limited by the absorption of blood (hemoglobin) for shorter wavelengths

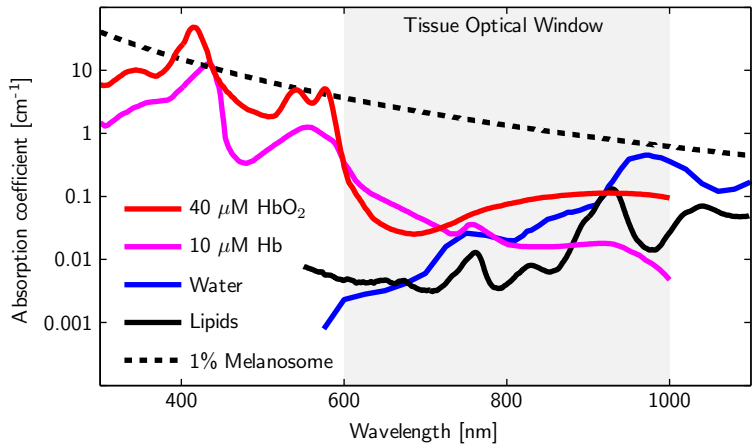

Figure 2.5. *The tissue optical window and the absorption spectra of a few common tissue chromophores: Oxygenated and deoxygenated hemoglobin [46], water [47], lipids [48], and melanin [49].*

($\lambda < 600$ nm) and water for longer wavelengths ($\lambda > 1000$ nm). Prominent chromophores in tissue within this window include: water [47], hemoglobin [46], myoglobin [51], lipids [48], cytochromes [52], melanin [49], and collagen [53, 54]. Fig. 2.5 illustrates the absorption spectra of a few chromophores in tissue along with the tissue optical window.

2.4 Radiative transport

With the absorption coefficient, scattering coefficient and the scattering phase function introduced, the stage is set for radiative transport theory (RTT) as a way to model multiple scattering. RTT is a phenomenological theory, based on arguments of energy conservation. The effects of absorption and scattering, as described in the previous sections, are incorporated in a differential equation describing energy conservation in a small control volume. This equation, called the radiative transport equation (RTE) or the Boltzmann equation, is introduced in the next section.

The work on RTT was initiated by Schuster who considered transport of radiation through a foggy atmosphere [55, 56] and have since been used in many and diverse fields of physics, for example, propagation of light in planetary and interstellar atmospheres [23, 30] and neutron transport [57]. RTT was used in early investigations of light transport in whole blood [58, 59], introducing the theory to the field of tissue optics, where it generally is

considered the gold standard model [60].

2.4.1 The radiative transport equation

Using the macroscopic optical properties discussed in the previous sections (the scattering coefficient μ_s and the absorption coefficient μ_a along with a scattering phase function, $p(\hat{\mathbf{s}}', \hat{\mathbf{s}})$) the RTE may be formulated. The RTE is an equation of energy conservation which is reached heuristically by considering the change in the flow of power along direction $\hat{\mathbf{s}}$ inside a small volume, V:

$$\frac{1}{v}\frac{\partial L}{\partial t} = \underbrace{q}_{\text{i)}} + \underbrace{\mu_s \int_{4\pi} p(\hat{\mathbf{s}}', \hat{\mathbf{s}}) L d\omega'}_{\text{ii)}} - \underbrace{\hat{\mathbf{s}} \cdot \nabla L}_{\text{iii)}} - \underbrace{L(\mu_s + \mu_a)}_{\text{iv)}}, \quad (2.29)$$

where $L = L(\mathbf{r}, \hat{\mathbf{s}}, t)$ [W/m^{2}sr] is the *radiance*, describing the power per unit area and per steradian flowing in direction $\hat{\mathbf{s}}$ and v is the energy transport velocity. The terms on the right-hand side of the equation, illustrated in Fig. 2.6, are:

i) Radiance gain due to sources inside the volume, $q = q(\mathbf{r}, \hat{\mathbf{s}}, t)$ [W/m^{3}sr].

ii) Radiance gain due to scattering from direction $\hat{\mathbf{s}}'$ into direction $\hat{\mathbf{s}}$. μ_s [m^{-1}] is the scattering coefficient and $p(\hat{\mathbf{s}}', \hat{\mathbf{s}})$ [-] is the scattering phase function.

iii) Change in radiance due to energy crossing the volume boundary.

iv) Radiance loss due to scattering (μ_s) and absorption (μ_a) respectively.

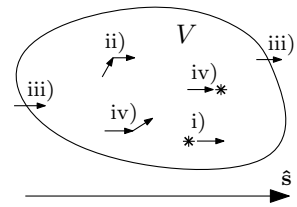

Figure 2.6. *Radiative transport theory considers conservation of energy in a volume, V, travelling in direction $\hat{\mathbf{s}}$. Energy is lost due to scattering and absorption, iv), and gained from scattering, ii), as well as sources inside V, i). Energy both enter and exit through the boundary, iii).*

2.4.2 Relationship between multiple scattering- and transport theory

The "derivation" of the RTE above is heuristic and is based on energy conservation. Its relation to wave propagation is contained in the derivation of the scattering coefficient and scattering phase function, but all wave properties of the multiple scattering problem are lost. This lack of rigorous derivation from the Maxwell equations was noted early [23, 61, 62] and the link between multiple scattering (*i.e.* Maxwell) theory and radiative transport have been an active area of research since.

In RTT, the radiance is treated as a ray of light completely lacking wave properties just as in geometrical optics. Ishimaru [23], Wolf [61] and Fante [62] investigated the meaning of the radiance and concluded that it may, under certain assumptions, be regarded

as the time averaged Poynting vector in wave theory. However, this is not a rigorous link between RTT and multiple scattering or wave theory.

The existence of a formal link between RTT and wave theory was shown, for example, in the recent work by Mishchenko, where the vector-RTE is rigorously derived from the Maxwell equations [63]. For details on the derivation, a summary of the work creating the formal link as well as discussions on common misconceptions related to RTT, the reader is directed to the work by Mishchenko and references therein [20, 25, 26, 63–65].

The loss of wave properties in the RTE has not been considered a problem in biomedical applications. However, in recent years, ways to exploit the wave properties of light in turbid materials have been investigated. For example, coherent/enhanced backscattering [66, 67] can be observed also in tissues, allowing the effect to be used *e.g.* for optical spectroscopy [68]. Phase conjugation techniques may be used to enhance transmission through tissue [69] and time-reversal in combination with ultrasound may be used to focus light deep inside scattering materials [70]. Further, scattering materials have recently been used to create high numerical aperture lenses [71]. All the above examples use the fact that light transport in scattering materials, even tissue, is deterministic as opposed to the stochastic nature suggested by RTE. Also, these applications serve as a reminder that light is transported as waves, not as "rays" or particles as commonly stated.

2.4.3 Solving the radiative transport equation

Despite the drastic simplifications involved in transforming multiple scattering theory to reach RTT, the resulting equation is not easy to solve. This section gives a brief introduction to some common solution techniques used to solve the RTE.

Monte Carlo

The Monte Carlo (MC) method involve stochastic numerical simulations of the RTE by tracing fictional particles through the medium. In the limit of infinitely many particles traced, MC is an exact solution to the RTE and is often used as the gold standard when in the evaluation of other solution techniques. MC will be covered in Chapter 3.

Spherical harmonics - P_N

In this solution method the radiance in expanded in a series of spherical harmonic functions. The series is truncated after N terms, (the so called P_N-approximation) leaving a system of equa-

tions which may be solved numerically but at great computational cost [72, 73]. In certain cases analytical solutions may be found as shown by Liemert and Kienle [74, 75]. In the limit $N \to \infty$ the method provides an exact solution to the RTE.

Diffusion theory

Diffusion theory is a special case of the P_N method. With $N = 1$ and some further simplifications, the RTE turns into a diffusion equation where simple analytical solutions may be found. The analytical solutions, in combination with the fact that diffusion in many cases is a sufficiently good approximation of RTT, have made diffusion solutions the most widely employed theory to solve the radiative transport problem. Diffusion theory is covered in Chapter 4.

Simplified spherical harmonics - SP_N

In the simplified spherical harmonics method (SP_N), the 1D-P_N equations are transformed to 3D, leaving a set of coupled equations, much simpler than the 3D P_N equivalents [76]. These equations may be solved numerically, [76–80] or, for simple geometries, analytically [81]. Contrary to the P_N method, in the limit $N \to \infty$ the SP_N method does not converge towards an exact solution of the RTE [76].

Discrete ordinates - S_N

In the discrete ordinates method, S_N, the radiance is discretized in N angular directions. This transforms the integral in Eq. 2.29 into a sum, converting the RTE into a matrix differential equation which may be solved numerically [57, 82, 83].

2.4.4 Properties of the solutions to the RTE

While solutions to the RTE may not easily be found, properties of such solutions may be deduced. An important property of the RTE and its solutions concerns how absorption is handled. The Beer-Lambert law states that the intensity of a wave propagating in an absorbing medium decays exponentially with time (Eq. 2.27) and the same should thus be true for the solutions of the RTE. If $L_0(\mathbf{r}, \hat{\mathbf{s}}, t)$ is the solution to the RTE for a nonabsorbing medium ($\mu_a = 0$) with a source described by a Dirac delta function ($q = \delta_r \delta_t$), then the expected solution, keeping all properties fixed but adding absorption (independent of $\mathbf{r}$), should be

$$L(\mathbf{r}, \hat{\mathbf{s}}, t) = L_0(\mathbf{r}, \hat{\mathbf{s}}, t) \exp(-\mu_a v t). \tag{2.30}$$

Inserting Eq. 2.30 into the RTE reveals that this is the case. This property have been noted and exploited by several authors, for example [84–86] and will be used both in Chapter 3 and 4.

Chapter 3

Monte Carlo

The Monte Carlo (MC) method is a simple and widely used technique to solve many types of problems in, for example, physics and mathematics. As suggested by the name, the method relies on sampling stochastic (random) variables and/or simulations of stochastic processes. That is, it relies on random numbers to estimate the solution of the given problem. It is also a numerical method, typically relying on computers to carry out the necessary calculations.

A good one-sentence description, by Dunn and Shultis, catches the essence of Monte Carlo: *"The analysis technique called Monte Carlo is, in essence, a methodology to use sample means to estimate population means."* [87]. Fig. 3.1 illustrates how MC can be used to estimate a distribution. In this example, the distribution is simple, but the MC method is capable of estimating distributions originating from problems lacking analytical or deterministic numerical solutions. As the number of observations, N, increase the MC estimate approaches the true distribution. That is, in the limit of infinite number of observations, $N \to \infty$, the MC solution is an exact method. In practice, a finite number of observations is always used. The solution is still exact, but influenced by statistical noise.

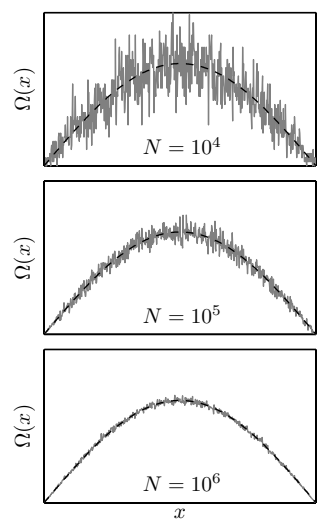

Figure 3.1. *Estimation of a distribution, $\Omega(x)$, using Monte Carlo. The dashed line represents the true distribution and the solid grey lines are the estimates of this distribution, sampled using MC.*

Turning to transport of light in turbid media, the distributions of interest are, for example, the spatial distribution of absorbed energy in tissue resulting from a laser pulse, or the temporal distribution of light transmitted through a pharmaceutical sample. An estimate of the distribution calculated by "sampling" the RTE using random numbers. This will be described in the next section. As MC gives an exact, albeit noisy, solution to the RTE and can handle any geometry, it is often considered the gold standard model of light propagation in turbid materials. As the MC method is subject to the same approximations as the underlying equation being solved, a more correct statement would be to consider MC

a gold standard technique for solving the RTE.

For an introduction to Monte Carlo in general the book by Dunn and Shultis is recommended [87]. For MC applied to biophotonics the book by Welch and van Gemert [60] and the thesis of Prahl [88] provides good starting points.

3.1 Introduction

The use of the Monte Carlo method to model light transport in tissue, was introduced by Wilson and Adam in 1983 [89]. Before that, the MC method had been used to study radiation transport in other fields, for example neutron transport in nuclear reactors [90]. The main idea is to reformulate the RTE (Eq. 2.29) as an equation describing transport of scalar particles. The density of such particles, propagating in direction $\hat{\mathbf{s}}$, $N = N(\mathbf{r}, \hat{\mathbf{s}}, t)$ [1/m^{3}sr], relates to the radiance

$$N(\mathbf{r}, \hat{\mathbf{s}}, t) = \frac{L(\mathbf{r}, \hat{\mathbf{s}}, t)}{Ev}, \tag{3.1}$$

where E is the energy per particle. Now the RTE reads

$$\frac{1}{v}\frac{\partial N}{\partial t} = Q + \mu_s \int_{4\pi} p(\hat{\mathbf{s}}', \hat{\mathbf{s}}) N d\omega' - \hat{\mathbf{s}} \cdot \nabla N - N(\mu_s + \mu_a), \tag{3.2}$$

where $Q = q/Ev$ [1/sm^{3}sr] is the number of particles emitted per unit time, volume and steradian. Applying the MC method to the radiation transport problem described by Eq. 3.2 is now a matter of tracing particles, from the source described by Q, through the turbid medium. Inside the medium, the particles are scattered and absorbed (with probabilities μ_s and μ_a per unit length), until they are absorbed or exit the region of interest. If this procedure is done for a large number of particles, the traces for these particles may be considered a good estimate of how the entire population (all particles) behaves and the transport problem has thus been solved. The number of particles needed to be traced varies significantly with the exact problem and the variance reduction techniques applied (see Section 3.3), but is generally in the order of $10^4 - 10^9$ particles [91]. This constitutes a heavy computational burden making the technique useless for anything but computers.

In the field of biomedical optics, many groups have developed MC codes solving more or less specific tasks. The code MCML by Wang *et al.* solving the steady-state light transport problem in multilayered media [91, 92], is probably the most well known and is often used as a starting point for custom codes. Calculating time-resolved responses of arbitrary 3D media, the tMCimg code by Boas *et al.* [93] has also served a similar purpose for the community.

3.1.1 The photonic confusion

One of the great advantages of the MC method is that the solution is very intuitive. The problem of solving a difficult equation has been reduced to a task of tracking particles "bouncing around" in a medium. However, great care must be taken when implementing and interpreting MC simulations, remembering the underlying assumptions of the problem to be solved and the relations between that problem and the actual physical processes.

One great misconception related to MC, concerns to the particles introduced in Eq. 3.2. It is tempting, and very common, to say that these particles are photons. However, these particles have nothing to do with the photons of quantum physics[1]. In fact, the particles are just a fiction of the solution method (MC), not real physical particles. Similarly, MC is just a (mathematical) way of solving the RTE, not a simulation of an actual physical process. For further discussions on this "photonic confusion" see the work by Mishchenko and references therein [20, 64].

The photonic terminology is common in the field of biomedical optics, as well as in other fields. This unfortunate terminology was, to some extent, used in Papers **I**,**II**,**III**, and **VI**.

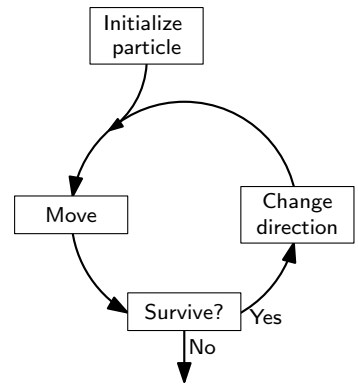

Figure 3.2. *A flowchart for a simple MC algorithm, tracing a single particle.*

3.2 Monte Carlo basics

A flowchart of a basic MC algorithm, calculating a sample of the RTE, is shown in Fig. 3.2. Details of the individual steps are given below.

Initialize the particle

The particle is initialized, or launched, in accordance with the source term, Q. The position of the particle is set to that of the source, typically at the origin of the local coordinate system, and the initial direction is set. Commonly used sources include the infinitely narrow collimated beam of particles, incident normal to a surface, and the isotropic source, where the initial direction is randomized evenly over 4π solid angles.

Move the particle

The particle will now take a step in the current direction. The length of this step is decided by the absorption and scattering coefficients, μ_a and μ_s respectively. Both coefficients describe the

[1] Without moving into quantum electrodynamics, a topic far outside the scope of this thesis, it may be mentioned that there, strictly speaking, is no such thing as a wave function for a photon and that photons [94]. Photons may thus not be localized in any classical sense.

interaction probability per unit length which leads to an exponential distribution of step lengths. The length of the step to take to the next scattering event is thus:

$$s_s = -\frac{\ln(\xi)}{\mu_s}, \tag{3.3}$$

where ξ is a random number, uniformly distributed in the interval $\xi \in (0, 1]$. Similarly, the length of the step to take to the next absorption even is:

$$s_a = -\frac{\ln(\xi)}{\mu_a}. \tag{3.4}$$

Note that ξ, being a random number, changes every time it is used in the algorithm.

If $s_a < s_s$ the particle will reach the absorption event before the scattering event and the particle is absorbed after the step. Otherwise, if $s_s < s_a$, the scattering event is reached first and the algorithm proceeds. The above implementation relies on the fact that the absorption process is *memoryless*. The process does not care how far the particle has already travelled, the only thing that matters is that the probability of absorption per unit length travelled is μ_a. The process described above will therefore lead to an exponential distribution of lengths travelled before absorption, in agreement with Beer-Lamberts law (Eq. 2.27).

Change direction

When the particle reaches a scattering event the particle changes direction according to the scattering phase function $p(\hat{\mathbf{s}}', \hat{\mathbf{s}})$. Here, the scattering phase function is reinterpreted as a probability density function (PDF) describing the probability that a particle, travelling in direction $\hat{\mathbf{s}}'$, to be scattered into direction $\hat{\mathbf{s}}$ when interacting with a scattered. As discussed in Section 2.2.4, it is commonly assumed that p is independent of the current direction, $\hat{\mathbf{s}}'$, and that the new direction can be characterized by the deflection angle θ and the azimuthal angle ϕ, which are independent. The azimuthal angle is uniformly distributed in $\phi \in (0, 2\pi]$:

$$\phi = 2\pi\xi. \tag{3.5}$$

A commonly used distribution for the deflection angle is the Henyey-Greenstein distribution [41] (Eq. 2.24) which is sampled, using the uniform random number ξ, from the expression:

$$\cos\theta = \frac{1}{2g}\left(1 + g^2 - \left(\frac{1 - g^2}{1 - g + 2g\xi}\right)^2\right). \tag{3.6}$$

In case of isotropic scattering ($g = 0$) Eq. 3.6 is undefined and the correct expression is instead

$$\cos\theta = 2\xi - 1. \tag{3.7}$$

The new direction of the particle is now calculated from the two angles θ and ϕ.

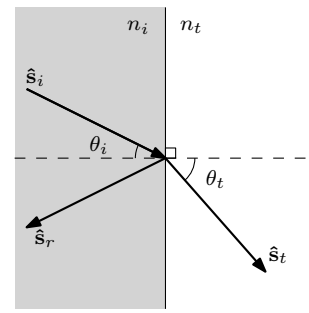

Figure 3.3. *A particle propagating in direction $\hat{\mathbf{s}}_i$ incident on a boundary. The particle is either reflected or transmitted, resulting in a direction change to $\hat{\mathbf{s}}_r$ or $\hat{\mathbf{s}}_t$ respectively.*

Boundary conditions

By tracing particles in the process described above, keeping track of where the particles have been or where they were absorbed, MC provides a way to solve the RTE in an infinite medium. However, in many cases the medium is not infinite and a way to handle transitions between different materials is needed. In the limit of geometrical optics, *i.e.* all spatial features are much larger than the wavelength, the transition between to regions with refractive indices n_i and n_t may be described by Fresnel reflection. The Fresnel reflection coefficient, $R(\theta_i)$, averaged over different polarization directions, is

$$R(\theta_i) = \frac{1}{2}\left(\frac{\sin^2(\theta_i - \theta_t)}{\sin^2(\theta_i + \theta_t)} + \frac{\tan^2(\theta_i - \theta_t)}{\tan^2(\theta_i + \theta_t)}\right), \tag{3.8}$$

where θ_i and θ_t are the angles of incidence and transmission respectively (see Fig. 3.3) calculated using Snell's law

$$n_i \sin\theta_i = n_t \sin\theta_t. \tag{3.9}$$

In case the step length, $s = \min(s_s, s_a)$, is longer than the step required to reach a boundary the particle is moved to the boundary. There, a uniformly distributed random number is compared to the reflection coefficients; if $\xi > R(\theta_i)$ the particle is transmitted and changes direction according to Eq. 3.9, otherwise the particle is reflected of the boundary. After this the process continues as usual.

Time-domain simulations

Time-domain simulations are easily accommodated in the current scheme. At initialization the time for the particle is set to zero. After each step the time is incremented by step length divided by the current velocity of the particle, v.

3.3 Variance reduction techniques

The MC process described in the previous section is a simple, yet rigorous, way to solve the radiative transport problem. It is, however, rarely applied in the way described above. Consider, for example, a material with $\mu_s \approx \mu_a$, where the solution far away from the source is of interest. It is evident that few particles will take more than a few steps before being absorbed, hence requiring a large amount of particles to be simulated for the MC method to provide a solution with acceptable statistics. To approach the

problem, several variance reduction techniques have been developed to aid the MC method in reaching less noisy solutions while tracing fewer particles. Many different such techniques exist [87], some of which are applicable to MC in general, and some of which provide significant advantages in specific problems. Two great examples of variance reduction techniques, applied to problems in biomedical optics, are [95] and [96], where efficient handling of distant sources and simulations involving fluorescence are presented, respectively. In the following sections a few variance reduction techniques, relevant to this thesis, are explained.

3.3.1 Implicit capture

Implicit capture is a very popular variance reduction technique in radiation transport MC simulations. In fact, it is so widely used that it is synonymous with MC simulation and a standard way of handling absorption, as opposed to the rigorous approach described in the previous section. It was used early by Witt [97], considering multiple scattering in nebulae, and have since found use in biomedical optics, for example by Wilson and Adam [89], Prahl [88], and in MCML [91, 92].

The implicit capture technique involves launching and tracing packets of particles instead of one by one. At launch, each packet is assigned an initial weight W_0. The packet is traced with a step length distribution determined by the total attenuation coefficient, $\mu_t = \mu_s + \mu_a$. After each step the weight of the packet is reduced by ΔW

$$W_{i+1} = W_i - \Delta W = W_i \left(1 - \frac{\mu_a}{\mu_t}\right). \tag{3.10}$$

The packets are traced until they either escape though a boundary, or until the weight reaches a threshold limit (e.g. $W_0/1000$). In order to conserve energy, the termination of the packets is handled by a so-called roulette routine. When the packet weight falls below the threshold limit, there is a one in m chance that the packet will survive. If the packet survives the roulette, its weight is increased m times. If not, the packet is terminated.

While the implicit capture technique is used in almost all available Monte Carlo codes in the biomedical optics field, it is often forgotten that, as pointed out by Swartling [98], the technique is approximative. In the limits $\mu_s/\mu_a \to 0$ and $\mu_s/\mu_a \to \infty$ the implicit capture technique converges towards the correct solution but for $\mu_s \approx \mu_a$ the technique is not equivalent to the rigorous approach. This inconsistency is briefly discussed in Paper **I**.

3.3.2 White Monte Carlo

The White Monte Carlo (WMC) technique has its foundation in two properties of the RTE:

i) To any time-resolved simulation performed with $\mu_a = 0$, absorption may be added afterwards using the Beer-Lambert law (see Section 2.4.4 and Eq. 2.30).

ii) In any simulation performed with $\mu_a = 0$, the scattering coefficient, μ_s, may be rescaled by rescaling the spatial and temporal coordinates. In certain simple geometries lacking spatially dependent features, such as infinite and semi-infinite media, this method proves particularly useful. The scaling relations are illustrated in Fig. 3.4.

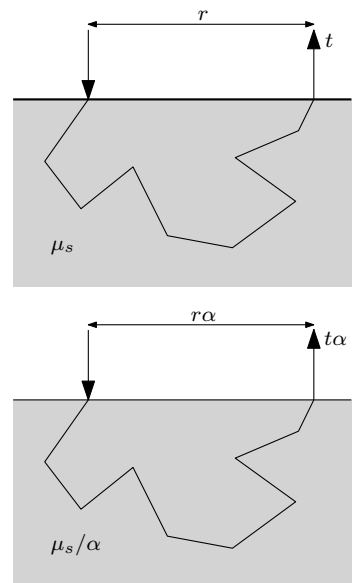

Figure 3.4. *The particle paths are determined by the scattering coefficient, the scattering phase function and the sequence of random numbers. Using the same random number sequence while rescaling μ_s yields identical, albeit rescaled paths. All spatial distances and time are both rescaled as shown. Adapted from [99].*

Combining the two properties it is evident that the result of a single MC simulation, in an appropriate geometry, may be rescaled and attenuated to accommodate any combination of μ_s and μ_a. The rescaling is virtually instantaneous, allowing the otherwise slow MC-method to be applied to iterative inverse problems. The scaling properties of MC simulations, and possible combination with the Beer-Lambert law, have been mentioned or investigated theoretically by several authors [89, 96, 99–103]. In Paper **I** a WMC model was implemented and used in evaluation of TOFS data. The scaling effect, mentioned by Xu *et al.* [103], was overcome by detecting particles individually and it was shown that MC-based evaluation significantly improve the performance of TOFS in interstitial geometries. Paper **VI** extends the investigations to the semi-infinite case, resulting in an important contribution in the characterization of the MEDPHOT-phantoms [104]. In Paper **IV** the model introduced in Paper **I** was used to evaluate *in vivo* data from human prostate, solving the modelling related problem in a previous study [105].

3.3.3 Spatial convolutions

Simulating a spatially extended source, *e.g.* a Gaussian beam incident on a semi infinite medium, it is evident that accounting for the source size in the packet initialization stage is not a particularly efficient strategy. Instead, running a simulation with a spatial impulse source (collimated beam) and convolving the solution with the source shape, has the potential of significantly reducing the noise in the direction of the convolution [88, 106]. In addition, as any spatial features scales with the rescaling of μ_s, the convolution method provides a way to handle extended sources in the WMC scheme. A convolution method to handle extended sources and detectors was thus used in Paper **I**.

3.4 Hardware accelerated Monte Carlo

The variance reduction techniques described in Section 3.3 are all mathematical/numerical tricks or simplifications that help reduce the variance in the MC solutions for a fixed number of traced particles, hence reducing the computational time required to reach a solution with a certain variance. Another approach to speed up the simulation time is to accelerate the computations themselves by using faster and/or more efficient hardware.

Zolek *et al.* investigated approximations of trigonometric and logarithmic functions, optimizing MC code for the calculations modern CPUs are good at, providing a $\sim 4\times$ speedup [107] . Using field programmable gate arrays (FPGAs) Lo *et al.* achieved $\sim 40\times$ speedup compared to a high-end CPU [108].

However, the key to even faster simulations lie in the move from serial to parallel computations. Considering the basic MC routine described in Section 3.2 it is obvious that the particles does not interact with each other, nor do they change the medium in which they travel, *i.e.* the traces of individual particles are independent. This independence implies that the particles may be traced in parallel as opposed to serially or simultaneously. Early parallelization of MC code was done using clusters of computers connected over a network [109, 110]. Shen and Wang recently exploited the streaming SIMD extensions (SSE), a set of instructions for x86 CPUs for doing parallel computations, and the multiple cores available in modern CPUs to speed up MC-simulations [111]. While the benefit of such an effort is significant, the effort to write such highly specialized code can be put to better use by writing code for an architecture designed for parallel computations.

3.4.1 GPU-accelerated Monte Carlo

In recent years, GPUs have evolved from highly specialized hardware to a general purpose parallel computation unit [112, 113]. In Paper **II**, GPUs were, for the first time, used to accelerate MC simulations of light propagation in turbid media, resulting in a $1000\times$ speedup over the conventional CPU-based approach.

In CPUs, a steady flow of instructions and data must be maintained in order for the processor to be used optimally. This is achieved using caching, branch prediction etc. In GPUs the silicon, and power, is used to achieve high raw computational power and high bandwidth for parallel operations, resulting in significantly higher computational performance as long as all operations can be done in an organized and parallel manner. As shown in Paper **II** this is the case for simple radiative transport problems. For more advanced problems, such recording the internal spatial distribution of absorbed energy as done by MCML, utilizing the parallel nature of the GPU becomes more tricky. The major prob-

lem lies in the implicit capture variance reduction technique where every particle have to write (deposit the absorbed weight) to a random position in memory every step, an operation unsuitable for parallelization. This, and other problems of how to best utilize GPUs for MC simulations is the topic of Paper **III**. It is shown that the proper use of the features of modern GPUs allow complex simulation problems to be solved several orders of magnitude faster on GPUs compared to modern CPUs. Moreover, it should be emphasized, that in many applications where simulation speed is of importance, such as iterative data evaluation, the entire spatial distribution inside a medium is rarely of interest. Considering *e.g.* only light exiting a medium, each particle requires only a single random memory write, instead of one per step, completely eliminating the problem.

The benefits of using GPU-accelerated Monte Carlo, combined with the very rapid development of new and significantly improved GPUs, suggest that GPU MC will become a standard method in radiative transport MC problems. Since Paper **II** several authors have made contributions to the field and several codes and tools have been made publicly available *e.g.* [114–119].

The use of GPU-accelerated MC enabled the simulation performed in Paper **IX**. There, the amount of particles re-entering a small fibre inserted in an infinite, scattering medium was studied. The results of such an MC simulation was used in the evaluation of TOFS data from a single-fibre setup.

Chapter 4

Diffusion Theory

In this chapter diffusion theory of light transport is discussed. First the traditional derivation of the *diffusion equation* (DE) from RTE is outlined, followed by a discussion of the approximations made in the derivation. In order to understand the approximations, the diffusion equation is also derived using an intuitive random walk approach, providing better understanding of the approximations. The approximations, and the validity of diffusion theory, from the point of view of the alternative derivation, are discussed. The purpose of this is to highlight the need to use better light transport models (*e.g.* Monte Carlo) in many domains of light transport where diffusion theory fails to accurately model the physics.

Finally, solutions to the DE and anisotropic diffusion are briefly discussed.

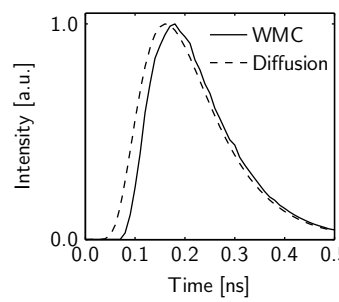

Figure 4.1. *Illustration of the breakdown of diffusion theory. Despite using the same optical properties, the solution provided by diffusion theory deviates significantly from that of a Monte Carlo simulation (Infinite geometry, 15 mm source-detector separation, $\mu_s' = (1-g)\mu_s$=7.5 cm^{-1} and μ_a=0.5 cm^{-1}). Adapted from Paper* **I**.

4.1 Introduction

Diffusion theory is a popular and widely used model of light transport in turbid media. As shown in the next section, under certain approximations the RTE reduces to a simple diffusion equation, providing simple and numerically inexpensive, or even analytical, solutions to the light transport problem. The drawback of diffusion theory is limited validity. Under certain conditions *e.g.* high absorption and/or weak scattering , diffusion theory breaks down. This breakdown of diffusion theory, noted and discussed by many authors *e.g.* [57, 120–124], is illustrated in Fig. 4.1. However, in many applications, diffusion theory is a sufficiently good model. In order to know when diffusion may and may not be applied, it is imperative to understand the underlying assumptions and approximations of the theory. An attempt at explaining the approximations is given in the following sections. Alternatively, as explored in Papers **I**, and **VI**, the breakdown of diffusion theory may be

quantified using numerical and experimental investigations.

4.2 The P1- and diffusion-approximation

In this section, the derivation of the diffusion equation, following the derivation by Durduran *et al.* [86], is outlined. For more details the reader is directed to any of the many sources providing such, *e.g.* [23, 86, 125]. Here, as explored in [86], the diffusion equation is derived in the absence of absorption. As explained in Section 2.4.4, absorption may always be added at a later stage.

In order to reduce the RTE to a diffusion equation, the radiance is expanded in an infinite series of spherical harmonics. The series is then truncated in the so called P_N-approximation, keeping only the terms up to Nth order. In the P_1-approximation only the zeroth and first order terms are kept

$$L(\mathbf{r}, \hat{\mathbf{s}}, t) \approx \frac{1}{4\pi}\Phi(\mathbf{r}, t) + \frac{3}{4\pi}\mathbf{F}(\mathbf{r}, t) \cdot \hat{\mathbf{s}}, \tag{4.1}$$

where

$$\Phi(\mathbf{r}, t) = \int_{4\pi} L(\mathbf{r}, \hat{\mathbf{s}}, t) d\omega, \tag{4.2}$$

is the *fluence rate* [W/m^2] and

$$F(\mathbf{r}, t) = \int_{4\pi} L(\mathbf{r}, \hat{\mathbf{s}}, t)\hat{\mathbf{s}} d\omega, \tag{4.3}$$

is the *flux* [W/m^2]. Further, the source is assumed to be isotropic

$$q(\mathbf{r}, \hat{\mathbf{s}}, t) = \frac{1}{4\pi} q_0(\mathbf{r}, t) \quad [\mathrm{W/m^3}]. \tag{4.4}$$

Inserting Eq. 4.1 and Eq. 4.4 into the RTE (Eq. 2.29, with $\mu_a = 0$) yields two coupled equations; one by integrating over all $\hat{\mathbf{s}}$ and the other by first multiplying by $\hat{\mathbf{s}}$ before integrating over all $\hat{\mathbf{s}}$.

$$\frac{1}{v}\frac{\partial \Phi(\mathbf{r}, t)}{\partial t} + \nabla \mathbf{F}(\mathbf{r}, t) = q_0(\mathbf{r}, t), \tag{4.5}$$

$$\left(\frac{1}{v}\frac{\partial}{\partial t} + \mu_s'\right)\mathbf{F}(\mathbf{r}, t) + \frac{1}{3}\nabla\Phi(\mathbf{r}, t) = 0, \tag{4.6}$$

where the property described in Eq. 2.25 was used. Also, a new coefficient, called the *reduced scattering coefficient*[1], $\mu_s' = (1-g)\mu_s$ [m^{-1}], was introduced. Assuming that the temporal change in flux

[1] μ_s' is also called the *transport scatting coefficient* and may be interpreted as the equivalent scattering coefficient when the scattering is isotropic ($g = 0$). The reduced scattering coefficient relates to the *transport mean free path* $\ell^* = 1/\mu_s'$ [m].

is negligible, *i.e.* $\partial\mathbf{F}/\partial t = 0$, Eq. 4.6 reduces to Fick's first law of diffusion

$$\mathbf{F}(\mathbf{r},t) = -\frac{1}{v} D \nabla \Phi(\mathbf{r},t), \tag{4.7}$$

where D is the *diffusion coefficient*[2] [m^2/s]

$$D = \frac{v}{3\mu_s'}. \tag{4.8}$$

Inserting Eq. 4.7 into Eq. 4.5 yields the diffusion equation (DE)

$$\frac{\partial \Phi(\mathbf{r},t)}{\partial t} - \nabla D(\mathbf{r}) \nabla \Phi(\mathbf{r},t) = v q_0(\mathbf{r},t). \tag{4.9}$$

The solution to the diffusion equation, in an infinite three-dimensional medium with $D(\mathbf{r}) = D$ and $q_0(\mathbf{r},t) = E_0 \delta_r \delta_t$ is

$$\Phi(r,t) = v E_0 \left(4\pi D t\right)^{-3/2} \exp\left(\frac{-r^2}{4Dt}\right). \tag{4.10}$$

4.2.1 Assumptions and simplifications

The assumptions and simplifications made in the derivation of the DE are not always easy to follow. A few simplifications, such as the P_1-truncation and ignoring the contribution of $\partial\mathbf{F}/\partial t$ are explicit but are not easily interpreted. In addition, it is often claimed, with varying motivations, that in order for diffusion to be valid, the scattering must dominate the absorption, $\mu_s' \gg \mu_a$, and that solutions are only valid far from the source, see *e.g.* [60]. These two restrictions, along with an alternative view on the truncation will be explained in the following sections.

The assumption $\partial\mathbf{F}/\partial t = 0$ have been investigated by several authors [86, 121, 126], concluding that the assumption is valid for frequencies[3] $\omega \ll \mu_s' c$.

If the DE is derived without assuming $\mu_a = 0$, a diffusion coefficient $D = v/(3(\mu_s' + \mu_a))$ is reached, which is in violation of the property of the RTE discussed in Section 2.4.4. The issue has been thoroughly discussed by several authors [85, 86, 127–129] promoting the definition in Eq. 4.8. Pierrat *et al.* concluded that, in time-domain solutions, the diffusion coefficient indeed is independent of absorption, but that in, steady state, it is not [130].

[2] In the field of biomedical optics diffusion coefficient is often denoted $D = 1/(3\mu_s')$ [m] which is more accurately described as the diffusion length.

[3] The frequency, ω, is related to time via the Fourier transform. See Section 5.3.3 for a brief introduction to frequency-domain measurements.

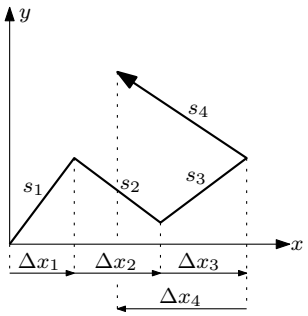

Figure 4.2. *Four steps of a random walk in two dimensions. Each step is s_i long and the projection of the step onto the x-axis is Δx_i. Note that Δx_i may be either positive or negative, depending on the direction of the step.*

4.3 Alternative derivation

In order to better understand the approximations made to reach the diffusion equation (Eq. 4.9), here, an alternative derivation is presented, based on the early work on random walks by Bachelier [131] and Einstein [132]. An excellent tutorial covering the subject is provided by Vlahos *et al.* [133]. The book by Hughes is also recommended [134].

Consider an ensemble of particles, walking randomly in 3 dimensions. The particles takes short steps of random length, s, where s is considered a random variable. The average time for each step is $\langle \Delta t \rangle = \langle s/v \rangle$, where $\langle\ \rangle$ denotes the expectation value (or average). The spatial distribution of particles, at time t, in a fixed direction, for example, the x-direction in a Cartesian coordinate system, is described by $f(x,t)$ [m^{-1}]. The projections of the steps onto this axis are denoted Δx, see Fig. 4.2. Δx is a random variable with a distribution given by the function $q_{\Delta x}(\Delta x)$. $q_{\Delta x}(\Delta x)$ is a probability density function, which is normalized

$$\int_{-\infty}^{+\infty} q_{\Delta x}(\Delta x) d\Delta x = 1. \tag{4.11}$$

Also, while the steps Δx_i and Δx_{i+1} generally are dependent, the expectation value of Δx is zero

$$\langle \Delta x \rangle = 0. \tag{4.12}$$

This is easily realized by noting that for an isotropic distribution of particle directions, $q_{\Delta x}(\Delta x)$ is symmetric, $q_{\Delta x}(\Delta x) = q_{\Delta x}(-\Delta x)$ (this will be further explained in Appendix A).

Assuming that the time to complete a step, $\langle \Delta t \rangle$, is constant the distribution of particles after a step relates to the distribution before the step like:

$$f(x, t + \langle \Delta t \rangle) = \int_{-\infty}^{+\infty} f(x + \Delta x, t) q_{\Delta x}(\Delta x) d\Delta x. \tag{4.13}$$

If the step Δx is small, $f(x + \Delta x, t)$ may be expanded in a Taylor series around x.

$$f(x + \Delta x, t) = f(x,t) + \Delta x \frac{\partial f(x,t)}{\partial x} + \frac{\Delta x^2}{2!} \frac{\partial^2 f(x,t)}{\partial x^2} + \dots \tag{4.14}$$

Inserting Eq. 4.14 into Eq. 4.13, yields

$$\begin{aligned} f(x, t + \langle \Delta t \rangle) = & \int_{-\infty}^{+\infty} f(x,t) q_{\Delta x}(\Delta x) d\Delta x \\ & + \int_{-\infty}^{+\infty} \Delta x \frac{\partial f(x,t)}{\partial x} q_{\Delta x}(\Delta x) d\Delta x \qquad (4.15) \\ & + \int_{-\infty}^{+\infty} \frac{\Delta x^2}{2!} \frac{\partial^2 f(x,t)}{\partial x^2} q_{\Delta x}(\Delta x) d\Delta x + \ldots \\ = & f(x,t) \int_{-\infty}^{+\infty} q_{\Delta x}(\Delta x) d\Delta x \\ & + \frac{\partial f(x,t)}{\partial x} \int_{-\infty}^{+\infty} \Delta x q_{\Delta x}(\Delta x) d\Delta x \qquad (4.16) \\ & + \frac{1}{2!} \frac{\partial^2 f(x,t)}{\partial x^2} \int_{-\infty}^{+\infty} \Delta x^2 q_{\Delta x}(\Delta x) d\Delta x + \ldots \end{aligned}$$

The integral terms in Eq. 4.16 are simply the central moments[4] of the distribution $q_{\Delta x}(\Delta x)$. Since $q_{\Delta x}(\Delta x)$ is symmetric, all the odd order central moments are zero. The zeroth order central moment is equal to unity (Eq. 4.11) and the second central moment is the variance[5] of the step length distribution

$$\int_{-\infty}^{+\infty} \Delta x^2 q_{\Delta x}(\Delta x) d\Delta x = \sigma^2_{\Delta x}. \qquad (4.17)$$

Truncating the series in Eq. 4.16 to include only the first two non-zero moments gives:

$$f(x, t + \langle \Delta t \rangle) \approx f(x,t) + \frac{\sigma^2_{\Delta x}}{2} \frac{\partial^2 f(x,t)}{\partial x^2}. \qquad (4.18)$$

[4] The k:th central moment, μ_k, of a distribution $f(x)$ is given by

$$\mu_k = \int_{-\infty}^{+\infty} x^k f(x) dx.$$

[5] The variance, σ^2, of a distribution $f(x)$ is

$$\sigma^2 = \int_{-\infty}^{+\infty} (x - \langle f(x) \rangle)^2 f(x) dx.$$

Since $\langle \Delta x \rangle = 0$ (Eq. 4.12), for the distribution $q_{\Delta x}(\Delta x)$ the variance is equal to the second central moment, $\sigma^2 = \mu_2$.

Rearranging and dividing both sides by $\langle \Delta t \rangle$ gives

$$\frac{f(x, t + \langle \Delta t \rangle) - f(x, t)}{\langle \Delta t \rangle} = \frac{\sigma^2_{\Delta x}}{2\langle \Delta t \rangle} \frac{\partial^2 f(x, t)}{\partial x^2}. \tag{4.19}$$

Identifying the left hand side of Eq. 4.19 as the definition of the derivative (when $\langle \Delta t \rangle \to 0$, which is true as $\langle \Delta t \rangle$ is assumed small) a 1D-diffusion equation is reached

$$\frac{\partial f(x, t)}{\partial t} = D_x \frac{\partial^2 f(x, t)}{\partial x^2}, \tag{4.20}$$

with the diffusion coefficient

$$D_x = \frac{\sigma^2_{\Delta x}}{2\langle \Delta t \rangle}. \tag{4.21}$$

The solution to Eq. 4.20 in infinite space, where the source is an isotropic pulse of unitary strength ($q_0(x, t) = \delta_x \delta_t$) is a Gaussian

$$f(x, t) = \frac{1}{\sqrt{4\pi D_x t}} \exp\left(\frac{-x^2}{4 D_x t}\right), \tag{4.22}$$

where $f(x, t)$ is the probability to find a particle at x at time t.

While the steps of an individual particle in different directions clearly are dependent, the behaviour of the distribution of particles is not. Hence, the probability to find a particle at $\mathbf{r}$ (*i.e.* in 3 dimensions) at time t is

$$\begin{aligned} f_{3D}(\mathbf{r}, t) &= f(x, t) * f(y, t) * f(z, t) \\ &= \frac{1}{\sqrt{4\pi D_x t}} \exp\left(\frac{-x^2}{4 D_x t}\right) * \frac{1}{\sqrt{4\pi D_y t}} \exp\left(\frac{-y^2}{4 D_y t}\right) \\ &\quad * \frac{1}{\sqrt{4\pi D_z t}} \exp\left(\frac{-z^2}{4 D_z t}\right) \\ &= (4\pi t)^{-3/2} (D_x D_y D_z)^{-1/2} \\ &\quad * \exp\left[-\frac{1}{4t}\left(\frac{x^2}{D_x} + \frac{y^2}{D_y} + \frac{z^2}{D_y}\right)\right]. \end{aligned} \tag{4.23}$$

The particle concentration, ρ, is $\rho(\mathbf{r}, t) = N f_{3D}(\mathbf{r}, t)$ [m^{-3}], where N is the number of particles launched. Further the relationship between the particle concentration and the fluence is given by

$$\Phi(\mathbf{r}, t) = v E \rho(\mathbf{r}, t) = v E_0 f_{3D}(\mathbf{r}, t), \tag{4.24}$$

where E is the energy per particle and $E_0 = EN$ is the total energy launched. In isotropic media ($D_x = D_y = D_z = D$) and with, $x^2 + y^2 + z^2 = r^2$, Eq. 4.23 may be written (compare with Eq. 4.10)

$$\Phi(r, t) = v E_0 (4\pi D t)^{-3/2} \exp\left(\frac{-r^2}{4Dt}\right). \tag{4.25}$$

4.3.1 The diffusion coefficient

While the two different ways of deriving the DE in the previous sections reach the same expression for the DE and its solution in infinite isotropic media, the expressions for the diffusion coefficient (Eq. 4.8 and Eq. 4.21) are not obviously identical. Here, a random walk-approach to the diffusion coefficient is presented, based on the tutorial by Vlahos *et al.* [133]. The approach was also explored by Zaccanti *et al.* [135] and Gandjbakhche *et al.* [136]

Consider a single particle doing a random walk in 3 dimensions. Using a Cartesian coordinate system, the position of the particle along one of the directions, for example, the x-direction, after n steps, is

$$x_n = \Delta x_1 + \Delta x_2 + \Delta x_3 + ... + \Delta x_n = \sum_{k=1}^{n} \Delta x_k, \tag{4.26}$$

where the increments Δx_i are random variables as illustrated in Fig. 4.2.

The mean square displacement $\langle x_n^2 \rangle$ is simply the mean of Eq. 4.26 squared:

$$\langle x_n^2 \rangle = \langle (\Delta x_1 + \Delta x_2 + ... + \Delta x_n)^2 \rangle. \tag{4.27}$$

In this context, as $\langle x_n \rangle = 0$, the mean square displacement of a single particle is the same as the variance for the particle distribution.

Now, considering the solution to the 1D-diffusion equation, Eq. 4.22, it is apparent that the solution is identical to a Gaussian (normal) distribution with mean zero and variance $2D_x t$. Since the variance of the distribution is $\langle x_n^2 \rangle$ it follows that

$$\langle x^2(t) \rangle = 2D_x t. \tag{4.28}$$

It was previously assumed that $t = n\langle \Delta t \rangle$, where n is the number of steps and $\langle \Delta t \rangle$ is the mean of the step time distribution. Hence

$$\langle x_n^2 \rangle = 2D_x n \langle \Delta t \rangle, \tag{4.29}$$

or

$$D_x = \frac{\langle x_n^2 \rangle}{2n\langle \Delta t \rangle}. \tag{4.30}$$

The problem of calculating the diffusion coefficient is thus a matter of calculating $\langle x_n^2 \rangle$. Using an elementary rule of arithmetics of random variables[6] Eq. 4.27 may be written

$$\langle x_n^2 \rangle = \sum_{j=1}^{n} \left(\sum_{k=1}^{n} \langle \Delta x_j \Delta x_k \rangle \right). \tag{4.31}$$

[6] If X and Y are random variables (dependent or independent), $\langle X+Y \rangle = \langle X \rangle + \langle Y \rangle$ holds.

When $\langle \Delta x_i \rangle = 0$, the expectation value $\langle \Delta x_j \Delta x_k \rangle$ is the covariance[7] of the two random variables, Δx_j and Δx_k. The covariance matrix, Σ_{jk} is

$$\Sigma_{jk} = \mathrm{cov}(\Delta x_j, \Delta x_k) = \langle \Delta x_j \Delta x_k \rangle. \tag{4.32}$$

Eq. 4.31 simply is the sum of all the elements in the covariance matrix Σ_{jk}. Details on how to calculate and sum the covariance matrix is available in Appendix A. Here the important results are summarized.

For isotropic scattering ($g = 0$) the sum of the covariance matrix, and hence the variance of the particle distribution after n steps, becomes

$$\langle x_n^2 \rangle = n \langle \Delta x_i^2 \rangle = \frac{2n}{3\mu_s^2}. \tag{4.33}$$

Assuming constant transport speed, v, the time each step takes is $\Delta t_i = s_i / v \Rightarrow \langle \Delta t \rangle = 1/(v\mu_s) = \ell / v$.

Using Eq. 4.30 the diffusion coefficient for isotropic scattering may be calculated:

$$D_x = \frac{\langle x_n^2 \rangle}{2n\langle \Delta t \rangle} = \frac{\frac{2n}{3\mu_s^2}}{2n\frac{1}{v\mu_s}} = \frac{v}{3\mu_s}, \tag{4.34}$$

or, noting that $\sigma_{\Delta x}^2 = \langle \Delta x_i^2 \rangle$

$$D_x = \frac{\langle x_n^2 \rangle}{2n\langle \Delta t \rangle} = \frac{n\langle \Delta x_i^2 \rangle}{2n\langle \Delta t \rangle} = \frac{\sigma_{\Delta x}^2}{2\langle \Delta t \rangle}. \tag{4.35}$$

Eq. 4.34 and Eq. 4.35 correspond to Eq. 4.8 (with $g = 0$) and Eq. 4.21 respectively and their equality have thus been shown.

In case of anisotropic scattering ($g \neq 0$) the sum of the covariance matrix can be calculated approximately

$$\langle x_n^2 \rangle = \sum_{j=1}^{n} \left(\sum_{k=1}^{n} \Sigma_{jk} \right) \overset{n \gg 1}{\approx} \frac{2n}{3\mu_s^2(1-g)}. \tag{4.36}$$

Using the approximative sum, the diffusion coefficient for anisotropic scattering is

$$D_x = \frac{\langle x_n^2 \rangle}{2n\langle \Delta t \rangle} = \frac{\frac{2n}{3\mu_s^2(1-g)}}{2n\frac{1}{v\mu_s}} = \frac{v}{3\mu_s(1-g)} = \frac{v}{3\mu_s'}, \tag{4.37}$$

which is the same as Eq. 4.8.

[7] The covariance of two random variables, X and Y is: $\mathrm{cov}(X,Y) = \langle (X - \langle X \rangle)(Y - \langle Y \rangle) \rangle = \langle XY \rangle - \langle X \rangle \langle Y \rangle$

Fig. 4.3 illustrates how the exact variance ($\langle x_n^2 \rangle$), calculated using Eq. A.19, grows with time for different values of g while the reduced scattering coefficient is fixed at $\mu_s' = 10$ cm^{-1}. In the approximation $n \gg 1$, (Eq. A.13) the variance is independent of g, *i.e.* regardless of g the variance is expected to follow the line for $g = 0$. Except for very early times, this is a good approximation.

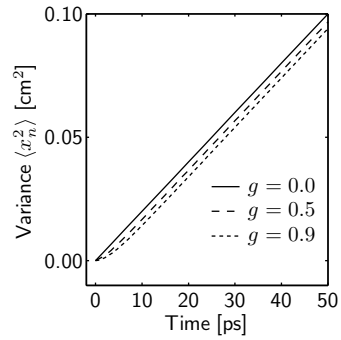

Figure 4.3. *The exact variance, $\langle x_n^2 \rangle$, calculated using Eq. A.19. The reduced scattering coefficient was fixed at $\mu_s' = 10$ cm^{-1} and the transport velocity was set to c. For different values of g, a small difference is found for early times but for larger times the difference is negligible.*

4.4 Aspects of the diffusion approximation

The alternative derivation of the diffusion equation along with the derivation of the diffusion equation reveals valuable information on the approximations and simplifications made that are not obvious when taking the conventional approach. In this section aspects of the diffusion equation, its solution and the approximations made to derive it are discussed in light of the alternative derivation.

4.4.1 Diffusion and the central limit theorem

The central limit theorem (CLT) states that the sum of *many* independent random variables, with finite mean and variance, tend to a Gaussian distribution. Considering Eq. 4.26 and isotropic scattering (*i.e.* independent random variables, Δx_i) it is obvious that the solution after many steps (large n) is a Gaussian, *i.e.* Eq. 4.22. In the case of anisotropic scattering, where the random variables are no longer independent, the traditional CLT does not hold. However, the CLT can be extended to include certain "weak" dependencies, see *e.g.* [137]. Also, diffusion theory suggest that the distribution will still tend to a Gaussian. As for the CLT, the first requirement for the DE is that the number of steps must be large, $n \gg 1$.

In order to investigate the number of steps required for diffusion to be valid, it is imperative to understand the approximations made in the derivation of the diffusion equation. While the implications of the P1-approximation are unclear, the approximation in Eq. 4.18 is that the higher order moments of the step length distribution are ignored. From the argument regarding the CLT, this approximation is the same as ignoring the higher order moments of the particle distribution. Since the distribution is symmetric the second most dominant moment is the fourth moment of the distribution, $\mu_4(n) = \langle x_n^4 \rangle$. It can be shown, using the same method as in Appendix A, that the fourth order moment, using the Henyey-Greenstein phase scattering function (Eq. 2.24), is exactly equal

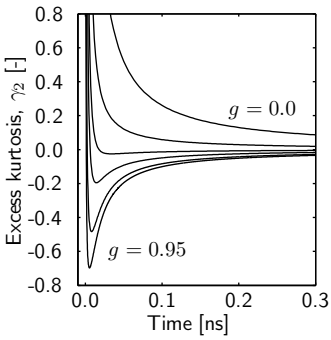

Figure 4.4. *Excess kurtosis, γ_2 as a function of time for $g = 0.0$, 0.5, 0.7, 0.8, 0.9, and 0.95. While γ_2 is independent of the scattering coefficient, μ_s a constant $\mu_s' = 10$ cm^{-1} was used to transform from number of steps n, to time t: $t = n(1-g)/(c\mu_s')$.*

to

$$\begin{aligned}\langle x_n^4 \rangle &= \sum_{i=1}^{n}\sum_{j=1}^{n}\sum_{k=1}^{n}\sum_{l=1}^{n}\langle \Delta x_i \Delta x_j \Delta x_k \Delta x_l \rangle \\ &= \frac{4}{15\mu_s^4}\frac{\left(A + nB + n^2C + g^nD + ng^nE + g^{2n}F\right)}{(g-1)^4(g+1)^2},\end{aligned} \tag{4.38}$$

where A, B, C, D, E, and F are polynomials of g

$$\begin{aligned}A &= -16g + 6g^2 + 60g^3 + 30g^4, \\ B &= 13 - 20g - 38g^2 + 20g^3 + 25g^4, \\ C &= 5 - 10g^2 + g^4, \\ D &= 16g - 6g^2 - 60g^3 - 38g^4, \\ E &= 8g - 2g^2 - 18g^3 + 2g^4 + 10g^5, \\ F &= 8g^4.\end{aligned} \tag{4.39}$$

In the derivation of Eq. 4.38, the second and third moment of the Henyey-Greenstein phase scattering function were used.

The excess kurtosis is a measure of how the fourth moment of a distribution differs from that of a normal distribution and may thus be used as a measure of the breakdown of diffusion theory. It is defined as

$$\gamma_2 = \frac{\mu_4}{\mu_2^2} - 3 = \frac{\langle x_n^4 \rangle}{\langle x_n^2 \rangle^2} - 3, \tag{4.40}$$

where $\mu_4 = \langle x_n^4 \rangle$ and $\mu_2 = \sigma^2 = \langle x_n^2 \rangle$, are the fourth and second moments of the distribution, calculated using Eq. 4.38 and A.19 respectively. The number 3 originates from the kurtosis of the Gaussian distribution. A distribution converging towards a Gaussian distribution should hence converge towards $\gamma_2 = 0$. The excess kurtosis of the spatial particle distribution in one direction is illustrated in Fig. 4.4 for $g = 0.0$ through 0.95. It is evident that the distribution converges towards a Gaussian distribution fastest for $g \approx 0.7$. For $g \gtrapprox 0.7$, $\gamma_2 < 0$ and the distribution is said to be *platykurtic*. For $g \lessapprox 0.7$, $\gamma_2 > 0$ and the distribution is *leptokurtic*.

Contrary to the intuitive result, the case with isotropic scattering, $g = 0$ where the random steps are independent, exhibit the slowest convergence. This is a result of the conversion from number of steps to time. For a fixed valued of the reduced scattering coefficient, $g = 0$ means longer and fewer steps compared to larger values of g. In conclusion, the CLT favours many, weakly dependent, steps, rather than fewer, but independent, steps. A balance between the independence of consecutive steps and the number of steps seems to be found for $g \approx 0.7$, where the excess kurtosis quickly converges to zero.

To visualize the meaning of the excess kurtosis, the spatial distributions, simulated using MC, at $t = 100$ ps, for $g = 0.0$, 0.7 and 0.95 are shown in Fig. 4.5. Here, the variance of all distributions are identical. Still, the shapes of the distributions differ from each other. A Gaussian distribution with the same variance is also shown, as this represents the solution from diffusion theory. As expected, the curve for $g = 0.7$ follow the Gaussian closely, where as the other curves deviate. This deviation between radiative transport (MC) and diffusion theory is a direct consequence of the truncation of the higher order moments of the step length distribution (in Eq. 4.18) and is a major influence on the breakdown of diffusion theory.

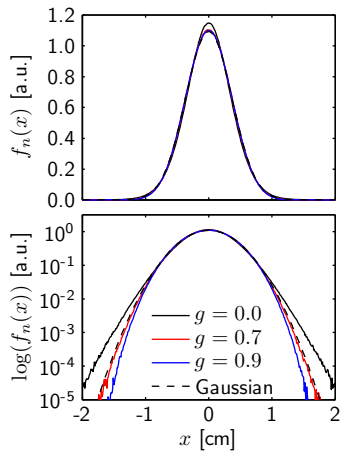

Figure 4.5. *Spatial distributions at 100 ps for $g = 0$, 0.7, and 0.95, calculated using MC. The reduced scattering coefficient was fixed at $\mu_s' = 10$ cm^{-1}. The dashed line shows the Gaussian distribution, i.e. the solution provided by diffusion theory. The variance of all four curves is the same.*

4.4.2 Time domain

The first assumption in the alternative derivation was that the time for a particle to complete a step is $\langle \Delta t \rangle = \langle s/v \rangle$. This can be seen as a discretization of time, where the time a particle has propagated is proportional to the number of steps

$$t_n = n\langle \Delta t \rangle. \tag{4.41}$$

This means that, in diffusion, time is discretized rather than continuous as in RTT. In the continuous time-domain, the time each step takes, Δt_i, depends on the particle velocity, v, and the length of each step, s_i (exponentially distributed)

$$\Delta t_i = \frac{s_i}{v}. \tag{4.42}$$

The time a particle has propagated after n steps is actually

$$t = \sum_{i=1}^{n} \Delta t_i = \frac{1}{v} \sum_{i=1}^{n} s_i. \tag{4.43}$$

The treatment of random walks with continuous, instead of discretized time, has been done by Weiss and co-workers [138, 139]. This so called continuous-time random walk (CTRW), treats random walk on a lattice with either constant transport velocity (step lengths and time is coupled using Eq. 4.42) or random waiting times (time and step lengths are decoupled).

In the limit of many steps, Eq. 4.41 and 4.43 converge. The intermediate regime, where n is not large, can be explored using the Erlang distribution [140]. This distribution describes the sum of n identically distributed exponential random variables, and may be used to transform the discretized time of diffusion to continuous time. The transformation is approximate as the step lengths already have been decoupled from the actual time. The PDF of the Erlang distribution is

$$f_n(t) = \frac{t^{n-1} e^{-t/\mu_1}}{\mu_1^n (n-1)!}, \tag{4.44}$$

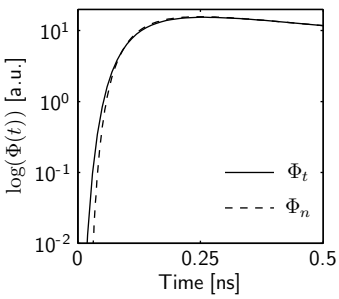

Figure 4.6. *The fluence predicted by diffusion theory in discretized time, Φ_n, and in continuous time, Φ_t. Here, $r = 10$ mm, $g = 0.0$, $\mu_s' = 10$ cm^{-1}, $\mu_a = 0$, and $n_{\text{eff}} = 1.5$. A small difference is observed for early times.*

where, t is the time, n is the number of steps, and $\mu_1 = \langle s_i \rangle / v = 1/(\mu_s v)$ is the mean of the exponential distribution. The fluence in continuous time, $\Phi_t(r,t)$ is the sum of the fluence after a certain number of steps, $\Phi_n(r,n) = \Phi\left(r, n\langle \Delta t \rangle\right)$ (where $\Phi(r,t)$ comes from Eq. 4.10), multiplied by the Erlang distribution, summed over all n

$$\Phi_t(r,t) = \sum_{n=1}^{\infty} \Phi_n(r,n) f_n(t). \tag{4.45}$$

Fig. 4.6 illustrates $\Phi_t(t)$ and $\Phi_n(t)$ for $g = 0$ showing a small discrepancy for early times. For larger values of g, the difference disappears. As in the previous section, it is clear that diffusion favours many smaller steps. The discrepancy between the discrete (number-of-steps) and continuous time domain is, in this context, small and is thus a minor contributor to the breakdown of diffusion theory.

4.4.3 Absorption

In the literature on diffusion theory for light transport, it is stated that $\mu_a \ll \mu_s'$ is required for diffusion theory to hold. The statement may be traced back to the field of neutron transport, where it is explained that the single-scattering albedo, $a = \mu_s/(\mu_a + \mu_s)$, must be close to unity for the P1 approximation to hold [57]. However, as shown in the previous sections, diffusion theory will fail when the number of steps is small, even in the absence of absorption. Absorption is added to the diffusion theory solution, Eq. 4.25, by multiplication with Beer-Lamberts law, Eq. 2.27. It is clear that longer paths are penalized as the absorption is increased, as illustrated in Fig. 4.7. Increasing the absorption will cause particles that have taken shorter paths, *i.e.* taken fewer steps, to dominate the solutions, causing diffusion theory to break down. It is clear that $\mu_a \ll \mu_s'$ still holds as a condition for the validity of diffusion, but the fundamental condition is that n must be large.

4.4.4 The diffusion coefficient

The question regarding whether or not the diffusion coefficient depends on the absorption coefficient [85, 86, 127–130], may be answered using the derivation of the diffusion coefficient in Section 4.3.1. The diffusion coefficient describe how the variance of the spatial distribution (Eq. 4.22) grows in time. The variance of the distribution after n number of steps can be calculated exactly using Eq. A.19. In the limit $n \to \infty$ the discrete and continuous time domains are equivalent, as previously discussed. Considering the spatial distribution at time t, adding absorption, by multiplying with $\exp(-\mu_a v t)$, does not change the shape of the distribution

as t is the same for all particles, regardless of how far they have travelled from the source. It is clear that the variance of the spatial distribution is independent of absorption.

It should, however, be noted that for fewer number of steps, the discrete and continuous time domains are not equivalent. Here, the spatial distribution after n steps, comprise particles that have propagated different lengths. The ones farther away from the source are likely to have taken longer steps and should thus be penalized to a greater extent by absorption. Thus, adding absorption changes the shape of the spatial distribution.

4.4.5 Similarity relation

Regardless of method of deriving the DE it is found that the diffusion coefficient only depend on the reduced scattering coefficient, $\mu_s' = \mu_s(1-g)$. This means that, in the diffusion approximation, μ_s and g are inseparable and the behaviour of the model is fully determined by μ_s'. This relationship is called the *similarity relation* [141].

Pifferi *et al.* briefly investigated the similarity relation in the time domain using MC simulations, concluding that the difference in curve shapes was small as long as $0.7 < g < 0.9$ [99]. Kienle and Patterson came to a similar conclusion, stating that the difference in curve shapes was small as long as $g > 0.8$ [101]. Studying steady-state reflectance at small source-detector separations, Mourant *et al.* noted that different phase scattering functions gave different results despite exhibiting the same g-factor [142]. Similar results were also reached other authors, *e.g.* [143, 144].

The result above are easily interpreted in terms of moments of the spatial distribution. The variance (second moment) of the spatial distribution depend only on the first order moment of the scattering phase function, *i.e.* g. This is the origin of the similarity relation. However, when entering a region where diffusion theory breaks down, the spatial distribution does depend on the higher order moments. For larger g-factors, diffusion breaks down "later", explaining the observed applicability limits of the similarity relation. How the breakdown manifests itself depend on the higher order moments of the spatial distribution, which in turn depend on the higher order moments of the scattering phase function. For example, in the calculation of the excess kurtosis (Eq. 4.38) the second and third moments of the Henyey-Greenstein distribution was used.

Making the connection back to Section 2.2.4, it is now clear why the Henyey-Greenstein scattering phase function can be successfully applied to problems of light propagation in complex biological tissue. For macroscopic problems, only the first moment of the scattering phase function, g, will significantly influence the

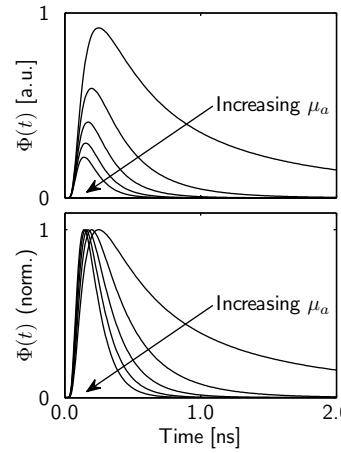

Figure 4.7. *The fluence rate for different levels of absorption, μ_a = 0.0, 0.1, 0.2, 0.3, and 0.4 cm^{-1}. Other parameters: r = 1.0 cm, μ_s' = 10 cm^{-1}, n_{eff} = 1.5. When increasing the absorption, the resulting TOF distribution is increasingly dominated by earlier particles.*

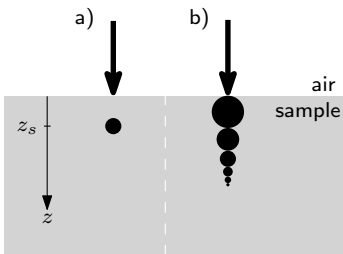

Figure 4.8. **a)** *single or* **b)** *multiple source representation of a directed source incident on a boundary. In* **b)** *the strengths of the sources decay exponentially with the depth.*

results and, according to the similarity relation, in many cases g is not even relevant.

The similarity relation was used in the MC-based evaluation scheme in Paper **I**. Clearly being used in a region where diffusion theory is known to break down, the application of the similarity relation was still successfully. A possible explanation for this is that a reasonable guess for g was used in the MC simulations. In a small range of g as suggested above, the excess kurtosis is similar, *i.e.* the deviation from a Gaussian is similar.

4.4.6 Conclusions from the alternative derivation

In the analysis of the approximations in diffusion theory, it may be concluded that the fundamental requirement for diffusion theory is that the number of step must be large, or equivalently that only late times can be considered. Absorption attenuates late light and must thus be small. The fluence close to the source is dominated by early light and it is therefore preferable to consider light far away from the source in order to be able to use diffusion theory.

At very late times, the distribution of light is independent of all the moments of the step length distribution and hence the scattering phase function. Here, it is clear that the diffusion coefficient is independent of the absorption. At intermediate times, the first moment, g, comes into play and diffusion theory starts to break down. Diffusion favours larger values of g and the breakdown occurs more easily for isotropic scattering. Finally, at earlier times, even higher order moments of the scattering phase function matters and the Henyey-Greenstein function may no longer be used without further analysis.

4.5 Solving the diffusion equation

This section deals with solutions to the diffusion equation in various geometries. An excellent overview of different geometries and boundary conditions is given by Moulton [145].

4.5.1 Source representation

In the derivation of the DE, it was assumed that the source was isotropic i.e. radiating equally in all directions. In actual measurements this is rarely the case. Consider for example a collimated beam of light incident on a scattering medium or light being delivered to the medium using an optical fibre. In both cases the incident light has an initial direction. The most common way of handling this problem is by approximating the directed source by an isotropic point source at a distance $z_s = 1/\mu_s'$ from the actual source, in the direction of the source [146, 147], see Fig. 4.8 a). This is motivated by z_s being the mean of the exponential

distribution of the first (isotropic equivalent) scattering events. The approximation works well far away from the source but close to the source the approximation is crude. A better approximation of the source is to model the directed source as a distribution of isotropic sources with strengths proportional to $\exp(-z\mu_s')$, where z is the distance from the source [148], see Fig. 4.8 b). A third approach is given by Xu *et al.* [149] who considers the cumulants of the spatial distribution in the direction of the source. Since the source has an initial direction the distribution is no longer symmetric and the odd order moments will no longer vanish.

Throughout the rest of the section only the first of the above source representations (isotropic) will be used.

4.5.2 Infinite medium

The solution to the DE in a macroscopically homogeneous ($D(\mathbf{r}) = D$), infinite medium with an isotropic point source has already been given in Eq. 4.10 and Eq. 4.25. Including absorption the solution is

$$\Phi(r,t) = vE_0(4\pi Dt)^{-3/2}\exp\left(\frac{-r^2}{4Dt} - \mu_a vt\right). \tag{4.46}$$

Considering the stationary case the solution is[8]

$$\int_0^\infty \Phi(r,t)dt = E_0\frac{3\mu_s'}{4\pi r}\exp(-\mu_{\text{eff}}r), \tag{4.47}$$

where $\mu_{\text{eff}} = \sqrt{3\mu_s'\mu_a}$ [m^{-1}] is the effective attenuation coefficient.

In Paper **I**, Eq. 4.46 is compared to the WMC model and the validity of time-domain diffusion theory in infinite geometries is investigated.

4.5.3 Semi-infinite medium

Light propagation in half-space geometries introduces the problem of appropriately handling boundaries between different media, for example, between a scattering media and air. At the boundary light is reflected back into the scattering medium due to the mismatch in refractive index, as described for a smooth boundary and unpolarized light by Eq. 3.8. Numerous papers on how to treat

[8] As pointed out by *e.g.* Pierrat *et al.* [130], the appropriate way to find the steady-state solutions to the diffusion equation is rather to state the steady-state diffusion equation and solving it instead of integrating the time-domain results. However, the difference between the two methods is, in the context of this thesis, negligible.

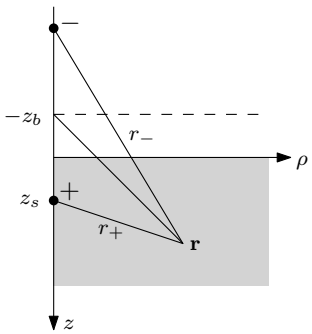

Figure 4.9. *Illustration of the positions of the positive and negative source in the extrapolated boundary condition.*

boundary conditions in the diffusion approximation have been published over the years [145, 146, 150–152], many of them sharing the method of using series of positive and negative sources to account for the losses introduced by the boundary. These sources are equivalent to the solution to DE in infinite media. Here, the extrapolated boundary condition [84, 90, 153] (EBC) is considered. In the EBC, a positive source is introduced at a distance z_s into the scattering medium, as described in Section 4.5.1. A negative source is introduced outside the medium to create a virtual boundary with zero fluence at a distance $-z_b$ from the actual boundary, see Fig. 4.9. The location of the virtual boundary is set so that the flux through the boundary, integrated over all angles, approximates the boundary condition [122, 146, 153]. In time-domain the solution becomes

$$\Phi(\mathbf{r},t) = \frac{cE_0 \exp(-\mu_a ct)}{(4\pi Dt)^{3/2}} \left[\exp\left(\frac{-r_+^2}{4Dt}\right) - \exp\left(\frac{-r_-^2}{4Dt}\right) \right], \quad (4.48)$$

where

$$r_+ = \sqrt{\rho^2 + (z - z_s)^2}, \quad (4.49)$$

$$r_- = \sqrt{\rho^2 + (z + z_s + 2z_b)^2}. \quad (4.50)$$

Considering the *diffuse reflectance i.e.* light that exit the medium after one or more scattering events, a commonly measured quantity, it is appropriate to consider the flux through the boundary, $R(\rho,t) = -D\nabla\Phi(\mathbf{r},t)\cdot(-\hat{z})\|_{z=0}$ [145] or weighted combinations of the flux and the fluence [122, 153].

The methods of handing boundaries and represent sources are approximate and may introduce restrictions on the applicability of diffusion theory. In Paper **VI** the accuracy of diffusion model of time resolved diffuse reflectance was investigated. The diffusion model, using the EBC boundary condition, was found inaccurate in many cases when compared to the WMC model. However, diffusion did not perform significantly worse than in infinite media, as investigated in Paper **I**.

4.5.4 Other geometries

The concept of mirroring sources may be extended to accommodate several boundaries, for example a slab geometry which requires an infinite series of positive and negative sources [84, 146]. Analytical solutions for other geometries, such as cylinders and spheres also exist [145] and when it comes to more difficult geometries, or for inhomogeneous optical properties, numerical methods such as the finite element method may be applied [154, 155].

4.6 Anisotropic diffusion

Anisotropic diffusion, not to be confused with anisotropic scattering, is observed when the diffusion coefficient is dependent on the direction. In a macroscopic picture, it means that light will propagate at different rates in different directions.

In order to understand why anisotropic diffusion occurs, consider, for example, the scattering of light by an asymmetric particle, such as a prolate spheroid. Depending on the size and properties of the particle, the differential scattering cross section may depend on the orientation of the particle relative to the incident plane wave. This means that the scattering cross section and the phase scattering function may be direction-dependent. Fig. 4.10 a) illustrates a collection of randomly oriented such particles. Despite the assumed direction dependency of the scattering by individual particles, the random orientation of the particles ensures that the resulting wave transport is isotropic. However, when the particles are statistically aligned, as illustrated in b), the lack of randomness causes the wave transport to become anisotropic.

Anisotropic diffusion can be observed in many materials such as aligned nematic liquid crystals [157–159], porous semiconductors [160], stretched plastics [161, 162], and wood [163–165]. Due to the anisotropic microstructure of many kinds of biological tissues, anisotropic light transport can be observed there as well, for example, muscle [166], bone [167], teeth [168], skin [169], and arterial walls [170].

In Paper **VIII**, anisotropic diffusion of light was observed in compacted granular porous media. Due to the radial symmetry of the samples, the anisotropy cannot be observed in steady state reflectance or transmission measurements. Instead, spatially resolved time-domain measurements were made, revealing the anisotropic transport behaviour.

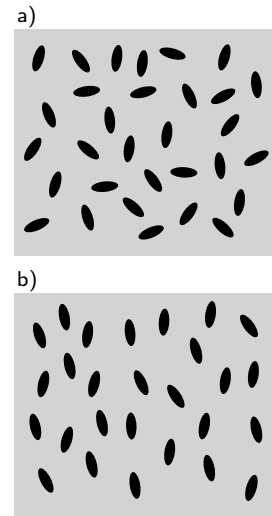

Figure 4.10. *Example of materials with isotropic and anisotropic transport properties. In a) the scattering particles are randomly oriented, resulting in a macroscopic isotropic behaviour. In b) the particles exhibit statistical alignment, resulting in anisotropic transport of waves, i.e., anisotropic diffusion. Modified from Bret [156].*

4.6.1 Anisotropic transport modelling

A solution to the anisotropic diffusion problem was stated in Eq. 4.23 and 4.24. A time-domain anisotropic diffusion equation, resulting in the same solution, was given in [159].

Anisotropic radiative transport may also be modelled using, for example, Monte Carlo methods [171]. The simulation is straightforward, but requires $p(\hat{\mathbf{s}}', \hat{\mathbf{s}})$ and $\mu_s(\hat{\mathbf{s}})$ to be explicitly defined. In addition, the relationship between these two parameters and the diffusion coefficients is not trivial [162, 172]. In this context, the random-walk based derivation of the diffusion coefficient in Section 4.3.1, provides an intuitive picture of the link between $p(\hat{\mathbf{s}}', \hat{\mathbf{s}})$ and $\mu_s(\hat{\mathbf{s}})$, and the diffusion coefficients.

Chapter 5

Time-of-flight spectroscopy

Absorption spectroscopy is a versatile and widely employed tool to investigate constituents of samples. In conventional optical absorption spectroscopy, a transmission spectrum, *i.e.* the wavelength dependent transmission coefficient, is measured and compared to known spectra of different molecules. This allows identification of the molecules present in the sample. Further, if the path length through the sample is known, the concentration of the identified molecules may be calculated, as suggested by Eq. 2.27 and 2.26. In the absence of scattering, for example, in a glass of water or wine, measuring the path length experienced by the wave of light is trivial, as light passes straight through.

In contrast to clear media, the presence of scatterers complicates the approach of absorption spectroscopy as the path length no longer is well defined. This is easily understood in the context of Monte Carlo simulations of the RTE, where light propagation through a turbid sample can be seen as a random walk of fictional energy particles. As illustrated in Fig. 5.1, considering transmission through a turbid slab, some particles will take a short path while some will make a longer excursion, resulting in a temporal broadening of the transmitted pulse. In time-of-flight spectroscopy (TOFS) the time evolution of a pulse transmitted through a turbid medium is recorded. Evaluation of the data, for example, by comparing it to a physical model of light transport such as Monte Carlo or diffusion theory, allows separation of the scattering and absorption properties of the sample. Once separated from the scattering properties, the absorption information may, just as in the simpler case, be used to identify and quantify the absorbers present in the sample. In addition, the scattering properties, often merely considered an aggravating factor, contains information on the microstructure of the sample.

In this chapter, some aspects of the TOFS technique will be explained, such as instrumentation, advantages and applications.

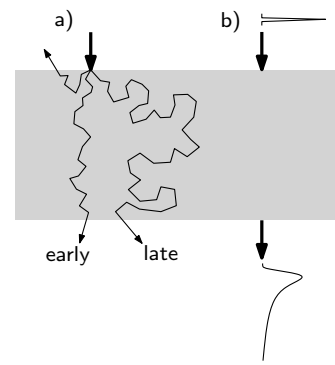

Figure 5.1. *Illustration of the temporal broadening of pulses propagating in turbid media. In the random walk picture, particles experience paths of different lengths as they are scattered multiple times. The distribution of different paths cause the transmitted pulse to be broadened in time. Modified from [125].*

5.1 Introduction

TOFS has its origins in the field of atmospheric optics where time-resolved propagation of light in clouds was investigated in the early 1970's [173, 174]. Investigating more strongly scattering and significantly smaller samples, Shimizu *et al.* presented their experimental results of measurements of densely packed latex spheres in 1979 [175]. While these results enabled measurements of materials such as tissue, the breakthrough for TOFS in biomedical applications came in the late 1980's when Chance and coworkers presented application of TOFS to measure hemoglobin and myoglobin in tissue [176, 177].

5.2 Instrumentation

The enabling technology for the experiment of Shimizu *et al.* was the advent of fast pulsed lasers, able to generate pulses with duration of picoseconds (10^{-12} s) or less [175]. In the biomedical and pharmaceutical applications considered here, the time-scale of the broadening of the pulses is in the range of hundreds of picoseconds to a few nanoseconds. To accurately measure the temporal shape of the pulse, both the source and the detection system must work on a time-scale much shorter than this. Over the years, the instruments involved in TOFS have been significantly improved and simplified, allowing faster, more accurate, and less expensive measurement systems with significantly expanded capabilities. In this section, a few relevant detection systems and sources are briefly mentioned.

5.2.1 Detection system

In Papers **I**, **VI**, **IV**,**V**, and **VII** a detection scheme called time-correlated single photon counting (TCSPC) was used. The subject of TSCPS is thoroughly covered in the book by Becker [178]. Briefly, TCSPC, as the name implies, is based on the detection of individual photons. The time of arrival of the photons, compared to a reference pulse, are measured electronically and a histogram of arrival times is built up by sequential measurements of many photons. The method is statistical, in the same sense Monte Carlo simulations are statistical, and is subject to the same drawbacks; the recorded TOF curves are noisy, and, due to limitations in detectors and counting electronics, the acquisition time is typically long (several seconds for a single measurement). An advantage of the TCSPC technique is that it allows measurements even when the signal to be measured is very weak. Also, it allows large dynamic range measurements, limited by the detector, or ultimately, the statistical noise.

The detectors for TCSPC must be sensitive enough to detect single photons, yet be fast enough for accurate timing of the detection. Due to clever electronics in the TCSPC system (a unit called a constant fraction discriminator) the timing accuracy may be a few picoseconds, despite the temporal response of typical detectors being several nanoseconds long. In Papers **I**, **VI**, **IV**, **V**, **VII**, and **VIII** micro channel plate-photomultiplier tube (MCP-PMT) detectors were used. In particular, in Paper **V** a system based on TCSPC and dual MCP-PMTs was described, extending the usable spectral range of TOFS up to 1400 nm, thus covering a range important for vibrational spectroscopy of solid samples [179].

In the last few years, single photon avalanche photodiode (SPAD) detectors have emerged as a competitive alternative to PMT detectors [178, 180–182]. Modern SPAD's may feature virtually zero dark noise and allow higher count rates, and thus shorter acquisition times, but offer a much smaller detection area limiting the use in some cases, *e.g.* fibre based TOFS systems. Further, SPAD's may be combined with fast electronically controlled gating of the bias voltage, enabling measurement with very large dynamic range [182]. Such time-gating techniques have recently been used to realize TOFS at small source-detector separations [183] and were used in Paper **IX** to demonstrate the possibilities to do TOFS with a single fibre, used to both deliver and collect light from the sample. SPAD detectors based on InGaAs instead of Silicon, are currently under development [184], possibly extending the advantage of SPAD detectors to the spectroscopically important region above 1000 nm.

While TCSPC-based systems are limited to measuring one or a few wavelengths at a time, alternative techniques exist simultaneously measure TOF distributions for several wavelengths simultaneously. Streak-cameras is an example of such a technique and its use in TOFS was the topic of the thesis by Abrahamsson [185]. Other notable detection techniques rely on electronic [186] (used *e.g.* for time resolved imaging) or optical [159, 175, 187, 188] time gating. Using the latter, remarkable temporal resolution, $\sim$ 10 fs, may be achieved [188, 189].

5.2.2 Sources

In Papers **I**, **VI**, and **IV** a TOFS system based on pulsed narrow-bandwidth diode lasers was utilized. Using a limited number of carefully selected fixed wavelength sources allows for some basic spectroscopy but access to the entire spectrum is clearly desirable, a problem approached by several authors [190–194]. Today, ps-pulsed supercontinuum sources are commercially available. Such a system was used, in combination with two acousto-optical tunable filters (AOTFs), in Paper **V**, to allow spectral filtering in the entire

$\sim 600 - 1550$ nm range.

The aspect of spectral filtering was investigated by Farina *et al.* showing that the bandwidth of the filtered pulses must be accounted for when employing broadband TOFS systems [195].

5.3 Relationship to other techniques

In order to understand the advantages of the TOFS method for assessment of optical properties, it is helpful to consider its relation to other techniques for diffuse optical spectroscopy. Here, a few such techniques are considered.

5.3.1 Spatially resolved steady-state

Spatially resolved steady-state is a technique where the fluence or flux is measured at several distances from the source, enabling deduction of the optical properties of the sample by comparison to a light propagation model [147, 148, 196, 197]. Despite limitations, the technique is widely popular due to its simplicity and low cost.

Considering light propagating in an unbounded, homogeneously scattering and absorbing material, far away from the source. In the diffusion approximation, the fluence distribution in steady state (*i.e.* a continuous source) is given by Eq. 4.47 while the spatial and temporal distribution is given by Eq. 4.46. In steady state, the shape of the spatial distribution is given by $r^{-1}\exp(-\mu_{\text{eff}}r)$. The absolute fluence level is proportional to μ_s'. As μ_{eff} depend on both the absorption and scattering coefficients, the two coefficients may not be separated by the shape of the spatial distribution alone. In order to separate absorption and scattering, it is required to measure the absolute fluence level (relative to the source), a cumbersome experimental task [198], or to measure fluence rate at a distance close to the source where diffusion is known to break down.

In the time-domain, at a fixed r, it is evident that the effect on temporal shape by the diffusion coefficient and absorption coefficient are different. While the absolute fluence level also carry information related to the scattering, the temporal shape of the transmitted pulse carries all the information needed to assess both the diffusion and absorption coefficient. In conclusion, by making measurements in the time-domain, both the scattering and absorption properties of a material may be deduced from a single measurement without the need to measure absolute light intensities. The shape dependency on scattering and absorption is illustrated in Fig. 5.2.

Moving away from model-based data evaluation, it is also possible to deduce optical or physical properties of a sample using

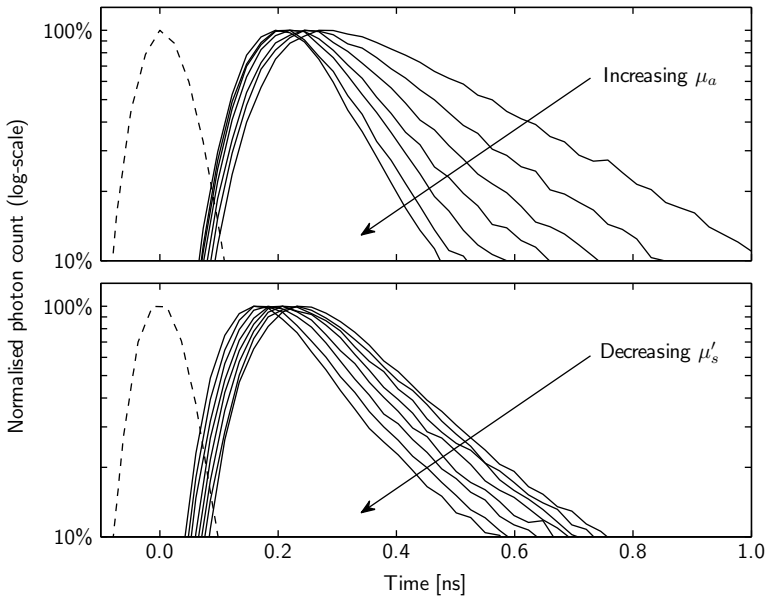

Figure 5.2. *An illustration of how absorption and scattering changes the shape of the TOF-curves, measured experimentally of tissue simulating phantoms (see Section 5.5.3) In the upper figure, absorption was increased in small steps by adding ink. The effect on the added absorption is an increased decay rate, as predicted by Beer-Lamberts law, Eq. 2.27. In the lower figure, increasing the scattering causes the detected pulses to arrive later and to be broadened. The dashed lines indicate the instrument response function (IRF) of the system. Modified from [125].*

calibrations. This requires measurements on a large set of samples with varying, but known, properties. A measurement of an unknown sample may later be compared to the database of measurements on known samples, and the properties of the unknown sample may thus be estimated. Such calibration-based techniques, combined with steady state measurements, are common, for example, in so-called near-infra red spectroscopy (NIRS) of pharmaceutical samples [179]. A disadvantage of this approach is the undefined behaviour when measurements are made on samples that lie outside of the range covered by the calibration database. The technique is thus sensitive to changes in, for example, the scattering properties of the sample, caused by small changes in the microstructure.

In conclusion, the TOFS technique, albeit slow, and relatively expensive and complex, allows straightforward separation of the effects of scattering and absorption in a sample from a single measurement. The TOFS technique uses models of light propagation,

rather than calibrations, for data evaluation and is thus capable of handling virtually any combination of optical properties.

A notable difference between the steady-state and time-domain measurements is the difference in the properties measured. TOFS gives a measure of the *dynamic* properties of light transport while steady-state measurements probe the *static* properties. The (reduced) scattering coefficient is a static property, governing step lengths while the diffusion coefficient is a dynamic property, also taking the energy transport velocity into account. The energy transport velocity is generally assumed the be the same as the phase velocity[1], $v = v_p = c/n_{\text{eff}}$. This allows μ_s' to be derived from TOFS measurements by assuming an effective refractive index of the material. This assumption was made in Papers **I**, **IV**, **V**, **VI**, **VII**, and **IX**. Alternatively, time-domain and steady-state techniques may be used together to gain knowledge of the energy transport velocity [199, 200].

5.3.2 Scatter correction

In scatter correction techniques, a spectrum, obtained from a steady-state measurement, is corrected for the contribution due to scattering. This correction is often model-based and relies on the smooth and predictable spectrum of the scattering process, $\mu_s' \propto \lambda^{-b}$, as discussed in Section 2.2.4. Using this *a priori* information, the entire scattering spectrum can be estimated if the (reduced) scattering coefficient is know for a few discrete wavelengths. Hence, combining broadband steady state techniques with discrete wavelength systems *e.g.* TOFS, yields a powerful combination. This kind of scattering correction has been explored by several authors, for example in studies of pharmaceutical preparations by Abrahamsson *et al.* [201] and in clinical studies of breast tumour detection [202–204].

Another way of doing scatter correction is to leave the parameters of the scattering spectrum as free parameters in a data evaluation fitting procedure, see *e.g.* [205].

5.3.3 Frequency-domain

In the frequency-domain (FD) technique, an intensity modulated source is used. At the detector, the change in amplitude (demodulation) and phase shift, compared to the source function is measured [204, 206, 207]. Doing this measurement for all modulation frequencies, the frequency domain technique would be equivalent

[1] In general this assumption holds. However, in certain materials, for example, where the scatterers are well defined in size and shape, the resonant behaviour of the scattering is no longer averaged out, resulting in a behaviour where the energy transport velocity differs from the phase velocity [199].

to the time-domain technique. The results of the two techniques, TOF curves, and phase and demodulation frequency spectra, are related by the Fourier transform. In order to extract optical properties, and separate absorption and scattering, all frequencies are not needed. In fact, a measurement at a single frequency carries enough information to extract μ_a and D (or μ_s') but, in general, increasing the number of frequencies and including higher frequencies increases the accuracy [121].

Advantages of the FD technique, in discrete wavelength measurements, is relaxed requirements for the optical and electrical system, allowing simpler and cheaper systems [208]. Furthermore, if just a few frequencies are needed, the measurement time may be significantly reduced. Compared to TOFS, some of the drawbacks of FD are the lack of higher frequency information and the requirement for more light to reach the detector. Time domain measurements are thus preferable for fundamental studies of light propagation while frequency domain systems are more suitable, for example, in large scale clinical trials [202].

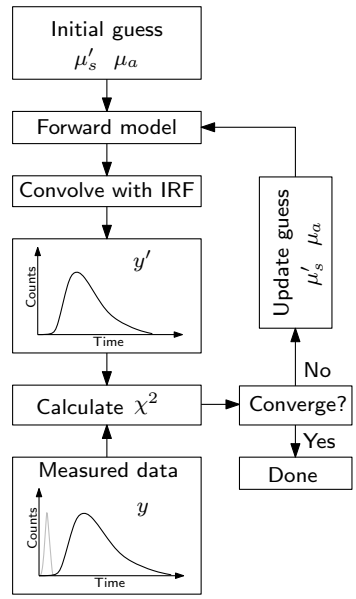

Figure 5.3. *A simplified flowchart of the iterative fitting procedure.*

5.4 Data evaluation

In order to assess optical properties from TOFS measurements, data evaluation is required. This, so called inverse problem, is a non-trivial but crucial step in the process of TOFS measurements and deserves attention. Some aspects of TOFS data evaluation were thoroughly discussed in the thesis of Svensson [125].

In the previous chapters, the forward model of light transport in turbid media was discussed. Radiative transport theory was introduced as a physical model of the reality, where the complex medium was reduced to three parameters *i.e.* μ_s, $p(\hat{\mathbf{s}}', \hat{\mathbf{s}})$, and μ_a. This model was solved using Monte Carlo or diffusion theory, where the temporal response of a sample may be calculated, given a set of the three parameters and a specific geometry. Together, this constitutes the forward model. However, in the inverse problem, a temporal response (a TOF curve) is given and the optical parameters corresponding to that curve are sought. As the forward model depends on the optical properties in a complex (non-linear) way, the problem may not be solved using ordinary regression analysis. Instead, methods such as iterative minimization of the sum-of-squares must be used to solve the inverse problem. The problem turns into the minimization of the function

$$\chi^2(\mu_s', \mu_a) = \sum_{i=1}^{N} \left(\frac{y_i - y(\mu_s', \mu_a, t_i)}{\sigma_i} \right)^2, \qquad (5.1)$$

where y_i is the experimental data, t_i the corresponding time, and σ_i are weights of the data points. The function $y(\mu_s', \mu_a, t_i)$ is the

forward model, convolved with the instrument response function (IRF). The IRF is an important aspect of TOFS, as it accounts for the temporal broadening of the system itself, caused by finite temporal length of the laser pulses, the temporal response of the detctors, electronic timing jitter, etc. The IRF also serves the important role of a timing reference for the recorded TOFS curves.

Fig. 5.3 illustrates a simplified flowchart of the iterative fitting procedure. The difficulty lies in intelligently updating the fitting parameters each iteration. A popular and commonly used method for solving this minimization problem is the Levenberg-Marquardt method [209].

The iterative nature of the data evaluation implies that the forward model will have to be evaluated for several sets of optical properties before the optimal fit is found. This introduces a constraint on the models used in evaluation; the evaluation time of the model must be short in order for the data evaluation to finish in reasonable time. In any case, the model used must be appropriate. As discussed in Chapter 4, under conditions relevant to tissue measurements, diffusion models break down, in particular in presence of strong absorption. Diffusion models should, despite their attractive analytical form, be avoided in evaluation of measurements where there is a risk of diffusion breakdown. The issues of model accuracy and evaluation speed were addressed in Papers **I** and **VI**, introducing a fully scalable MC model used to evaluate TOFS data. It was shown that improved modelling, *e.g.* Monte Carlo, is required in many situations of measurements of tissue, in order to accurately measure optical properties. In cases where WMC rescaling is not possible, Paper **II** provides a major step towards enabling MC-based data evaluation in arbitrary geometries, by significantly reducing the simulation time in MC.

Other evaluation methods, besides iterative fitting also exist [210, 211]. In particular, in the early days of TOFS a popular method of data evaluation was to extract μ_a from the slope of the late part of the TOFS curve [176, 177, 212, 213], assumed independent of the scattering coefficient at late times (compare to Fig. 5.2). While theoretically possible, this method is hard to use in practice as it requires very large dynamic range in order to collect data at sufficiently late times. The method is related to the ideas presented in Paper **IX**, where this the eight orders of dynamic range provided by the SPAD-based detection scheme, clearly resolves this late part. Still, iterative fitting proved to be a far superior evaluation scheme as it allows data from earlier times to be used as well.

5.5 Estimating physical properties

In the previous sections, aspects on TOFS instrumentation and TOFS data evaluation, were discussed, *i.e.* how TOFS curves are measured and how the optical properties, μ_s' and μ_a, may be assessed. Much effort is spent assuring accurate evaluation of these properties. The properties in themselves are of interest, for example, in fundamental studies of light propagation as well as for solving the forward problem in various applications. However, from a spectroscopic point of view, the optical properties are valuable as they can be used to assess the physical properties of a measured sample, such as chemical composition.

5.5.1 Absorption spectroscopy

Absorption spectroscopy relies on an accurately measured absorption spectrum, $\mu_a(\lambda)$. The total absorption spectrum is the sum of the absorption spectra of the different absorbers, weighted by their concentrations, as described by Eq. 2.28. Knowing the spectra of the absorbers (chromophores) present in the sample, this equation turns into a linear system of equations. The quantities of the absorbers may be calculated by solving the system of equation. For the system to be determined, at least as many measurements of μ_a, at different wavelengths, as there are major absorbers, are required. Therefore, in applications of absorption spectroscopy of tissue, for example, studying the oxygenation of blood only a few wavelengths needs to be measured (see Fig 2.5). In Paper **IV**, a four wavelength TOFS system was used to measure the oxy- and deoxyhemoglobin concentration in human prostate *in vivo*.

In order to improve the accuracy in the absorption spectroscopy, it is preferable to work with an overdetermined system, *i.e.* measuring the full spectrum. In Paper **V** a so-called white light system was introduced, capable of measuring the absorption coefficient in the entire $650 - 1400$ nm range. The system is intended for applications involving pharmaceutical samples where the important spectral information (absorption peaks) is located in the NIR range (> 1000 nm).

An interesting twist on absorption spectroscopy, called double-differential spectroscopy, was introduced to the field of tissue spectroscopy, by Kukreti *et al.* [214]. There, the measured absorption spectrum was compared to that of presumed healthy tissue from the same patient, revealing small, but significant, differences with potential use as optical biomarkers for tumours.

5.5.2 Assessing structural properties

At a first glance it appears as if the presence of scattering in a sample is just an aggravation in the application of absorption

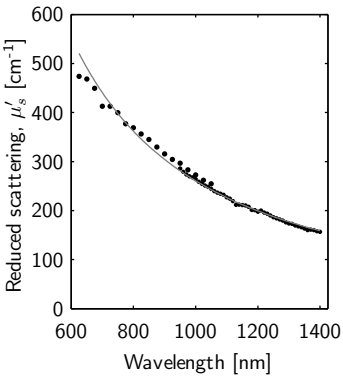

Figure 5.4. *A scattering spectrum of a tablet made of epoxy and TiO_2, measured using the dual-PMT system described in Paper* **V**. *The solid line illustrates the scattering power law fit: $\mu_s' = 261 * (\lambda/\mu m)^{-1.47}$. Adapted from Paper* **V**.

spectroscopy. However, as discussed in Section 2.2, the scattering properties are intimately linked to the microstructure of the scattering material, as microscopic variations in the refractive index are the source of scattering. Clearly, in the process of reducing the complex microstructure of *e.g.* tissue, to one or a few parameters, a lot of information is lost. In biological tissue, the source of the microscopic variations in refractive index, are cells and organelles. The scattering spectrum hence carries information about the structures that contributes the most to the refractive index variations, for example, cell nuclei and mitochondria [215, 216], and collagen [11]. A scattering spectrum of a tablet phantom is shown in Fig. 5.4. Just as in the case of tissue, the microstructure is complex and cannot be considered a collection if independently scattering particles. Still, the scattering exhibit a power law behaviour.

In colloidal suspensions of scattering particles, the analysis of structural information is straightforward. In case of spherical scatterers, Mie theory may be used to infer the size and concentration of the scatterers from the scattering spectrum [38, 217].

The study of anisotropic transport properties is another, not strictly spectroscopic, way of revealing sample microstructural parameters [162].

Turning to fundamental investigations of the interaction of electromagnetic waves and strongly scattering materials, the mean free path, energy transport velocity and effective refractive index are properties of great interest [200, 218].

5.5.3 Phantoms

In order to evaluate, improve, and compare instruments, as well as theoretical models, access to objects with known and/or controllable optical properties is essential. A review of such objects, called "phantoms", was recently published [219]. Below, two commonly used phantom designs are briefly discussed as they were extensively use in the work in this thesis.

Perhaps the most common phantom design in the field of biomedical optics is the liquid phantom, based on water and Intralipid [220, 221], and an absorber. Intralipid is the name of a commercially available lipid emulsion, *i.e.* lipid microparticles in water, much like common milk. The scattering properties of an Intralipid based phantom may be calculated approximately [220], or calculated using a batch specific calibration [222]. To incorporate absorption, for example blood [223] or ink [224] may be added. These liquid phantoms have the advantage that the scattering and absorption may be modified at any time, by adding more Intralipid or absorber by diluting the phantom. This was used to perform added absorber and added scatterer series in Papers **I** and **IX**. Measurement from such series are shown in Fig. 5.2.

A second kind of phantom is the solid phantom, based on an epoxy resin as bulk material, with titanium dioxide particles added for scattering and toner ink added as absorber [225]. The finished phantoms are durable and stable, but their optical properties may not be changed. Such phantoms were created in the MEDPHOT initiative, aiming to investigate the performance of diffuse optical spectroscopy instruments in an international collaboration [104]. In Paper **VI** this set of phantoms was characterized using TOFS in combination with WMC data evaluation, demonstrating the necessity of improved modelling in TOFS data evaluation.

5.6 Applications of TOFS

The spectroscopic applications of TOFS are intimately linked to those of diffuse optical spectroscopy (DOS) in general, which are to numerous to count. Due to the amount of information provided by TOFS (the full time of flight histogram), the technique is primarily used in more fundamental, or piloting, studies of DOS or fundamental studies of light propagation. In *e.g.* medical applications, unless all the information provided by TOFS is needed, simpler techniques are generally applied. In this section a few pharmaceutical and biomedical applications are highlighted. In addition to those fields, TOFS has been applied in various other studies, for example, studies of agricultural produce [226, 227], measurements of optical thickness of clouds [228], and spectroscopic studies of wood [163, 229]. Also, TOFS is an essential tool in the fundamental understanding of wave propagation in complex media, for example, in the search for Anderson localization [230, 231].

5.6.1 Pharmaceutical applications

Near-infrared spectroscopy (NIRS) has, over the last decades, evolved into an important tool in the analysis of pharmaceutical preparations [179]. NIRS, commonly based on steady state measurements of the transmission or reflectance spectrum, allows accurate quantitative chemometry, *i.e.* identification and quantification of active pharmaceutical components in tablets. Being an optical technique, the measurements are fast, inexpensive, non-destructive, and requires little or no sample preparation. The complication of scattering is generally handled by calibration, making the method sensitive for changes in the sample microstructure. The microstructure is an important parameter in pharmaceutical manufacturing of durable and robust tablets, and for dissolution dynamics of tablets in the gastro-intestinal system [179].

In order to separate the absorption and scattering properties, measurement techniques that rely on model based data evaluation have recently gained interest. A review of such techniques and their application was recently published [232]. Instruments

for diffuse optical spectroscopy in time-domain [233], frequency-domain [234], and spatially resolved steady state [197] have been explored, all of them relying on isotropic diffusion theory for data evaluation. In Paper **VIII** the use of isotropic models is questioned, as it is shown that light propagation in compacted granular media is anisotropic. In such materials, used in pharmaceutical tablets as filler materials, the anisotropy originates from an anisotropic microscopic pore structure, induced by compaction [235, 236]. While this is a complication in modelling, it also shows that optical methods may provide a valuable and non-destructive way of probing this microstructure. This topic is also explored in Paper **VII** where TOFS was used in combination with the GASMAS technique [43, 237] in an investigation of how light interacts with porous solids. Although revealing the need for better modelling in order to realize accurate model-based optical porosimetry, excellent correlation between optical porosity and actual porosity, measured by a standard, but destructive, reference technique, is shown. On a final note regarding optical measurements of the microstructure of porous samples; as in the case of tissue, these materials are clearly not a collection of independent scatterers. Still, a power-law behaviour of the scattering is observed, with coefficients related to the pore structure [238, 239].

5.6.2 Biomedical applications

Optical mammography

The one medical application of TOFS, and related DOS techniques, that perhaps have received the most attention over the years is so-called optical mammography. Here, optical spectroscopic techniques are employed, either in point measurements or in a tomographic manner, in search of malignancies. [202, 214, 240–244]. In breast tissue, scattering is reasonably weak and the absorption small enough to allow optical penetration depths of a few centimetres. Thus, an entire breast may be probed non-invasively in either transmission or reflection geometries. However, as light scatter in tissue, the spatial resolution in such measurements is coarse, in particular in comparison to conventional X-ray based mammography measurements. Optical techniques, however, offers several advantages; light within the tissue optical window is non-ionizing and, at intensities used in TOFS, completely harmless. Also, optical techniques are spectroscopic, providing several opportunities for contrast. Absorption of blood, water, and lipids all provide contrast [202, 214, 242–244]. The scattering spectrum have also been shown to provide contrast between tissue types, as well as between normal and malignant breast tissue [245–248]. In addition to the potential application of optical mammography, this optical contrast, providing information on tissue composition

and structure, is currently being evaluated as a tool to follow and predict the tissue response in cancer treatment [14].

Interstitial *in vivo* spectroscopy

TOFS have successfully been applied to *in vivo* measurements of the human prostate, proving its value in spectroscopic measurements of blood rich internal organs, see *e.g.* [105] and Paper **IV**. These studies were motivated by the potential application of photodynamic therapy (PDT) treatment of prostate cancer. PDT relies on three things for successful necrosis/apoptosis. i) The presence of molecular oxygen ii) an appropriate light dose, and finally iii) the presence of a photosensitizer, a light activated molecule, converting oxygen into toxic singlet oxygen. Thus, in PDT dosimetry accurate measurements of the tissue oxygenation are beneficial. Also, in order to calculate the light dose, the optical properties of the tissue are also of interest. An overview of interstitial PDT for prostate cancer treatment and PDT dosimetry can be found in [249, 250].

The oxygenation in tumours is not only of interest in PDT. Treatment outcome of other modalities, such as radiotherapy, brachytherapy, and some forms of chemotherapy, is significantly influenced by the amount of oxygen present in the tumour. See, for example the review by Vaupel *et al.* [251].

Motivated by minimally invasive interstitial absorption spectroscopy, a single-fibre TOFS system was demonstrated in Paper **IX**.

Hemodynamics and functional measurements

In addition to the previously presented applications, optical measurements related to the presence, and dynamics, of blood have many other applications. As an example, TOFS have been applied to the study of hemodynamics and metabolism in the infant brain [252–254]. As shown by Chance *et al.* despite the strong scattering of bone, TOFS can be used to non-invasively probe the hemoglobin oxygenation in the adult human brain [177]. This have opened the field of TOFS for functional measurements, such as hemodynamic changes due to cerebral activity [255–257].

Appendix A

The covariance matrix

In this appendix, the sum of the covariance matrix (Eq. 4.31) is calculated. The problem may be divided into tree parts, calculating the diagonal elements of the covariance matrix, $\langle \Delta x_i^2 \rangle$, calculating the non-diagonal elements of the matrix, $\langle \Delta x_i \Delta x_j \rangle$, and finally calculating the sum of all the elements in the matrix. To help solve the first two problems, Fig. A.1 illustrates two steps in a 3D random walk and the angles involved in calculating Δx_i. s_i is the step length and α_i is the angle between the direction at step i and the x-axis. The step increments in the x-direction, Δx_i are simply the step length s_i projected onto the x-axis

$$\Delta x_i = s_i \cos \alpha_i. \tag{A.1}$$

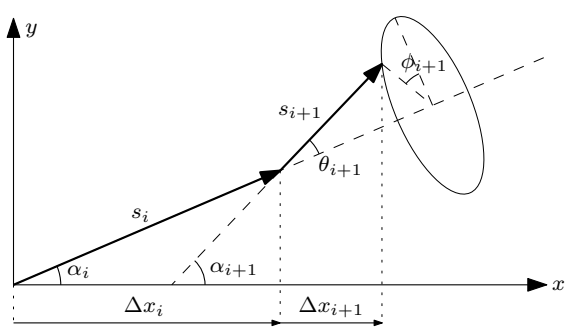

Figure A.1. *Two steps in a random walk in three dimensions, along with the projections of the steps onto the x-axis. The direction of the second step is determined by the direction of the former step as well as the deflection angle θ_{i+1} and the azimuthal angle ϕ_{i+1} (see Section 3.2). The angles α_j are the angles between the step direction and the x-axis.*

The step lengths s_i are independent random variables. As s_i follows an exponential distribution with the rate μ_s, the first four moments of s_i are: $\langle s_i \rangle = 1/\mu_s$, $\langle s_i^2 \rangle = 2/\mu_s^2$, $\langle s_i^3 \rangle = 6/\mu_s^3$, and $\langle s_i^4 \rangle = 24/\mu_s^4$.

The next direction angle, α_{i+1}, can be expressed as a function of the cosine of the current direction angle, α_i, the deflection angle, θ_{i+1}, and the azimuthal angle, ϕ_{i+1}:

$$\cos \alpha_{i+1} = \cos \theta_{i+1} \cos \alpha_i + \cos \phi_{i+1} \sin \theta_{i+1} \sin \alpha_i. \tag{A.2}$$

The two angles, θ_n and ϕ_n can be considered independent random variables. Also, for $m \neq n$, θ_n and θ_m, are independent. The same holds for ϕ_n and ϕ_m.

Assuming that the distribution of directions is isotropic at all times (basically, isotropic source or late enough so that the angular distribution have reached equilibrium in an isotropic medium) the distribution of step lengths projected onto an axis is uniform. That is, the cosine of the angle α is uniformly distributed $\in [-1, 1]$. Hence, $\cos \alpha_i$ has the following raw moments: $\langle \cos \alpha_i \rangle = 0$, $\langle \cos^2 \alpha_i \rangle = 1/3$, $\langle \cos^3 \alpha_i \rangle = 0$, $\langle \cos^4 \alpha_i \rangle = 1/5$.

Three rules are great to keep in mind for the calculations ahead:

- For all even distributions, all the odd moments are zero.
- For two random variables, X and Y, $\langle X + Y \rangle = \langle X \rangle + \langle Y \rangle$ always holds.
- For independent random variables, $\langle XY \rangle = \langle X \rangle \langle Y \rangle$ also holds.

A.0.3 $\langle \Delta x_i^2 \rangle$

The diagonal elements of the covariance matrix are

$$\langle \Delta x_i^2 \rangle = \langle s_i^2 \cos^2 \alpha_i \rangle = \langle s_i^2 \rangle \langle \cos^2 \alpha_i \rangle = \frac{2}{\mu_s^2} \frac{1}{3}. \tag{A.3}$$

A.0.4 $\langle \Delta x_i \Delta x_j \rangle$

The non-diagonal elements of the covariance matrix are not trivial as the random variables Δx_i and Δx_j $(i \neq j)$ are dependent, as clearly shown by Eq. A.2. For simplicity $j = i + 1$ is initially considered

$$\begin{aligned} \langle \Delta x_i \Delta x_{i+1} \rangle &= \langle s_i \cos \alpha_i s_{i+1} \cos \alpha_{i+1} \rangle \\ &= \langle s_i \rangle \langle s_{i+1} \rangle \langle \cos \alpha_i \cos \alpha_{i+1} \rangle. \end{aligned} \tag{A.4}$$

The term containing the dependency, $\langle \cos\alpha_i \cos\alpha_{i+1}\rangle$ may be rewritten using Eq. A.2

$$\begin{aligned}
&\langle \cos\alpha_i \cos\alpha_{i+1}\rangle = \\
&= \langle \cos\alpha_i(\cos\theta_{i+1}\cos\alpha_i + \cos\phi_{i+1}\sin\theta_{i+1}\sin\alpha_i)\rangle \\
&= \langle \cos\theta_{i+1}\cos^2\alpha_i + \cos\phi_{i+1}\sin\theta_{i+1}\sin\alpha_i\cos\alpha_i\rangle \\
&= \langle \cos\theta_{i+1}\cos^2\alpha_i\rangle + \langle \cos\phi_{i+1}\sin\theta_{i+1}\sin\alpha_i\cos\alpha_i\rangle \\
&= \langle \cos\theta_{i+1}\rangle\langle\cos^2\alpha_i\rangle + \langle\cos\phi_{i+1}\rangle\langle\sin\theta_{i+1}\rangle\langle\sin\alpha_i\cos\alpha_i\rangle.
\end{aligned} \tag{A.5}$$

The azimuthal angle ϕ is uniformly distributed in $(0, 2\pi]$. Thus, $\cos\phi$ is an even function and $\langle\cos\phi_i\rangle = 0$. The average cosine of the deflection angle is $g = \langle\cos\theta_j\rangle$, as described in Section 2.2.2,

$$\begin{aligned}
\langle \Delta x_i \Delta x_{i+1}\rangle &= \langle s_i\rangle\langle s_{i+1}\rangle\langle\cos\theta_{i+1}\rangle\langle\cos^2\alpha_i\rangle \\
&= \frac{1}{\mu_s}\frac{1}{\mu_s} g \frac{1}{3} = \frac{g}{3\mu_s^2}.
\end{aligned} \tag{A.6}$$

The same approach may be used for $j = i + a$

$$\begin{aligned}
\langle \Delta x_i \Delta x_{i+a}\rangle &= \langle s_i \cos\alpha_i s_{i+a}\cos\alpha_{i+a}\rangle \\
&= \langle s_i\rangle\langle s_{i+a}\rangle\langle\cos\alpha_i\cos\alpha_{i+a}\rangle.
\end{aligned} \tag{A.7}$$

The term $\langle\cos\alpha_i\cos\alpha_{i+a}\rangle$ may be approached as before

$$\begin{aligned}
&\langle \cos\alpha_i \cos\alpha_{i+a}\rangle = \\
&= \langle \cos\alpha_i(\cos\theta_{i+a}\cos\alpha_{i+(a-1)} + \cos\phi_{i+a}\sin\theta_{i+a}\sin\alpha_{i+(a-1)})\rangle \\
&= \langle \cos\theta_{i+a}\cos\alpha_i\cos\alpha_{i+(a-1)} + \cos\phi_{i+a}\sin\theta_{i+a}\sin\alpha_{i+(a-1)}\cos\alpha_i\rangle \\
&= \langle \cos\theta_{i+a}\cos\alpha_i\cos\alpha_{i+(a-1)}\rangle + \langle\cos\phi_{i+a}\sin\theta_{i+a}\sin\alpha_{i+(a-1)}\cos\alpha_i\rangle \\
&= \langle\cos\theta_{i+a}\rangle\langle\cos\alpha_i\cos\alpha_{i+(a-1)}\rangle + \langle\cos\phi_{i+a}\rangle\langle\sin\theta_{i+a}\rangle\langle\sin\alpha_{i+(a-1)}\cos\alpha_i\rangle \\
&= g\langle\cos\alpha_i\cos\alpha_{i+(a-1)}\rangle.
\end{aligned} \tag{A.8}$$

Every iteration, a $\langle\cos\phi\rangle$-term appears and removes the involved part. Also, every iteration a factor g appears in front of the final expression. Iterating Eq. A.8 a times yields

$$\langle\cos\alpha_i\cos\alpha_{i+a}\rangle = g^a\langle\cos^2\alpha_i\rangle, \tag{A.9}$$

which in turn gives

$$\langle\Delta x_i\Delta x_{i+a}\rangle = \frac{g^a}{3\mu_s^2}. \tag{A.10}$$

A.0.5 The sum of the covariance matrix

Using Eq. A.10 and Eq. A.10 the covariance matrix may be stated

$$\Sigma_{jk} = \frac{1}{3\mu_s^2}\begin{pmatrix} 2 & g & g^2 & ... & g^{n-1} \\ g & 2 & g & ... & g^{n-2} \\ g^2 & g & 2 & ... & g^{n-3} \\ ... & ... & ... & ... & ... \\ g^{n-1} & g^{n-2} & g^{n-3} & ... & 2 \end{pmatrix}. \tag{A.11}$$

In order to calculate the sum of the matrix, the sum $1 + g + g^2 + g^3 + ... + g^n$ is recognized as a geometrical series which, for $g < 1$, and assuming that n is large, may be calculated using

$$\sum_{k=0}^{\infty} g^k = \frac{1}{1-g}. \tag{A.12}$$

The sum of the covariance matrix calculated approximately

$$\langle x_n^2 \rangle = \sum_{j=1}^{n}\left(\sum_{k=1}^{n}\Sigma_{jk}\right) \overset{n\gg 1}{\approx} \frac{2n}{3\mu_s^2(1-g)}. \tag{A.13}$$

Exact covariance matrix sum

The sum of the covariance matrix may also be calculated exactly

$$\langle x_n^2 \rangle = \sum_{j=1}^{n}\left(\sum_{k=1}^{n}\Sigma_{jk}\right) = \frac{1}{3\mu_s^2}\left(\sum_{k=0}^{n-1} 2(n-k)g^k\right). \tag{A.14}$$

The new sum is identified as two geometric series

$$\begin{aligned} \sum_{k=0}^{n-1} 2(n-k)g^k &= 2n\sum_{k=0}^{n-1} g^k - 2\sum_{k=0}^{n-1} kg^k \\ &= 2(n+1)\sum_{k=0}^{n-1} g^k - 2\sum_{k=1}^{n} kg^{k-1}. \end{aligned} \tag{A.15}$$

Using

$$\sum_{k=0}^{n} g^k = \frac{1-g^{n+1}}{1-g}, \tag{A.16}$$

and

$$\sum_{k=1}^{n} kg^{k-1} = \frac{1-g^{n+1}}{(1-g)^2} - \frac{(n+1)g^n}{1-g}, \tag{A.17}$$

the sum can be calculated

$$\sum_{k=0}^{n-1} 2(n-k)g^k = \frac{2(n+1)}{1-g} - 2\frac{1-g^{n+1}}{(1-g)^2}. \tag{A.18}$$

Finally

$$\langle x_n^2 \rangle = \frac{2}{3\mu_s^2} \left(\frac{n+1}{1-g} - \frac{1-g^{n+1}}{(1-g)^2} \right). \tag{A.19}$$

A.0.6 Dimensionality

It is of interest to briefly mention the role of dimensionally when calculating $\langle x_n^2 \rangle$ and hence the diffusion coefficient. The influence of dimensionality enters the calculations when considering the projection of the step length s_i onto the x-axis. In three dimensions the projection is given by Eq. A.1 in combination with Eq. A.2.

Considering a random walk in 2D the azimuthal angle disappears *i.e.* $\cos\alpha_{i+1} = \cos(\alpha_i + \theta_{i+1})$. $\cos\alpha_{i+1}$ is no longer uniformly distributed. Instead α_{i+1} is uniformly distributed in $[0, 2\pi)$ and the moments of the projections are $\langle \cos\alpha_i \rangle = 0$, $\langle \cos^2\alpha_i \rangle = 1/2$ etc. Similarly in 1D, no angles exist and the "projection" is either 1 or -1. The first and second moments of this distribution are zero and one respectively.

In conclusion, the sum of the covariance matrix may be generalized to N dimensions by replacing the $1/3$ factor that appears in Eq. A.19 (or Eq. A.13). The approximative expression for the diffusion coefficient in N dimensions is (from Eq. 4.37)

$$D_x = \frac{\langle x_n^2 \rangle}{2n\langle \Delta t \rangle} = \frac{\frac{2n}{N\mu_s^2(1-g)}}{2n\frac{1}{v\mu_s}} = \frac{v}{N\mu_s(1-g)} = \frac{v}{N\mu_s'}. \tag{A.20}$$

Comments on the papers

I **White Monte Carlo for time-resolved photon migration**
E. Alerstam, S. Andersson-Engels, and T. Svensson.
Journal of Biomedical Optics **13**, 041304 (2008).

This paper reports on the development of a White Monte Carlo (WMC) based scheme for evaluation of experimental time-of-flight data. The paper shows the need to replace diffusion modelling in the evaluation of data in a wide range of optical properties, relevant for many clinical applications. Experimental investigations using intralipid are illustrates the improved performance of the WMC model in an interstitial configuration.

I developed the MC code and the fast code for post-processing of the MC simulation data. I did a major part of the experimental work and did the data analysis. I wrote a minor part of the manuscript.

II **Parallel computing with graphics processing units for high-speed Monte Carlo simulation of photon migration**
E. Alerstam, T. Svensson, and S. Andersson-Engels.
Journal of Biomedical Optics **13**, 060504 (2008).

This letter introduces the use of graphics processing units (GPUs) to accelerate Monte Carlo simulations of light transport in turbid media. The benefit of using GPUs for Monte Carlo simulations is demonstrated by running a simulation in a semi-infinite geometry showing a speedup of three orders of magnitude. Issues related to GPU- and parallel programming, such as random number generation, are addressed.

I came up with the idea to test GPUs for our Monte Carlo simulation needs, did the programming and validation, and I wrote a major part of the manuscript.

III **Next-generation acceleration and code optimization for light transport in turbid media using GPUs**
E. Alerstam, W. C. Y. Lo, T. D. Han, J. Rose, S. Andersson-Engels, and L. Lilge.
Biomedical Optics Express **1**, 658-675 (2010).

In this paper, the work in Paper **II** is expanded. A GPU version of a popular Monte Carlo program (MCML [92]) is presented and several issues with writing GPU accelerated light transport Monte Carlo codes are addressed. Methods to make the best use of the capabilities of modern GPUs are presented, showing that significant acceleration ($\sim$ 600$\times$ in this case) is possible even for more complicated simulations.

I co-developed the code and did a major part of the validation. I prepared major parts of the manuscript.

IV **Towards accurate in vivo spectroscopy of the human prostate**
T. Svensson, E. Alerstam, M. Einarsdóttír, K. Svanberg, and S. Andersson-Engels.
Journal of Biophotonics **1**, 200-203 (2008).

This letter reports on the use of the WMC modelling developed in Paper **I** for evaluation of TOFS-based prostate spectroscopy. Due to the relatively high absorption and low scattering of the prostate, this paper shows that diffusion modelling, as used in a previous study [105], will induce significant errors in derived optical properties. Due to an important improvement in the measurement of the instrument response function, the data from the previous study could not be re-evaluated with the WMC model and the paper is thus based on new data.

I took part in the experimental work, was responsible for data evaluation, and I took part in writing the manuscript.

V **Near-infrared photon time-of-flight spectroscopy of turbid materials up to 1400 nm**
T. Svensson, E. Alerstam, D. Khoptyar, J. Johansson, S. Folestad and S. Andersson-Engels.
Review of Scientific Instruments **80**, 063105 (2009).

This paper describes a TOFS instrument, based on TCSPC technology, capable of measuring in the spectral range from 650 up to 1400 nm. This is achieved by using dual MCP-PMT detectors in combination with a super-continuum fibre laser in combination with a dual AOTF spectral filtering system. In pharmaceutical applications it is imperative to reach up into the region above 1000 nm where the spectral features of the pharmaceutical constituents are prominent.

I participated in the design and construction of the system, including characterization of the laser source and spectral filtering system.

VI **Improved accuracy in time-resolved diffuse reflectance spectroscopy**
E. Alerstam, S. Andersson-Engels and T. Svensson.
Optics Express **16**, 10434-10448 (2008).

In this paper the WMC model from Paper **I** is used to investigate the need for improved modelling in time-resolved diffuse reflectance measurements, *i.e.* in semi-infinite geometries. The importance of proper modelling is further discussed. Experiments were conducted on a set of internationally used reference samples [104] and the resulting characterization of the reference samples is thus an important contribution to the MEDPHOT initiative for performance assessment of photon migration instruments.

I was responsible for the experimental work and the data analysis. I made substantial contributions to manuscript preparation.

VII **Optical porosimetry and investigations of the porosity experienced by light interacting with porous media**
T. Svensson, E. Alerstam, J. Johansson, and S. Andersson-Engels.
Optics Letters **35**, 1740-1742 (2010).

In this letter TOFS is used in combination with laser-based gas sensing to investigate how light interacts with porous materials. In comparison with a standard, but destructive, porosimetry technique it is found that the non-intrusive optical technique underestimates the sample porosity but also that there is a strong correlation between results. The need for improved modelling is emphasised.

I participated in the experimental work and contributed to the data evaluation and analysis.

VIII **Observation of anisotropic diffusion of light in compacted granular porous materials**
E. Alerstam, and T. Svensson.
(2011) *arXiv 1111.1700v1, to be submitted.*

In this work, the observation of anomalous diffusion of light in compacted granular porous materials is reported. It is shown that an anisotropic diffusion model may explain the anomalous behaviour suggesting that the micro-structure of the samples is anisotropic, a conclusion supported by measurements using other modalities. These findings introduce a problem to model based optical techniques to characterize *e.g.* compacted pharmaceutical samples but also suggest that important structural properties may be revealed by non-destructive optical techniques.

I was responsible for the experimental setup and measurements. I did the modelling-related work, such as data evaluation, and I helped prepare the samples. I made minor contributions to the manuscript.

IX **Toward single-fiber diffuse optical time-of-flight spectroscopy**
E. Alerstam, T. Svensson, S. Andersson-Engels, L. Spinelli, D. Contini, A. Dalla Mora, A. Tosi, F. Zappa and A. Pifferi. (2011) *Manuscript in preparation.*

This manuscript describes our work towards a novel TOFS system, capable of interstitial spectroscopic measurements using a single fibre to deliver light to and collect light from the sample. The intention is to simplify clinical interstitial measurements by alleviating the need to use, and keep track of the positions of, multiple fibres, reducing the invasiveness of the measurement. Using Monte Carlo simulations and phantom experiments it is shown that the effect of scattering and absorption properties are separable and that the absorption coefficient may be accurately assessed in a wide range of clinically relevant optical properties. Apart from theoretical proof of principle, a single Monte Carlo simulation is used as part of the forward model in the data evaluation.

I initiated the collaboration and did Monte Carlo simulations to prove the concept. I participated in the experimental design and took part in all experimental work. I did the data evaluation and analysis, and contributed to a major part of the manuscript.

Acknowledgements

First, I would like to express my deepest gratitude to Stefan Andersson-Engels for guiding me though my Ph.D. studies. Thank you for giving me this great opportunity and for giving me the freedom to explore my ideas. Your enthusiasm and positive attitude have meant a lot to me and I will always be grateful for your support and encouragement.

I would like to thank my co-supervisors: Katarina Svanberg for your help and, in particular, for your hospitality and support during conferences. Jonas Johansson for your encouragement and for sharing your interesting problems. And last, but certainly not least, Tomas Svensson in whom I found a true friend. Thanks for all the enlightening discussions, all the support you have given me, and all the great times we have shared.

Thanks to all my colleagues and friends in the Biophotonics group; in particular, Pontus Svenmarker for being an outstanding travelling companion, and Johan Axelsson for interesting discussions, and for your encouragement during the writing of this thesis. Can Xu, Haiyan Xie, Haichun Liu, Dmitry Khoptyar, and Emilie Krite-Svanberg - present members of the group, thank you for your friendship and our exciting work together.

I would also like to thank all my colleagues at the Atomic Physics Division, both former and present, for providing a friendly and stimulating environment. In particular, I would like to thank Marcus Dahlström for our interesting physics discussions and Märta Lewander for pleasant lunch and coffee breaks. Teaching with Johan Mauritsson have been a true pleasure. Thank you very much for the opportunity to do so, as well as for the pleasant wine tastings.

Our collaborators outside of the Physics department: the kind and helpful members of the brachytherapy team at Lund University Hospital, our colleagues at polytecnico di Milano, and our GPU-MCML collaborators at University of Toronto. Thank you all!

Having Markus Nilsson and Johannes Töger around, simultaneously pursuing their Ph.D.'s, have been invaluable. Thanks for

all of our interesting discussions, for your support, and for being wonderful friends!

The support of all my great friends have been very much appreciated. Thank you all for reminding me of what is truly important in life.

Finally, my beloved family deserves my deepest gratitudes for their unconditional support and encouragement.

References

1. S. Svanberg. *Atomic and molecular spectroscopy.* Springer (2001).

2. D. A. Skoog, D. M. West, F. J. Holler and S. R. Crouch. *Fundamentals of analytical chemistry.* Thomson-Brooks/Cole eighth edition (2004).

3. D. F. Gray. *The observation and analysis of stellar photospheres.* Cambridge University Press third edition (2005).

4. A. K. Pradhan and N. N. Sultana. *Atomic Astrophysics and Spectroscopy.* Cambridge University Press (2011).

5. C. Weitkamp. *Lidar Range-Resolved Optical Remote Sensing of the Atmosphere.* Springer (2005).

6. K. Kohse-Hönighaus and J. B. Jeffries, editors. *Applied combustion diagnostics.* Taylor & Francis (2002).

7. J.E. Hansen and J.W. Hovenier. *Interpretation of the polarization of Venus.* J. Atmos. Sci **31**, 1137–1160 (1974).

8. J. G. J. Peelen and R. Metselaar. *Light-scattering by pores in polycrystalline materials - transmission properties of alumina.* J. Appl. Phys. **45**, 216–220 (1974).

9. G.A. Millikan. *The oximeter, an instrument for measuring continuously the oxygen saturation of arterial blood in man.* Rev. Sci. Instrum. **13**, 434–444 (1942).

10. V. Backman, M.B. Wallace, L.T. Perelman, J.T. Arendt, R. Gurjar, M.G. Muller, Q. Zhang, G. Zonios, E. Kline, T. McGillican, S. Shapshay, T. Valdez, K. Badizadegan, J.M. Crawford, M. Fitzmaurice, S. Kabani, H.S. Levin, M. Seiler, R.R. Dasari, I. Itzkan, J. Van Dam and M.S. Feld. *Detection of preinvasive cancer cells.* Nature **406**, 35–36 (2000).

11. A.E. Cerussi, D. Jakubowski, N. Shah, F. Bevilacqua, R. Lanning, A.J. Berger, D. Hsiang, J. Butler, R.F. Holcombe and B.J. Tromberg. *Spectroscopy enhances the information content of optical mammography.* J. Biomed. Opt. **7**, 60–71 (2002).

12. T. H. Pham, R. Hornung, M. W. Berns, Y. Tadir and B. J. Tromberg. *Monitoring tumor response during photodynamic therapy using near-infrared photon-migration spectroscopy.* Photochem. Photobiol. **73**, 669–677 (2001).

13. A. Johansson, T. Johansson, M. Soto Thompson, N. Bendsoe, K. Svanberg, S. Svanberg and S. Andersson-Engels. *In vivo measurement of parameters of dosimetric importance during photodynamic therapy of thick skin tumors.* J. Biomed. Opt. **11**, 034029 (2006).

14. A. Cerussi, D. Hsiang, N. Shah, R. Mehta, A. Durkin, J. Butler and B.J. Tromberg. *Predicting response to breast cancer neoadjuvant chemotherapy using diffuse optical spectroscopy.* P. Natl. Acad. Sci. USA **104**, 4014–4019 (2007).

15. D Roblyer, S. Ueda, A. Cerussi, W. Tanamai, A. Durkin, R. Mehta, D. Hsiang, J. Butler, C. McLaren, W.-P. Chen and B. J. Tromberg. *Optical imaging of breast cancer oxyhemoglobin flare correlates with neoadjuvant chemotherapy response one day after starting treatment.* P. Natl. Acad. Sci. USA **108**, 14626–14631 (2011).

16. J. H. Woodhams, A. J. MacRobert and S. G. Bown. *The role of oxygen monitoring during photodynamic therapy and its potential for treatment dosimetry.* Photochem. Photobiol. **6**, 1246–1256 (2007).

17. M. Nilsson, E. Alerstam, S. Brockstedt, R. Wirestam, F. Ståhlberg and J. Lätt. Fast Monte Carlo Simulations Replace Analytical Tissue Models in Diffusion MRI (2009). URL `http://www.ismrm.org/09/Session46.htm`.

18. J. D. Jackson. *Classical Electrodynamics, 3rd edition.* John Wiley & Sons, Inc. (1998).

19. J. Rička and M. Frenz. *Polarized Light: Electrodynamic Fundamentals* chapter Optical-Thermal Response of Laser-Irradiated Tissue, pages 65–108. Springer 2 edition (2010).

20. M. I. Mishchenko. *Gustav Mie and the fundamental concept of electromagnetic scattering by particles: A perspective.* J. Quant. Spectrosc. Rad. Transfer **110**, 1210–1222 (2009).

21. C.F. Bohren and D.R. Huffman. *Absorption and scattering of light by small particles.* Wiley (1983).

22. M.I. Mishchenko, L.D. Travis and A.A. Lacis. *Scattering, absorption, and emission of light by small particles.* Cambridge University Press (2002). URL `http://www.giss.nasa.gov/~crmim/books.html`.

23. A. Ishimaru. *Wave propagation and scattering in random media.* Academic Press (1978).

24. H. C. van de Hulst. *Multiple Light Scattering.* New York: Academic (1980).

25. M.I. Mishchenko, L.D. Travis and A.A. Lacis. *Multiple scattering of light by particles: radiative transfer and coherent backscattering.* Cambridge University Press (2006).

26. M. I. Mishchenko, V. K. Rosenbush, N. N. Kiselev, D. F. Lupishko, V. P. Tishkovets, V. G. Kaydash, I. N. Belskaya, Y. S. Efimov and N. M. Shakhovskoy. *Polarimetric Remote Sensing of Solar System Objects.* Akademperiodyka, Kyiv (2010).

27. J.W.S. Rayleigh. *On the light from the sky, its polarization and colour.* Phil. Mag. **41**, 107–120, 274–279 (1871).

28. J.W.S. Rayleigh. *On the scattering of light by small particles.* Phil. Mag. **41**, 447 (1871).

29. G. Mie. *Beiträge zur Optik trüber Medien, speziell kolloidaler Metallösungen.* Ann. Phys. **330**, 377–445 (1908).

30. S. Chandrasekhar. *Radiative transfer*. Dover Books on Physics. Dover Publications (1960).

31. J. Rička and M. Frenz. *From Electrodynamics to Monte Carlo Simulations* chapter Optical-Thermal Response of Laser-Irradiated Tissue, pages 203–266. Springer 2 edition (2010).

32. L. L. Foldy. *The Multiple Scattering of Waves*. Phys. Rev. **67**, 107–119 (1945).

33. J. M. Schmitt and G. Kumar. *Turbulent nature of refractive-index variations in biological tissue*. Opt. Lett. **21**, 1310–1312 (1996).

34. T.T. Wu, J.Y. Qu and M. Xu. *Unified Mie and fractal scattering by biological cells and subcellular structures*. Opt. Lett. **32**, 2324–2326 (2007).

35. M. Xu and R.R. Alfano. *Fractal mechanisms of light scattering in biological tissue and cells*. Opt. Lett. **30**, 3051–3053 (2005).

36. F.P. Bolin, L.E. Preuss, R.C. Taylor and R.J. Ference. *Refractive-index of some mammalian-tissues using a fiber optic cladding method*. Appl. Opt. **28**, 2297–2303 (1989).

37. J.M. Schmitt and G. Kumar. *Optical scattering properties of soft tissue: a discrete particle model*. Appl. Opt. **37**, 2788–2797 (1998).

38. J.R. Mourant, T. Fuselier, J. Boyer, T.M. Johnson and I.J. Bigio. *Predictions and measurements of scattering and absorption over broad wavelength ranges in tissue phantoms*. Appl. Opt. **36**, 949–957 (1997).

39. A.M.K. Nilsson, C. Sturesson, D.L. Liu and S. Andersson-Engels. *Changes in spectral shape of tissue optical properties in conjunction with laser-induced thermotherapy*. Appl. Opt. **37**, 1256–1267 (1998).

40. S. Prahl. Mie Scattering Calculator (2011). URL `http://omlc.ogi.edu/calc/mie_calc.html`.

41. L.G. Henyey and J.L. Greenstein. *Diffuse radiation in the galaxy*. Astrophys. J. **93**, 70–83 (1941).

42. S. Jacques, C. Alter and S. Prahl. *Angular dependence of HeNe laser light scattering by human dermis*. Lasers Life Sci. **1**, 309–333 (1987).

43. M. Sjöholm, G. Somesfalean, J. Alnis, S. Andersson-Engels and S. Svanberg. *Analysis of gas dispersed in scattering media*. Opt. Lett. **26**, 16–18 (2001).

44. P. A. Valdes, A. Kim, F. Leblond, O. M. Conde, B. T. Harris, K. D. Paulsen, B. C. Wilson and D. W. Roberts. *Combined fluorescence and reflectance spectroscopy for in vivo quantification of cancer biomarkers in low- and high-grade glioma surgery*. J. Biomed. Opt. **16**, 116007 (2011).

45. B. C. Wilson and M. S. Patterson. *The physics, biophysics and technology of photodynamic therapy*. Phys. Med. Biol. **53**, R61–R109 (2008).

46. S.A. Prahl. Optical absorption of hemoglobin (2006). URL `http://omlc.ogi.edu/spectra/hemoglobin/index.html`.

47. G.M. Hale and M.R. Querry. *Optical constants of water in 200-nm to 200-μm wavelength region*. Appl. Opt. **12**, 555–563 (1973).

48. R.L.P. van Veen, H.J.C.M. Sterenborg, A. Pifferi, A. Torricelli, E. Chikoidze and R. Cubeddu. *Determination of visible near-IR absorption coefficients of mammalian fat using time- and spatially resolved diffuse reflectance and transmission spectroscopy.* J. Biomed. Opt. **10**, 054004 (2005).

49. S.L. Jacques. Optical absorption of melanin (2008). URL `http://omlc.ogi.edu/spectra/melanin/index.html`.

50. J.A. Parrish. *New concepts in therapeutic photomedicine - photochemistry, optical targeting and the therapeutic window.* J. Invest. Dermatol. **77**, 45–50 (1981).

51. E. Antonini and M. Brunori. *Hemoglobin and myoglobin in their reactions with ligands.* North-Holland Publishing Company (1971).

52. E.L. Hull and T.H. Foster. *Cytochrome spectroscopy in scattering suspensions containing mitochondria and red blood cells.* Appl. Spectrosc. **55**, 149–154 (2001).

53. A.M.K. Nilsson, D. Heinrich, J. Olajos and S. Andersson-Engels. *Near infrared diffuse reflection and laser-induced fluorescence spectroscopy for myocardial tissue characterisation.* Spectrochem. Acta A **53**, 1901–1912 (1997).

54. P. Taroni, D. Comelli, A. Pifferi, A. Torricelli and R. Cubeddu. *Absorption of collagen: effects on the estimate of breast composition and related diagnostic implications.* J. Biomed. Opt. **12**, 014021 (2007).

55. A. Schuster. *Radiation through a foggy atmosphere.* The Observatory **26**, 379–381 (1903).

56. A Schuster. *Radiation Through a Foggy Atmosphere.* Astrophys. J. **21**, 1–22 (1905).

57. K.M. Case and P.F. Zweifel. *Linear transport theory.* Addison-Wesley series in nuclear engineering. Addison-Wesley Pub. Co. (1967).

58. R. Longini and R. Zdrojkowski. *A Note on the Theory of Backscattering of Light by Living Tissue.* IEEE Trans. Biomed. Eng. **BME-15**, 4–10 (1968).

59. L. Reynolds, C. Johnson and A. Ishimaru. *Diffuse reflectance from a finite blood medium - applications to modeling of fiber optic catheters.* Appl. Opt. **15**, 2059–2067 (1976).

60. A.J. Welch and M.J.C. Gemert. *Optical-Thermal Response of Laser-Irradiated Tissue, second ed.* Springer 2 edition (2010).

61. E. Wolf. *New theory of radiative energy transfer in free electromagnetic fields.* Phys. Rev. D **13**, 869–886 (1976).

62. Ronald L. Fante. *Relationship between radiative-transport theory and Maxwell's equations in dielectric media.* J. Opt. Soc. Am. **71**, 460–468 (1981).

63. M. I. Mishchenko. *Vector radiative transfer equation for arbitrarily shaped and arbitrarily oriented particles: a microphysical derivation from statistical electromagnetics.* Appl. Opt. **41**, 7114–7134 (2002).

64. M. I. Mishchenko. *Maxwell's equations, radiative transfer, and coherent backscattering: a general perspective.* J. Quant. Spectrosc. Rad. Transfer **101**, 540–555 (2006).

65. M. I. Mishchenko. *Radiative Transfer-V* chapter Radiative transfer: a new look of the old theory, pages 1–30. Begell House, New York (2007).

66. Pierre-Etienne Wolf and Georg Maret. *Weak Localization and Coherent Backscattering of Photons in Disordered Media.* Phys. Rev. Lett. **55**, 2696– (1985).

67. Meint P. Van Albada and Ad Lagendijk. *Observation of Weak Localization of Light in a Random Medium.* Phys. Rev. Lett. **55**, 2692–2695 (1985).

68. Young L. Kim, Yang Liu, Vladimir M. Turzhitsky, Hemant K. Roy, Ramesh K. Wali and Vadim Backman. *Coherent backscattering spectroscopy.* Opt. Lett. **29**, 1906–1908 (2004).

69. Z. Yaqoob, D. Psaltis, M. S. Feld and C. Yang. *Optical phase conjugation for turbidity suppression in biological samples.* Nature Photon. **2**, 110–115 (2008).

70. X. Xu, H. Liu and L. V. Wang. *Time-reversed ultrasonically encoded optical focusing into scattering media.* Nature Photon. **5**, 154–157 (2011).

71. I. M. Vellekoop, A. Lagendijk and A. P. Mosk. *Exploiting disorder for perfect focusing.* Nature Photon. **4**, 320–322 (2010).

72. E.D. Aydin, C.R.E. de Oliveira and A.J.H. Goddard. *A finite element-spherical harmonics radiation transport model for photon migration in turbid media.* J. Quant. Spectrosc. Rad. Transfer **84**, 247 – 260 (2004).

73. S. Wright, M. Schweiger and S. R. Arridge. *Reconstruction in optical tomography using the PN approximations.* Meas. Sci. Technol. **18**, 79–86 (2007).

74. A. Liemert and A. Kienle. *Analytical solution of the radiative transfer equation for infinite-space fluence.* Phys. Rev. A **83**, 015804 (2011).

75. A. Liemert and A. Kienle. *Analytical Green's function of the radiative transfer radiance for the infinite medium.* Phys. Rev. E **83**, 036605 (2011).

76. A. D. Klose and E. W. Larsen. *Light transport in biological tissue based on the simplified spherical harmonics equations.* J. Comput. Phys. **220**, 441–470 (2006).

77. M. Frank, A. Klar, E. W. Larsen and S. Yasuda. *Time-dependent simplified PN approximation to the equations of radiative transfer.* J. Comput. Phys. **226**, 2289–2305 (2007).

78. M. Chu, K. Vishwanath, A. D. Klose and H. Dehghani. *Light transport in biological tissue using three-dimensional frequency-domain simplified spherical harmonics equations.* Phys. Med. Biol. **54**, 2493 (2009).

79. J. B. Domínguez and Y. Bérubé-Lauzière. *Diffuse light propagation in biological media by a time-domain parabolic simplified spherical harmonics approximation with ray-divergence effects.* Applied Optics **49**, 1414–1429 (2010).

80. Y. Bérubé-Lauzière and J. B. Issa, V. Domínguez. *Simplified spherical harmonics approximation of the time-dependent equation of radiative transfer for the forward problem in time-domain diffuse optical tomography.* In Bruce J. Tromberg, Arjun G. Yodh, Mamoru Tamura, Eva M. Sevick-Muraca and Robert R. Alfano, editors, *Proc. of SPIE, Optical Tomography and Spectroscopy of Tissue VIII* volume 7174 page 717403. SPIE (2009).

81. A. Liemert and A. Kienle. *Analytical solutions of the simplified spherical harmonics equations.* Opt. Lett. **35**, 3507–3509 (2010).

82. M. L. Adams and E. W. Larsen. *Fast iterative methods for discrete-ordinates particle transport calculations.* Prog. Nucl. Energ. **40**, 3 – 159 (2002).

83. K. Peng, X. Gao, X. Qu, N. Ren, X. Chen, X. He, X. Wang, J. Liang and J. Tian. *Graphics processing unit parallel accelerated solution of the discrete ordinates for photon transport in biological tissues.* Appl. Opt. **50**, 3808–3823 (2011).

84. D. Contini, F. Martelli and G. Zaccanti. *Photon migration through a turbid slab described by a model based on diffusion approximation: I. Theory.* Appl. Opt. **36**, 4587–4599 (1997).

85. K. Furutsu and Y. Yamada. *Diffusion-approximation for a dissipative random medium and the applications.* Phys. Rev. E **50**, 3634–3640 (1994).

86. T. Durduran, A.G. Yodh, B. Chance and D.A. Boas. *Does the photon-diffusion coefficient depend on absorption?* J. Opt. Soc. Am. A **14**, 3358–3365 (1997).

87. W. L. Dunn and J. K. Shultis. *Exploring Monte Carlo Methods.* Elsevier (2011).

88. S.A. Prahl. *Light Transport in Tissue.* PhD thesis, University of Texas at Austin (1988).

89. B.C. Wilson and G. Adam. *A Monte Carlo model for the absorption and flux distributions of light in tissue.* Med. Phys. **10**, 824–830 (1983).

90. J. J. Duderstadt and L. J. Hamilton. *Nuclear reactor analysis.* John Wiley & sons, Inc. (1976).

91. L. Wang and S.L. Jacques. *Monte Carlo modeling of light transport in multi-layered tissues in standard C* (1998).

92. L.H. Wang, S.L. Jacques and L.Q. Zheng. *MCML Monte Carlo modeling of light transport in multilayered tissues.* Comput. Meth. Prog. Bio. **47**, 131–146 (1995).

93. D.A. Boas, J.P. Culver, J.J. Stott and A.K. Dunn. *Three dimensional Monte Carlo code for photon migration through complex heterogeneous media including the adult human head.* Opt. Express **10**, 159–170 (2002).

94. M. O. Scully and M. Suhail Zubairy. *Quantum optics.* Cambridge University Press (1997).

95. I. Fredriksson, M. Larsson and T. Strömberg. *Forced detection Monte Carlo algorithms for accelerated blood vessel image simulations.* J. Biophoton. **2**, 178–184 (2009).

96. J. Swartling, A. Pifferi, A.M.K. Enejder and S. Andersson-Engels. *Accelerated Monte Carlo models to simulate fluorescence spectra from layered tissues.* J. Opt. Soc. Am. A **20**, 714–727 (2003).

97. A. N. Witt. *Multiple scattering in reflection nebulae. I. A Monte Carlo approach.* Astrophys. J. Suppl. Ser. **35**, 1–6 (1977).

98. J. Swartling. *Biomedical and atmospheric applications of optical spectroscopy in scattering media.* PhD thesis, Lund University (2002). URL `http://atomic.physics.lu.se/biophotonics`.

99. A. Pifferi, P. Taroni, G. Valentini and S. Andersson-Engels. *Real-time method for fitting time-resolved reflectance and transmittance measurements with a Monte Carlo model.* Appl. Opt. **37**, 2774–2780 (1998).

100. R. Graaff, M.H. Koelink, F.F.M. Demul, W.G. Zijlstra, A.C.M. Dassel and J.G. Aarnoudse. *Condensed Monte Carlo simulations for the description of light transport.* Appl. Opt. **32**, 426–434 (1993).

101. A. Kienle and M.S. Patterson. *Determination of the optical properties of turbid media from a single Monte Carlo simulation.* Phys. Med. Biol. **41**, 2221–2227 (1996).

102. A. Pifferi, R. Berg, P. Taroni and S. Andersson-Engels. *Fitting of Time-resolved reflectance curves with a Monte Carlo model.* In *Trends in optics and Photonics: Advances in Optical Imaging and Photon Migration* volume 2 pages 311–314. Optical Society of America (1996).

103. H. P. Xu, T. J. Farrell and M. S. Patterson. *Investigation of light propagation models to determine the optical properties of tissue from interstitial frequency domain fluence measurements.* J. Biomed. Opt. **11**, 041104 (2006).

104. A. Pifferi, A. Torricelli, A. Bassi, P. Taroni, R. Cubeddu, H. Wabnitz, D. Grosenick, M. Moller, R. MacDonald, J. Swartling, T. Svensson, S. Andersson-Engels, R.L.P. van Veen, H.J.C.M. Sterenborg, J.M. Tualle, H.L. Nghiem, S. Avrillier, M. Whelan and H. Stamm. *Performance assessment of photon migration instruments: the MEDPHOT protocol.* Appl. Opt. **44**, 2104–2114 (2005).

105. T. Svensson, S. Andersson-Engels, M. Einarsdóttír and K. Svanberg. *In vivo optical characterization of human prostate tissue using near-infrared time-resolved spectroscopy.* J. Biomed. Opt. **12**, 014022 (2007).

106. L. Wang, S.L. Jacques and L. Zheng. *CONV-convolution for responses to a finite diameter photon beam incident on multi-layered tissues.* Comput. Meth. Prog. Bio. **54**, 141–150 (1997).

107. N.S. Zolek, A. Liebert and R. Maniewski. *Optimization of the Monte Carlo code for modeling of photon migration in tissue.* Comput. Meth. Prog. Bio. **84**, 50–57 (2006).

108. W. C. Y. Lo, K. Redmond, J. Luu, P. Chow, J. Rose and L. Lilge. *Hardware acceleration of a Monte Carlo simulation for photodynamic treatment planning.* J. Biomed. Opt. **14**, 014019 (2009).

109. D. R. Kirkby and D. T. Delpy. *Parallel operation of Monte Carlo simulations on a diverse network of computers.* Phys. Med. Biol. **42**, 1203–1208 (1997).

110. A. Colasanti, G. Guida, A. Kisslinger, R. Liuzzi, M. Quarto, P. Riccio, G. Roberti and F. Villani. *Multiple processor version of a Monte Carlo code for photon transport in turbid media.* Comput. Phys. Commun. **132**, 84–93 (2000).

111. H. Shen and G. Wang. *A tetrahedron-based inhomogeneous Monte Carlo optical simulator.* Phys. Med. Biol. **55**, 947–962 (2010).

112. D. Blythe. *Rise of the graphics processor.* Proc. IEEE **96**, 761–778 (2008).

113. NVIDIA CUDA C Programming Guide 4.0. Technical report NVIDIA-Corporation (2011). URL `www.nvidia.com/cuda`.

114. Q. Fang and D. A. Boas. *Monte Carlo simulation of photon migration in 3D turbid media accelerated by graphics processing units.* Opt. Express **17**, 20178–20190 (2009).

115. A. Badal and A. Badano. *Accelerating Monte Carlo simulations of photon transport in a voxelized geometry using a massively parallel graphics processing unit.* Med. Phys. **36**, 4878–4880 (2009).

116. N. Ren, J. Liang, X. Qu, J. Li, B. Lu and J. Tian. *GPU-based Monte Carlo simulation for light propagation in complex heterogeneous tissues.* Opt. Express **18**, 6811–6823 (2010).

117. N. Carbone, H. Di Rocco, D. I. Iriarte and J. A. Pomarico. *Solution of the direct problem in turbid media with inclusions using Monte Carlo simulations implemented in graphics processing units: new criterion for processing transmittance data.* J. Biomed. Opt **15**, 035002 (2010).

118. A. Doronin and I. Meglinski. *Online object oriented Monte Carlo computational tool for the needs of biomedical optics.* Biomed. Opt. Express **2**, 2461–2469 (2011).

119. T. S. Leung and S. Powell. *Fast Monte Carlo simulations of ultrasound-modulated light using a graphics processing unit.* J. Biomed. Opt **15**, 055007 (2010).

120. K.M. Yoo, F. Liu and R.R. Alfano. *When does the diffusion-approximation fail to describe photon transport in random-media.* Phys. Rev. Lett. **64**, 2647–2650 (1990).

121. J.B. Fishkin, S. Fantini, M.J. VandeVen and E. Gratton. *Gigahertz photon density waves in a turbid medium: theory and experiments.* Phys. Rev. E **53**, 2307–2319 (1996).

122. A. Kienle and M. S. Patterson. *Improved solutions of the steady-state and the time-resolved diffusion equations for reflectance from a semi-infinite turbid medium.* J. Opt. Soc. Am. A **14**, 246–254 (1997).

123. F. Martelli, M. Bassani, L. Alianelli, L. Zangheri and G. Zaccanti. *Accuracy of the diffusion equation to describe photon migration through an infinite medium: numerical and experimental investigation.* Phys. Med. Biol. **45**, 1359–1373 (2000).

124. R. Elaloufi, R. Carminati and J.-J. Greffet. *Diffusive-to-ballistic transition in dynamic light transmission through thin scattering slabs: a radiative transfer approach.* J. Opt. Soc. Am. A **21**, 1430–1437 (2004).

125. T. Svensson. *Pharmaceutical and biomedical applications of spectroscopy in the photon migration regime.* PhD thesis, Lund University (2008). URL `http://atomic.physics.lu.se/biophotonics`.

126. L. Marti-Lopez, J.C. Hebden and J. Bouza-Dominguez. *Estimates of minimum pulse width and maximum modulation frequency for diffusion optical tomography.* Opt. Laser Eng. **44**, 1172–1184 (2006).

127. M. Bassani, F. Martelli, G. Zaccanti and D. Contini. *Independence of the diffusion coefficient from absorption: Experimental and numerical evidence.* Opt. Lett. **22**, 853–855 (1997).

128. T. Nakai, G. Nishimura, K. Yamamoto and M. Tamura. *Expression of optical diffusion coefficient in high-absorption turbid media.* Phys. Med. Biol. **42**, 2541–2549 (1997).

129. R. Graaff and J.J. Ten Bosch. *Diffusion coefficient in photon diffusion theory.* Opt. Lett. **25**, 43–45 (2000).

130. R. Pierrat, L. J. Greffet and R. Carminati. *Photon diffusion coefficient in scattering and absorbing media.* J. Opt. Soc. Am. A **23**, 1106–1110 (2006).

131. L. Bachelier. *Théorie de la spéculation.* Annales Scientifiques de l'École Normale Supérieure **3**, 21–86 (1900).

132. A. Einstein. *On the movement of small particles suspended in stationary liquids required by the molecular-kinetic theory of heat.* Ann. der Physik **17**, 549–560 (1905).

133. L. Vlahos, H. Isliker, Y. Kominis and K. Hizanidis. *Normal and Anomalous Diffusion: A Tutorial.* In T. Bountis, editor, *Order and Chaos* volume 10. Patras University Press (2008). (arXiv:0805.0419).

134. B. D. Hughes. *Random Walks and Random Environments, Volume 1.* Oxford University Press (1995).

135. G. Zaccanti, E. Battistelli, P. Bruscaglioni and Q. N. Wei. *Analytic relationships for the statistical moments of scattering point coordinates for photon migration in a scattering medium.* Pure Appl. Opt. **3**, 897–905 (1994).

136. A. H. Gandjbakhche, R. F. Bonner and R. Nossal. *Scaling Relationships for Anisotropic Random Walks.* J. Stat. Phys. **69**, 35–53 (1992).

137. J.-P. Bouchaud and Georges A. *Anomalous diffusion in disordered media: Statistical mechanisms, models and physical applications.* Phys. Rep. **195**, 127 – 293 (1990).

138. E. W. Montroll and G. H. Weiss. *Random Walks on Lattices. II.* J. Math. Phys. **6**, 167–181 (1965).

139. G. H. Weiss, J. M. Porra and J. Masoliver. *The continuous-time random walk description of photon migration in an isotropic medium.* Opt. Commun. **146**, 268–276 (1998).

140. M. Evans, N. Hastings and B. Peacock. *Statistical distributions 3.ed.* Wiley, New York (2000).

141. R. Graaff, J.G. Aarnoudse, F.F.M. Demul and H.W. Jentink. *Similarity relations for anisotropic scattering in absorbing media.* Opt. Eng. **32**, 244–252 (1993).

142. J. R. Mourant, J. Boyer, A. H. Hielscher and I. J. Bigio. *Influence of the scattering phase function on light transport measurements in turbid media performed with small source-detector separations.* Opt. Lett. **21**, 546–548 (1996).

143. F. Bevilacqua and C. Depeursinge. *Monte Carlo study of diffuse reflectance at source-detector separations close to one transport mean free path.* J. Opt. Soc. Am. A **16**, 2935–2945 (1999).

144. A. Kienle, F.K. Forster and R. Hibst. *Influence of the phase function on determination of the optical properties of biological tissue by spatially resolved reflectance.* Opt. Lett. **26**, 1571–1573 (2001).

145. J. D. Moulton. Diffusion modelling of picosecond laser pulse propagation of turbid media. Master's thesis McMaster University, Hamilton, Ontario, Canada (1990).

146. M.S. Patterson, B. Chance and B.C. Wilson. *Time resolved reflectance and transmittance for the noninvasive measurement of tissue optical-properties.* Appl. Opt. **28**, 2331–2336 (1989).

147. T. J. Farell, M. Patterson and B. Wilson. *A diffusion theory model of spatially resolved, steady-state diffuse reflectance for noninvasive determination of tissue optical properties in vivo.* Med. Phys. **19**, 879–888 (1992).

148. R. A. J. Groenhuis, H. A. Ferwerda and J. J. Tenbosch. *Scattering and Absorption of Turbid Materials Determined From Reflection Measurements .1. Theory.* Appl. Opt. **22**, 2456–2462 (1983).

149. M. Xu, W. Cai, M. Lax and R. R. Alfano. *Photon migration in turbid media using a cumulant approximation to radiative transfer.* Phys. Rev. E **65**, 066609 (2002).

150. A. Lagendijk, R. Vreeker and P. De Vries. *Influence of internal reflection on diffusive transport in strongly scattering media.* Phys. Lett. A. **136**, 81–88 (1989).

151. N. G. Chen and J. Bai. *Monte Carlo Approach to Modeling of Boundary Conditions for the Diffusion Equation.* Phys. Rev. Lett. **80**, 5321–5324 (1998).

152. J. X. Zhu, D. J. Pine and D. A. Weitz. *Internal reflection of diffusive light in random media.* Phys. Rev. A **44**, 3948– (1991).

153. R.C. Haskell, L.O. Svaasand, T.T. Tsay, T.C. Feng and M.S. Mcadams. *Boundary-conditions for the diffusion equation in radiative-transfer.* J. Opt. Soc. Am. A **11**, 2727–2741 (1994).

154. S.R. Arridge, M. Schweiger, M. Hiraoka and D.T. Delpy. *A finite-element approach for modeling photon transport in tissue.* Med. Phys. **20**, 299–309 (1993).

155. H. Dehghani, M.E. Eames, P.K. Yalavarthy, S.C. Davis, S. Srinivasan, C.M. Carpenter, B.W. Pogue and K.D. Paulsen. *Near infrared optical tomography using NIRFAST: Algorithm for numerical model and image reconstruction.* Comm. Numer. Methods. Eng. **25**, 711–732 (2008).

156. B. Bret. *Multiple light scattering in porous gallium phosphide.* PhD thesis, University of Twente (2005). URL `http://www.wavesincomplexmedia.com`.

157. B. A. van Tiggelen, R. Maynard and A. Heiderich. *Anisotropic light diffusion in oriented nematic liquid crystals.* Phys. Rev. Lett. **77**, 639–642 (1996).

158. M. H. Kao, K. A. Jester, A. G. Yodh and P. J. Collings. *Observation of Light Diffusion and Correlation Transport in Nematic Liquid Crystals.* Phys. Rev. Lett. **77**, 2233–2236 (1996).

159. D. S. Wiersma, A. Muzzi, M. Colocci and R. Righini. *Time-Resolved Anisotropic Multiple Light scattering in Nematic Liquid Crystals.* Phys. Rev. Lett. **83**, 4321–4324 (1999).

160. P. M. Johnson, B. P. J. Bret, J. Gómez Rivas, J. J. Kelly and A. Lagendijk. *Anisotropic Diffusion of Light in a Strongly Scattering Material.* Phys. Rev. Lett. **89**, 1–4 (2002).

161. P. M. Johnson, S. Faez and A. Lagendijk. *Full characterization of anisotropic diffuse light.* Opt. Express **16**, 7435–7446 (2008).

162. P. M. Johnson and A. Lagendijk. *Optical anisotropic diffusion: new model systems and theoretical modeling.* J. Biomed. Opt **14**, 054036–1 – 054036–9 (2009).

163. S. Tsuchikawa and S. Tsutsumi. *Application of time-of-flight near-infrared Spectroscopy to wood with anisotropic cellular structure.* Appl. Spectrosc. **56**, 869–876 (2002).

164. J. Alnis, B. Anderson, M. Sjöholm, G. Somesfalean and S. Svanberg. *Laser spectroscopy of free molecular oxygen dispersed in wood materials.* Appl. Phys. B **77**, 691–695 (2003).

165. A. Kienle, C. D'Andrea, F. Foschum, P. Taroni and A. Pifferi. *Light propagation in dry and wet softwood.* Opt. Express **16**, 9895–9906 (2008).

166. T. Binzoni, C. Courvoisier, R. Giust, G. Tribillon, T. Gharbi, J. C. Hebden, T. S. Leung, J. Roux and D. T. Delpy. *Anisotropic photon migration in human skeletal muscle.* Phys. Med. Biol. **51**, N79–N90 (2006).

167. A. Sviridov, V. Chernomordik, M. Hassan, A. Russo, A. Eidsath, P. Smith and A. Gandjbakhche. *Intensity profiles of linearly polarized light backscattered from skin and tissue-like phantoms.* J. Biomed. Opt. **10**, 014012 (2005).

168. A. Kienle and R. Hibst. *Light Guiding in Biological Tissue due to Scattering.* Phys. Rev. Lett. **97**, 018104 (2006).

169. S. Nickell, M. Hermann, M. Essenpreis, Farrell T. J., U. Krämer and M. S. Patterson. *Anisotropy of light propagation in human skin.* Phys. Med. Biol. **45**, 2873–2886 (2000).

170. C. Baravian, F. Caton, J. Dillet, G. Toussaint and P. Flaud. *Incoherent light transport in an anisotropic random medium: A probe of human erythrocyte aggregation and deformation.* Phys. Rev. E **76**, 011409 (2007).

171. A. Kienle, F. K. Forster and R. Hibst. *Anisotropy of light propagation in biological tissue.* Opt. Lett. **29**, 2617–2619 (2004).

172. A. Kienle. *Anisotropic Light Diffusion: An Oxymoron?* Phys. Rev. Lett. **98**, 218104–1 – 218104–4 (2007).

173. B.J. Brinkworth. *Pulsed-lidar reflectance of clouds.* Appl. Opt. **12**, 427–428 (1973).

174. E.A. Bucher and R.M. Lerner. *Experiments on light pulse communication and propagation through atmospheric clouds.* Appl. Opt. **12**, 2401–2414 (1973).

175. K. Shimizu, A. Ishimaru, L. Reynolds and A.P. Bruckner. *Backscattering of a picosecond pulse from densely distributed scatterers.* Appl. Opt. **18**, 3484–3488 (1979).

176. B. Chance, S. Nioka, J. Kent, K. Mccully, M. Fountain, R. Greenfeld and G. Holtom. *Time-resolved spectroscopy of hemoglobin and myoglobin in resting and ischemic muscle.* Anal. Biochem. **174**, 698–707 (1988).

177. B. Chance, J.S. Leigh, H. Miyake, D.S. Smith, S. Nioka, R. Greenfeld, M. Finander, K. Kaufmann, W. Levy, M. Young, P. Cohen, H. Yoshioka and R. Boretsky. *Comparison of time-resolved and time-unresolved measurements of deoxyhemoglobin in brain.* P. Natl. Acad. Sci. USA **85**, 4971–4975 (1988).

178. W. Becker. *Advanced time-correlated single photon counting techniques.* Spinger (2005).

179. G. Reich. *Near-infrared spectroscopy and imaging: Basic principles and pharmaceutical applications.* Adv. Drug Deliver. Rev. **57**, 1109–1143 (2005).

180. S. Cova, M. Ghioni, A. Lacaita, C. Samori and F. Zappa. *Avalanche photodiodes and quenching circuits for single-photon detection.* Appl. Opt. **35**, 1956–1976 (1996).

181. S. Cova, M. Ghioni, A. Lotito, C. Rech and F. Zappa. *Evolution and prospects for single-photon avalanche diodes and quenching circuits.* J. Mod. Optic. **51**, 1267–1288 (2004).

182. A. Tosi, A. Dalla Mora, F. Zappa, G. Gulinatti, D. Contini, A. Pifferi, L. Spinelli, A. Torricelli and R. Cubeddu. *Fast-gated single-photon counting technique widens dynamic range and speeds up acquisition time in time-resolved measurements.* Opt. Express **19**, 10735–10746 (2011).

183. A. Pifferi, A. Torricelli, L. Spinelli, D. Contini, R. Cubeddu, F. Martelli, G. Zaccanti, A. Tosi, A. Dalla Mora, F. Zappa and S. Cova. *Time-Resolved Diffuse Reflectance Using Small Source-Detector Separation and Fast Single-Photon Gating.* Phys. Rev. Lett. **100**, 138101– (2008).

184. A. Tosi, A. Dalla Mora, F. Zappa and S. Cova. *Single-photon avalanche diodes for the near-infrared range: detector and circuit issues.* J. Mod. Optic. **56**, 299–308 (2009).

185. C. Abrahamsson. *Time-resolved spectroscopy for pharmaceutical applications.* PhD thesis, Lund Unviersity (2005). URL `http://atomic.physics.lu.se/biophotonics`.

186. C. D'Andrea, D. Comelli, A. Pifferi, A. Torricelli, G. Valentini and R. Cubeddu. *Time-resolved optical imaging through turbid media using a fast data acquisition system based on a gated CCD camera.* J. Phys. D. **36**, 1675 (2003).

187. J. G. Fujimoto, S. De Silvestri, E. P. Ippen, C. A. Puliafito, R. Margolis and A. Oseroff. *Femtosecond optical ranging in biological systems.* Opt. Lett. **11**, 150–152 (1986).

188. R. H. J. Kop, P. de Vries, R. Sprik and A. Lagendijk. *Observation of Anomalous Transport of Strongly Multiple Scattered Light in Thin Disordered Slabs.* Phys. Rev. Lett. **79**, 4369–4372 (1997).

189. P. M. Johnson, A. Imhof, B. P. J. Bret, J. G. Rivas and A. Lagendijk. *Time-resolved pulse propagation in a strongly scattering material.* Phys. Rev. E **68**, 016604 (2003).

190. S. Andersson-Engels, R. Berg, A. Persson and S. Svanberg. *Multispectral tissue characterization with time-resolved detection of diffusely scattered white-light.* Opt. Lett. **18**, 1697–1699 (1993).

191. C. Abrahamsson, T. Svensson, S. Svanberg, S. Andersson-Engels, J. Johansson and S. Folestad. *Time and wavelength resolved spectroscopy of turbid media using light continuum generated in a crystal fiber.* Opt. Express **12**, 4103–4112 (2004).

192. A. Bassi, J. Swartling, C. D'Andrea, A. Pifferi, A. Torricelli and R. Cubeddu. *Time-resolved spectrophotometer for turbid media based on supercontinuumgeneration in a photonic crystal fiber.* Opt. Lett. **29**, 2405–2407 (2004).

193. A. Pifferi, A. Torricelli, P. Taroni, D. Comelli, A. Bassi and R. Cubeddu. *Fully automated time domain spectrometer for the absorption and scattering characterization of diffusive media.* Rev. Sci. Instrum. **78**, 053103 (2007).

194. A. Bassi, A. Farina, C. D'Andrea, A. Pifferi, G. Valentini and R. Cubeddu. *Portable, large-bandwidth time-resolved system for diffuse optical spectroscopy.* Opt. Express **15**, 14482–14487 (2007).

195. A. Farina, A. Bassi, A. Pifferi, P. Taroni, D. Comelli, L. Spinelli and R. Cubeddu. *Bandpass effects in time-resolved diffuse spectroscopy.* Appl. Spectrosc. **63**, 48–56 (2009).

196. A. Kienle, L. Lilge, M.S. Patterson, R. Hibst, R. Steiner and B.C. Wilson. *Spatially resolved absolute diffuse reflectance measurements for noninvasive determination of the optical scattering and absorption coefficients of biological tissue.* Appl. Opt. **35**, 2304–2314 (1996).

197. Z. Q. Shi and C. A. Anderson. *Scattering Orthogonalization of Near-infrared Spectra for Analysis of Pharmaceutical Tablets.* Anal. Chem. **81**, 1389–1396 (2009).

198. A. Dimofte, J.C. Finlay and T.C. Zhu. *A method for determination of the absorption and scattering properties interstitially in turbid media.* Phys. Med. Biol. **50**, 2291–2311 (2005).

199. M. P. van Albada, B. A. van Tiggelen, A. Lagendijk and A. Tip. *Speed of Propagation of Classical Waves in Strongly Scattering Media.* Phys. Rev. Lett. **66**, 3131–3135 (1991).

200. J. G. Rivas, R. Sprik, A. Lagendijk, L. D. Noordam and C. W. Rella. *Static and dynamic transport of light close to the Anderson localization transition.* Phys. Rev. E. **63**, 046613 (2001).

201. C. Abrahamsson, A. Löwgren, B. Strömdahl, T. Svensson, S. Andersson-Engels, J. Johansson and S. Folestad. *Scatter correction of transmission near-infrared spectra by photon migration data: Quantitative analysis of solids.* Appl. Spectrosc. **59**, 1381–1387 (2005).

202. A. Cerussi, N. Shah, D. Hsiang, A. Durkin, J. Butler and B. J. Tromberg. *In vivo absorption, scattering, and physiologic properties of 58 malignant breast tumors determined by broadband diffuse optical spectroscopy.* J. Biomed. Opt. **11**, 044005 (2006).

203. F. Bevilacqua, A. J. Berger, A. E. Cerussi, D. Jakubowski and B. J. Tromberg. *Broadband Absorption Spectroscopy in Turbid Media by Combined Frequency-Domain and Steady-State Methods.* Appl. Opt. **39**, 6498–6507 (2000).

204. T.H. Pham, O. Coquoz, J.B. Fishkin, E. Anderson and B.J. Tromberg. *Broad bandwidth frequency domain instrument for quantitative tissue optical spectroscopy.* Rev. Sci. Instrum. **71**, 2500–2513 (2000).

205. R.M.P. Doornbos, R. Lang, M.C. Aalders, F.W. Cross and H.J.C.M. Sterenborg. *The determination of in vivo human tissue optical properties and absolute chromophore concentrations using spatially resolved steady-state diffuse reflectance spectroscopy.* Phys. Med. Biol. **44**, 967–981 (1999).

206. J. R. Lakowicz and K. Berndt. *Frequency-domain measurements of photon migration in tissues.* Chem. Phys. Lett. **166**, 246 – 252 (1990).

207. J.B. Fishkin and E. Gratton. *Propagation of photon-density waves in strongly scattering media containing an absorbing semi-infinite plane bounded by a straight edge.* J. Opt. Soc. Am. A **10**, 127–140 (1993).

208. K.-S. No, R. Kwong, P. H. Chou and A. Cerussi. *Design and testing of a miniature broadband frequency domain photon migration instrument.* J. Biomed. Opt. **13**, 050509 (2008).

209. D.W. Marquardt. *An algorithm for least-squares estimation of nonlinear parameters.* J. Soc. Indust. Appl. Math. **11**, 431–441 (1963).

210. L. Leonardi and D.H. Burns. *Quantitative measurements in scattering media: Photon time-of-flight analysis with analytical descriptors.* Appl. Spectrosc. **53**, 628–636 (1999).

211. F. Chauchard, S. Roussel, J.M. Roger, V. Bellon-Maurel, C. Abrahamsson, T. Svensson, S. Andersson-Engels and S. Svanberg. *Least-squares support vector machines modelization for time-resolved spectroscopy.* Appl. Opt. **44**, 7091–7097 (2005).

212. S.L. Jacques. *Time-resolved reflectance spectroscopy in turbid tissues.* IEEE T. Biomed. Eng. **36**, 1155–1161 (1989).

213. B.C. Wilson and S.L. Jacques. *Optical reflectance and transmittance of tissues - principles and applications.* IEEE J. Quantum Elect. **26**, 2186–2199 (1990).

214. S. Kukreti, A. Cerussi, B. Tromberg and E. Gratton. *Intrinsic tumor biomarkers revealed by novel double-differential spectroscopic analysis of near-infrared spectra.* J. Biomed. Opt. **12**, 020509 (2007).

215. J. R. Mourant, M. Canpolat, C. Brocker, O. Esponda-Ramos, T. M. Johnson, A. Matanock, K. Stetter and J. P. Freyer. *Light scattering from cells: the contribution of the nucleus and the effects of proliferative status.* J. Biomed. Opt. **5**, 131–137 (2000).

216. B. Beauvoit, H. Liu, K. Kang, P. Kaplan, M. Miwa and B. Chance. *Characterization of absorption and scattering properties for various yeast strains by time-resolved spectroscopy.* Cell Biochem. Biophys. **23**, 91–109 (1993).

217. S.M. Richter and E.M. Sevick-Muraca. *Characterization of concentrated colloidal suspensions using time-dependent photon migration measurements.* Colloid. Surface. A **172**, 163–173 (2000).

218. J. G. Rivas, D. H. Dau, A. Imhof, R. Sprik, B. P. J. Bret, P. M. Johnson, T. W. Hijmans and A. Lagendijk. *Experimental determination of the effective refractive index in strongly scattering media.* Opt. Commun. **220**, 17–21 (2003).

219. B.W. Pogue and M.S. Patterson. *Review of tissue simulating phantoms for optical spectroscopy, imaging and dosimetry.* J. Biomed. Opt. **11**, 041102 (2006).

220. H.J. van Staveren, C.J.M. Moes, J. van Marle, S.A. Prahl and M.J.C. van Gemert. *Light-scattering in intralipid-10-percent in the wavelength range of 400-1100 nm.* Appl. Opt. **30**, 4507–4514 (1991).

221. S.T. Flock, S.L. Jacques, B.C. Wilson, W.M. Star and M.J.C. van Gemert. *Optical-properties of intralipida phantom medium for light-propagation studies.* Laser Surg. Med. **12**, 510–519 (1992).

222. L. Spinelli, F. Martelli, A. Farina, A. Pifferi, A. Torricelli, R. Cubeddu and G. Zaccanti. *Calibration of scattering and absorption properties of a liquid diffusive medium at NIR wavelengths. Time-resolved method.* Opt. Express **15**, 6589–6604 (2007).

223. G. Wagnieres, S. G. Cheng, M. Zellweger, N. Utke, D. Braichotte, J. P. Ballini and H. van den Bergh. *An optical phantom with tissue-like properties in the visible for use in PDT and fluorescence spectroscopy.* Phys. Med. Biol. **42**, 1415–1426 (1997).

224. S.J. Madsen, M.S. Patterson and B.C. Wilson. *The use of india ink as an optical absorber in tissue-simulating phantoms.* Phys. Med. Biol. **37**, 985–993 (1992).

225. M. Firbank and D.T. Delpy. *A design for a stable and reproducible phantom for use in near-infrared imaging and spectroscopy.* Phys. Med. Biol. **38**, 847–853 (1993).

226. P. E. Zerbini, M. Vanoli, M. Grassi, A. Rizzolo, M. Fibiani, R. Cubeddu, A. Pifferi, L. Spinelli and A. Torricelli. *A model for the softening of nectarines based on sorting fruit at harvest by time-resolved reflectance spectroscopy.* Postharv. Biol. Tech. **39**, 223–232 (2006).

227. S. Tsuchikawa and T. Hamada. *Application of Time-of-Flight Near Infrared Spectroscopy for Detecting Sugar and Acid Contents in Apples.* J. Agric. Food Chem. **52**, 2434–2439 (2004).

228. J.A. Weinman and S.T. Shipley. *Effects of multiple-scattering on laser pulses transmitted through clouds.* J. Geophys. Res. **77**, 7123–7128 (1972).

229. C. D'Andrea, A. Farina, D. Comelli, A. Pifferi, P. Taroni, G. Valentini, R. Cubeddu, L. Zoia, M. Orlandi and A. Kienle. *Time-resolved optical spectroscopy of wood.* Appl. Spectrosc. **62**, 569–574 (2008).

230. G. H. Watson, P. A. Fleury and S. L. McCall. *Searching for photon localization in the time domain.* Phys. Rev. Lett. **58**, 945–948 (1987).

231. C. M. Aegerter and G. Maret. *Coherent Backscattering and Anderson Localization of Light.* Prog. Optics **52**, 1 – 62 (2009).

232. Z. Q. Shi and C. A. Anderson. *Pharmaceutical Applications of Separation of Absorption and Scattering in Near-Infrared Spectroscopy (NIRS).* J. Pharm. Sci. **99**, 4766–4783 (2010).

233. J. Johansson, S. Folestad, M. Josefson, A. Sparen, C. Abrahamsson, S. Andersson-Engels and S. Svanberg. *Time-resolved NIR/Vis spectroscopy for analysis of solids: Pharmaceutical tablets.* Appl. Spectrosc. **56**, 725–731 (2002).

234. T. S. Pan, D. Barber, D. Coffin-Beach, Z. G. Sun and E. M. Sevick-Muraca. *Measurement of low-dose active pharmaceutical ingredient in a pharmaceutical blend using frequency-domain photon migration.* J. Pharm. Sci. **93**, 635–645 (2004).

235. V. Busignies, P. Porion, B. Leclerc, P. Evesque and P. Tchoreloff. *Application of PGSTE-NMR technique to characterize the porous structure of pharmaceutical tablets.* Eur. J. Pharm. Biopharm. **69**, 1160–1170 (2008).

236. P. Porion, V. Busignies, V. Mazel, B. Leclerc, P. Evesque and P. Tchoreloff. *Anisotropic Porous Structure of Pharmaceutical Compacts Evaluated by PGSTE-NMR in Relation to Mechanical Property Anisotropy.* Pharm. Res. **27**, 2221–2233 (2010).

237. T. Svensson, M. Andersson, L. Rippe, J. Johansson, S. Folestad and S. Andersson-Engels. *High sensitivity gas spectroscopy of porous, highly scattering solids.* Opt. Lett. **33**, 80–82 (2008).

238. J. Manara, R. Caps, F. Raether and J. Fricke. *Characterization of the pore structure of alumina ceramics by diffuse radiation propagation in the near infrared.* Opt. Commun. **168**, 237–250 (1999).

239. T. Svensson, E. Adolfsson, M. Lewander, C. T. Xu and S. Svanberg. *Disordered, strongly scattering porous materials as miniature multipass gas cells.* Phys. Rev. Lett. **107**, 143901 (2011).

240. D. Grosenick, H. Wabnitz, H.H. Rinneberg, K.T. Moesta and P.M. Schlag. *Development of a time-domain optical mammograph and first in vivo applications.* Appl. Opt. **38**, 2927–2943 (1999).

241. D. Grosenick, K.T. Moesta, H. Wabnitz, J. Mucke, C. Stroszczynski, R. Macdonald, P.M. Schlag and H. Rinneberg. *Time-domain optical mammography: initial clinical results on detection and characterization of breast tumors.* Appl. Opt. **42**, 3170–3186 (2003).

242. M. A. Franceschini, K. T. Moesta, S. Fantini, G. Gaida, E. Gratton, H. Jess, W. W. Mantulin, M. Seeber, P. M. Schlag and M. Kaschke. *Frequency-domain techniques enhance optical mammography: Initial clinical results.* P. Natl. Acad. Sci. USA **94**, 6468–6473 (1997).

243. B. W. Pogue, S. P. Poplack, T. O. McBride, W. A. Wells, K. S. Osterman, U. L. Osterberg and K. D. Paulsen. *Quantitative hemoglobin tomography with diffuse near-infrared spectroscopy: Pilot results in the breast.* Radiology **218**, 261–266 (2001).

244. A. Pifferi, P. Taroni, A. Torricelli, F. Messina, R. Cubeddu and G. Danesini. *Four-wavelength time-resolved optical mammography in the 680-980-nm range.* Opt. Lett. **28**, 1138–1140 (2003).

245. J. R. Mourant, A. H. Hielscher, A. A. Eick, T. M. Johnson and J. P. Freyer. *Evidence of intrinsic differences in the light scattering properties of tumorigenic and nontumorigenic cells.* Cancer **84**, 366–374 (1998).

246. N. Ghosh, S. K. Mohanty, S. K. Majumder and P. K. Gupta. *Measurement of Optical Transport Properties of Normal and Malignant Human Breast Tissue.* Appl. Opt. **40**, 176–184 (2001).

247. A. E. Cerussi, A. J. Berger, F. Bevilacqua, N. Shah, D. Jakubowski, J. Butler, R. F. Holcombe and Tromberg B. J. *Sources of Absorption and Scattering Contrast for Near-Infrared Optical Mammography.* Acad. Radiol. **8**, 211 – 218 (2001).

248. P. Taroni, A. Torricelli, L. Spinelli, A. Pifferi, F. Arpaia, G. Danesini and R. Cubeddu. *Time-resolved optical mammography between 637 and 985 nm: clinical study on the detection and identification of breast lesions.* Phys. Med. Biol. **50**, 2469–2488 (2005).

249. J. Axelsson. *Model-based approaches to diffuse optical imaging and dosimetry.* PhD thesis, Lund University (2009). URL `http://atomic.physics.lu.se/biophotonics`.

250. A. Johansson. *Spectroscopic techniques for photodynamic therapy.* PhD thesis, Lund University (2007). URL `http://atomic.physics.lu.se/biophotonics`.

251. P. Vaupel, O. Thews and M. Hoeckel. *Treatment resistance of solid tumors: role of hypoxia and anemia.* Med. Oncol. **18**, 243–259 (2001).

252. D.A. Benaron, S.R. Hintz, A. Villringer, D. Boas, A. Kleinschmidt, J. Frahm, C. Hirth, H. Obrig, J.C. van Houten, E.L. Kermit, W.F. Cheong and D.K. Stevenson. *Noninvasive functional imaging of human brain using light.* J. Cerebr. Blood F. Met. **20**, 469–477 (2000).

253. J.C. Hebden, A. Gibson, R.M. Yusof, N. Everdell, E.M.C. Hillman, D.T. Delpy, S.R. Arridge, T. Austin, J.H. Meek and J.S. Wyatt. *Three-dimensional optical tomography of the premature infant brain.* Phys. Med. Biol. **47**, 4155–4166 (2002).

254. J.C. Hebden and T. Austin. *Optical tomography of the neonatal brain.* Eur. Radiol. **17**, 2926–2933 (2007).

255. A. Liebert, H. Wabnitz, J. Steinbrink, H. Obrig, M. Möller, R. Macdonald, A. Villringer and H. Rinneber. *Time-resolved multidistance near-infrared spectroscopy of the adult head: intracerebral and extracerebral absorption changes from moments of distribution of times of flight of photons.* Appl. Opt. **43**, 3037–3047 (2004).

256. J. Selb, J.J. Stott, M.A. Franceschini, A.G. Sorensen and D.A. Boas. *Improved sensitivity to cerebral hemodynamics during brain activation with a time-gated optical system: analytical model and experimental validation.* J. Biomed. Opt. **10**, 011013 (2005).

257. D. Comelli, A. Bassi, A. Pifferi, P. Taroni, A. Torricelli, R. Cubeddu, F. Martelli and G. Zaccanti. *In vivo time-resolved reflectance spectroscopy of the human forehead.* Appl. Opt. **46**, 1717–1725 (2007).